Western Australian School of Mines

Department of Exploration Geophysics

Gamma Ray Spectroscopy for Logging While Drilling in Mineral Exploration

Ida Hooshyari Far

This thesis is presented for the Degree of

Doctor of Philosophy

of

Curtin University

March 2018

Declaration

"To the best of my knowledge and belief this thesis contains no material previously published by any other person except where due acknowledgment has been made. This thesis contains no material which has been accepted for the award of any other degree or diploma in any university."

Signature: 

Date: 19/03/2018

To my dear mother, for all her love and all her tough love

To my great father, for his love, support and his dedication to our family

To my life and love partner, for his love, care and being an amazing being

Thesis Abstract

Gamma ray spectroscopy has been in use in the mineral exploration industry for decades, with much pioneering work done in the 1970's to 1980's, yet many of the techniques used to process the recorded spectrum have not improved significantly in the last 30 years. Technological developments in slim logging tools appear to have not kept pace with other technological developments, such as advances in scintillator materials for better gamma detectors, and neutron generators for electronic control of radiation. Yet the ability to collect good quality gamma-ray energy spectra with 256 or more channels is common and the computational resources for better data processing are now abundant. Despite such advances there hasn't been much change in the way natural gamma spectra are analysed, in the borehole or in airborne radiometrics, except for noise reduction techniques such as Noise Adjusted Singular Value Decomposition (NASVD) and Maximum Noise Fraction (MNF).

Natural gamma-ray logs currently estimate concentrations of natural radioisotopes of uranium, thorium and potassium (U, Th and K) based on analysis of spectral peaks in the gamma-energy spectrum and estimation the decay series is in radioactive equilibrium. However, there is, potentially, other useful lithological information hidden within the recorded gamma-ray spectrum. This extra information lies in the gamma rays scattered by the rock, normally rejected as noise or background to spectral peaks. These gamma rays are the ones that have interacted with elements other than K, U, and Th and provide new physical information about the rock matrix. The research in this thesis principally explores the use of a ratio between photoelectric absorption and Compton scattering and uses a calculation of a ratio (the Heavy Mineral Indicator) of these effects to measure changes in effective atomic number (Z_{eff}) in the formation. Furthermore, it is postulated that as the relative atomic number of iron is greatest amongst the most common crustal elements then the Heavy Mineral Indicator (HMI) is generally an indication of the iron content of the rock in most cases.

Simulation, laboratory scale models, and field experiments all demonstrate that the natural gamma-ray spectrum recorded during borehole drilling (Logging-While-Drilling) can be used to track changes in heavy element concentrations with HMI, and HMI correlates well with iron-rich zones. The best regions within the gamma spectrum to be exploited are energies between 50-150 keV and between 200-500

keV; the ratio of gamma-ray counts in these energy windows provides a good measure of Z_{eff} variation. It was found that the small gamma-ray detectors used in wireline logging collected too few gamma rays to be useful in measuring changes in Z_{eff} with HMI. Wireline logging speeds are too fast (even at 2 m/min) to collect sufficient scattered gamma rays to produce statistically useful results. Thus, it is concluded that logging-while–drilling measurement is the only viable means to detect changes in Z_{eff} because logging speed is much slower.

Another novel aspect of looking at the relationship between HMI and iron is the application of this type of analysis to conventional litho-density tools that use an isotope gamma-ray source. Data were analysed from experimental litho-density tools designed to measure density in iron ore deposits in the Pilbara area of Western Australia. The litho-density gamma spectra from iron ore formations provided detectably higher HMI measures as expected due to relatively high Z_{eff} in this environment. Thus, HMI values can act as a proxy for an iron assay to differentiate iron ore from waste rock in near real-time.

An opportunity to test HMI measurements on airborne radiometrics represented a slight side-track in the research. Advances in airborne gamma ray spectrometers and the implementation of low-level surveys provide high quality spectra similar to logging while drilling approaches. The analysis of a well-studied radiometrics data set from Elashgin, Western Australia, show very clearly that iron-rich soils and surface formations are mapped with HMI. Thus, using the same approach in analysing natural gamma rays from boreholes allows maps of Fe and K, U, Th to be made simply by reprocessing legacy data.

This work has demonstrated that analysing the scattered gamma rays in the earth may be used to see changes in soils and rocks non-invasively using natural gamma radiation. Additionally, the measure of these changes, the Heavy Mineral Indicator, is generally related to the iron content of the material. In combination, these two findings alone represent a significant advance in how we may use spectral-gamma measurements in the earth sciences.

Acknowledgments

Firstly, I would like to thank sincerely my supervisor Anton Kepic for his guidance and his support. It has been a great privilege to work with him and to benefit from his brilliant ideas. I am also very grateful to my co-supervisor Michael Carson for his assistance, enthusiasm and great support. I am also thankful to Anousha Hashemi from BHP Billiton for providing me her time and knowledge.

I would like to acknowledge the Deep Exploration Technology Commonwealth Research Centre (DETCRC) for their financial assistance. Additionally I wish to acknowledge Curtin University for my CIPRS scholarship.

Last but not least, I thank my family in Iran for supporting me and giving me so much positive energy despite the distance and my beautiful friends in Australia.

List of publications

Extended abstracts

Hooshyari, I., A. Kepic, M, Carson, 2016, Gamma-ray spectra analysis for Lithology investigation. Near Surface Geoscience 2016 - First Conference on Geophysics for Mineral Exploration and Mining, 4-8 September 2016. Barcelona, Spain: EAGE.

Hooshyari, I., A. Kepic, A. Greenwood, A. Podolska, 2015, A New Logging While Drilling Approach for Natural Gamma Spectroscopy with Diamond Drilling. Joint assembly, AGU-GAC-MAC-CGU, 3-7May 2015, Montreal, Canada

Hooshyari-Far, I., A. Kepic, and A. Podolska. 2015. A new approach provides opportunities for spectral gamma analysis in boreholes for mineral exploration. ASEG Extended Abstracts 2015: 24th International Geophysical Conference and Exhibition. 1-4 February 2015, Perth, Australia

Hooshyari, I., Kepic, A., Javadipour, Sh., 2014. Resistivity and Induced polarization technique for mapping hematite rich areas in Iran: ASEG Conference 2015

Kepic, A., A. Podolska, I. Hooshari-Far, and A. Greenwood, 2015, New scintillators and method for spectral gamma logging in slim boreholes. Near-Surface Asia Pacific Conference, Waikoloa, Hawaii, 7-10 July 2015. 220-223.

Journal articles in preparation

Hooshyari, I., Kepic, A., Carson, M, Heavy metal indicator in logging while drilling, (Geophysics)

Hooshyari, I., Kepic, A., Carson, M, A novel approach in analysing full spectrum airborne radiometric data (Geophysics Research Letters)

Contents

List of Figures

List of Tables

Nomenclature

Glossary of abbreviations

CPR	Compton Scattering to Peak Ratio
DETCRC	Deep Exploration Technology Commonwealth Research Centre
HMI	Heavy Mineral Indicator
IP	Induced Polarisation
LWD	Logging While Drilling
SGG	Spectral Gamma Gamma
BGO	Bismuth Germinate Oxide
NaCl	Sodium choloride
PVC	Polyvinyl chloride
LSB	Laboratory Scale Borehole
CsI(NaI)	Caesium iodide Sodium choloride
PMT	Photomultiplier Tube
MCA	Multichannel Analyser
KCl	Potassium chloride
BHA	Bottom Hole Assembly
TC	Total Counts
XRF	X-ray fluorescence
SD	Standard Deviation
Ave	Average
BDw	Bulk Density - Whole Earth
DEM	Digital Elevation Model
DSMART	Disaggregation and Harmonisation of Soil Map Units Through Resampled Classification Trees

PROPR	Digital Soil Property Mapping Using Soil Class Probability Raster

Indices, Sub- and Superscripts

B	Bulk
E	Electron
E_{ff}	Effective

Symbols

K	Potassium
U	Uranium
Th	Thorium
I_0	Initial energy of gamma rays
I	Energy of gamma ray
μ	linear attenuation coefficient
x	Distance
τ	Photoelectric cross section
ρ	Density
m	mass attenuation coefficient
Z	Atomic number
A	Atomic mass
σ_{pe}	Probability of photoelectric absorption
E'	Gamma ray energy after scattering
E^0	Gamma ray energy before scattering
Θ	Scattering angle
c	Speed of light

H	Plank constant
ν	Frequency
keV	Kilo electron volt
MeV	Mega electron volt
W	Window
N	Number
I_p	intensity of gamma rays deposited directly in a detector
β	a factor to scale the intensity to Compton scattered gamma rays
I_c	intensity of gamma rays from Compton scattering
g	Gram
cm	Centimetre
a	Slope of line
b	Intercept point

CHAPTER 1. INTRODUCTION

1.1 MOTIVATION

The main aim of drilling a borehole is to collect information related to the geology and lithology of a formation. For this purpose, a drill core or rock chips are taken out, logged by a geologist in the field and then sent to a laboratory for further analysis. There are several problems associated with this practice, such as missing a core, particularly in the depth of interest or collapsing boreholes before core retrieval. Moreover, the core assay is not necessarily representative of the bulk properties of the formation especially in inhomogeneous rock ore. Additionally, core logging in the laboratory, as well as in the field, is time consuming and costly. Geophysical logging can provide more representative and robust information about the surrounding rock than just the core and can alleviate the problem of missing core sections. Geophysical logging is also faster and less expensive compared to geological core logging.

Logging While Drilling (LWD) is a technique of recording geophysical data while drilling is in progress. In LWD sensing tools are incorporated into the drill string to facilitate close to real-time data acquisition. This technology is well developed in the oil and gas industry but has not yet been adopted by the mineral industry, for reasons outlined below. The benefits of having access to real-time data lead to a quicker analysis of information and can be used to improve decision making at both the planning and operational levels (Beattie 2009), for instance, knowing when to stop drilling, or immediately placing infill drill-holes to map unanticipated changes before the drill rig is remobilised. LWD provides significant advantages, aside from the real-time measurements, in that logs are less influenced by drilling fluid invasion as less time elapses in the boreholes before measurement is undertaken (Crain 2014). Real commercial LWD tools introduced in the 1970s and the 1980s have produced a greater variety of measurements, such as gamma rays, resistivity, Nuclear Magnetic Resonance (NMR) and neutron logs (Crain 2014).

Similar to LWD tools, analysis methods have advanced accordingly; for instance gamma-ray spectroscopy has advanced from simply determining the concentration of potassium (K), uranium (U) and thorium (Th) to measuring the photoelectric factor P_e, a property of the rock matrix. The low energy region of the gamma-ray spectrum, which is

used to measure P_e, is sensitive to the average atomic number of a formation. Clays and heavy minerals have high P_e whilst sandstones typically have low P_e. The measurement of P_e has been incorporated into the litho-density tool (GOWell Petroleum Equipment, 2016) which the lithology and density of a formation can be interpreted. This measures the formation-scattered radiation from an isotopic source, incorporated into the tool.

In the mineral industry, there have been advances related to drilling tools such as developing slimmer and more efficient tools that can drill faster and which have less impact on the environment. However, LWD has not been adopted by the minerals industry due, primarily, to the lack of available tools (MaterialsWorld 2009). Researchers at Curtin University and DET CRC have developed a LWD tool called "Auto-shuttle". Auto-shuttle is attached to the core barrel and records the natural gamma-ray spectrum when the borehole is being drilled. To have such an instrument, which provides a high-quality spectrum in near real-time, can transform the information available for exploration in the mineral industry. The acquisition of high-quality data opens an opportunity to improve processing techniques. This means having a better estimation the natural gamma rays associated with rock formations, which ultimately enables the detection of mineralised zones.

Historically, geophysical logging has not played a major role in mineral exploration compared to the oil and gas industry due to logging costs, technical restrictions, such as narrow and inclined holes and a lack of experience in data interpretation by mineral exploration geologists (Mutton 1994). In recent decades, the need to explore deeper and more subtle deposits in less time and a more cost-effective manner have raised interests to address the challenges of geophysical logging in mineral exploration. The application of geophysical logging in mineral exploration has been reviewed by Glenn and Nelson (1979); Czubek (1979); Glenn and Hohmann (1981); and, Killeen (1997b). Natural gamma logging is a passive method that is based on the measurement of the natural radioactivity of the rocks to determine the concentrations of Th, U and K with proper calibration. The determination of these elements can be used to characterise the formation; for instance, in sedimentary rocks K is the main source of natural radioactivity due to its presence in clay minerals while in igneous rocks all three radioactive sources generally contribute more equally in the natural radiation (Killeen 1997b). In addition, during mineralisation and hydrothermal alteration the natural radioactivity of the rock increases; for example K content can increase in altered rocks (Airo 2015). Natural spectral gamma-ray measurements perform poorly in mineral wireline logging due to the fact that small borehole diameters restrict the size of the

scintillation crystals that are frequently used in gamma-ray detectors (Killeen 1997a): large, dense crystals generally make more efficient gamma-ray detectors. Nowadays the most common technique of measuring gamma ray activities is densitometry or gamma-gamma logging. This method is based on measuring the density of the surrounding rocks in-situ within the borehole. It works based on measuring scattered gamma rays from a formation with a logging tool which incorporates a weak radioactive source (Killeen 1997a). The possibility of using high and low energy parts of gamma-ray spectrum to determine the elemental composition of rocks in mining geophysics was first studied by Czubek (1966). This concept was further investigated by Killeen (1989). He conducted extended experiments to develope a method, called Spectral Gamma Gamma (SGG), to indicate heavy elements in rocks. The SGG ratio is the ratio of counts in the low and high energy regions of the spectrum and, as with P_e, is sensitive to variations in atomic numbers. This method is useful for determining the ore-grade zones of heavy elements such as zinc and lead. This approach used a spectral gamma-ray tool equipped with a Co^{60} radioactive source that emits low and high energy. The use of a radioactive source makes this method less favourable to the mining industry due to the possibility of losing the source and the downtime that results from its retrieval. This issue encouraged us to develop a technique to determine the variations in the elemental composition of the formations by means of natural gamma-ray spectroscopy alone.

1.2 RESEARCH AIMS

The primary aim of this research is to determine whether the natural gamma-ray spectrum, recorded during borehole drilling, can be used to track changes in heavy element concentration and to indicate iron-rich zones. This research also proposes to expand the horizon of gamma-ray spectral analysis from downhole to airborne. To achieve these goals, the SGG method introduced by Killeen (1989) is exploited and studied in depth and applied to the *natural* gamma-ray spectrum. We use the term HMI (heavy mineral indicator) to mean the SGG ratio applied to the natural gamma-ray spectrum. The following questions will be answered:

1. How can the gamma-ray spectrum measure variations in the elemental composition of a formation?

2. How important is the spectral quality in the HMI method and how do we define a high-quality spectrum?
3. Could the HMI method be used to detect iron-rich zones?
4. Could this method be applied to other areas where natural radioactivity is measured (airborne gamma-ray spectrometry)?

The first question may be answered by reviewing the physical mechanisms of gamma-ray scattering and absorption and how different regions of the spectrum relate to different properties of the scattering medium. We answered the second question by developing a computational approach to understand how counting statistics affects the error on the HMI. By developing computer simulations and laboratory models we aim to understand how the HMI varies with different formation compositions. Computer modelling has the advantage of being able to construct and test scenarios, which may otherwise be difficult to investigate. Following on from this, we then look at borehole data, recorded from a specially designed tool, in order to determine the applicability and sensitivity of the technique.

1.3 THESIS OUTLINE

This thesis has been formatted in seven chapters, including this introduction as the first chapter. The material of each chapter is briefly described as follows:

Chapter 2: In this chapter a brief description is provided of gamma-ray radiation and the principal of its interactions with matter as it relates to the detection of physical parameters of formations. We then review the historical developments of spectral analysis and current practice in this direction. Finally, we introduce the analysis techniques studied in this research.

Chapter 3: In this chapter, we evaluate the study's methodology, which implements the use of computer-based simulations and laboratory measurements. We simulate simple models that only contain iron and cement as their formation to directly study the effect of iron content variations in a formation with HMI values. We then discuss how we expand the simulation to more complicated models in which the models' parameters are determined based on the laboratory conditions. Then we describe how we further conduct our simulations to even more complicated situations, which are not very feasible, or very costly, to construct

under laboratory environments. We go on to explain the study's laboratory set-ups, calibration and measurement parameters and as the final step in this chapter, the results from the simulations with the laboratory are compared and discussed.

Chapter 4: In this chapter, we discuss the role of spectrum quality in the HMI method by comparing the HMI responses from the Auto-shuttle to wireline datasets. To this end the results of analysing spectra from our field measurement, prototype Auto-shuttle and wireline spectral tool are presented. The chapter closes with a discussion on the correlation between the HMI and iron concentration in the formation.

Chapter 5: The purpose of this chapter is to study the HMI technique in relation to the current wireline practice in the mining industry as well as the correlation of the HMI with ore deposits. We present the results of the HMI calculation on the data from the litho-density tool and compare the HMI values with the iron assays. The same approach is taken with the data from the spectral gamma tool and the results from both tools are compared and discussed. Finally we discuss that using the joint information from the HMI and Total Count (TC) logs can result in better lithology interpretation.

Chapter 6: In this chapter we analyse a high-quality radiometric dataset to evaluate the potential of the HMI technique in the process of characterizing regolith. We discuss how the HMI method could be applied as a new technique to provide more information from the earth surface since radiometric data is a measure of natural radioactivity.

Chapter 7: This chapter summaries the main outcomes of this research and provide recommendations for further study.

CHAPTER 2. INTRODUCTION TO GAMMA-RAY SPECTROSCOPY

2.1 NUCLEAR PHYSICS FOR LOGGING APPLICATION

2.1.1 The origin of natural gamma rays

The natural gamma-ray spectra as is evident from the name, detects the natural gamma radiation emitted from a formation (Serra, Baldwin, and Quirein 1980). First, we should explain the origin of this natural emission. Prominent natural gamma radiation originates from three potassium, ^{40}K, thorium, ^{232}Th, uranium, ^{238}U and their daughter products (Serra 1984). ^{40}K has a single stable daughter and only emits gamma rays at an energy level of 1.46 MeV, while uranium and thorium decay through a series of unstable isotopes, each of which decays and has characteristic gamma-ray energies. Hence natural gamma-ray spectra includes many different energies (Evans 1955). The largest source of radioactivity in a formation is potassium, which is a common element in the Earth's crust. There are numerous minerals in a formation containing potassium (Ellis and Singer 2008). In comparison, thorium- and uranium-bearing minerals are scarce. Uranium content is generally associated with organic matter in the sediments, frequently in organic shales. Thorium generally reflects heavy minerals, such as monazite and zircon (Hassan 1976), and is also associated with aluminium and titanium. However, the largest concentration of thorium is seen to be related to shales (Hassan 1976). Figure 2-1 depicts the abundance of common elements in the Earth's crust.

2.1.2 Radioactivity of the elements in rocks

Serra, Baldwin, and Quirein (1980) summarised radioactivity occurrence in sedimentary rocks as follows:

- Potassium: it is seen in sediments with uncommon amounts of chemically unstable grain. Potassium feldspar, micas and alteration products such as kaolinite, sericite and chlorite are examples of potassium rich rocks.
- Thorium: it is related to detrital and not purely chemical sediments. Hence, thorium would be found mostly with clay rocks that are associated with heavy minerals. These heavy minerals are more abundant in the silty fraction. Thorium is more common in

residual sediments such as bauxite, kaolinite and bentonite, which are formed by the alteration of volcanic ash. Thorium is also presented in tuffs, conglomerates and greywacke sandstones.

- Uranium: it is associated with both chemical and detrital sediments such as shales, organic matter and uranium-bearing heavy minerals. It is also abundant within phosphates, tuff, conglomerates, greywacke sandstones and carbonates of confined media.

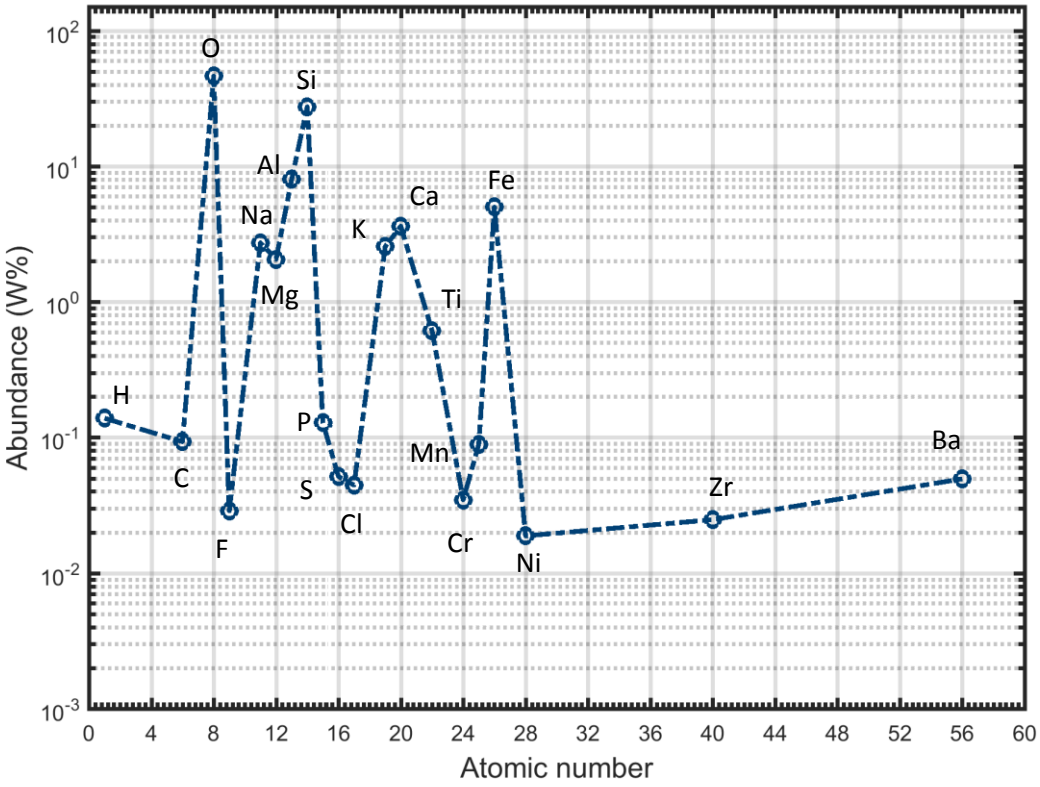

Figure 2-1 Elemental concentrations in the Earth's crust based on weight percentage are as Oxygen 47%, Silicon 28%, Aluminium 8%, Iron 5%, Calcium 3.5%, Sodium 3%, Potassium 2.5% and Magnesium 2%. Almost 99% of the Earth's crust is composed of these 8 elements (Garrels 1972).

2.1.3 Gamma ray attenuation

When gamma rays travel through matter with a thickness of x before reaching a detector, their energy attenuate exponentially as follows:

$$\frac{I}{I_0} = e^{-\mu x}, \qquad (2\text{-}1)$$

where μ is the linear attenuation coefficient, which is the sum of the probability of all interactions that gamma rays undertake when passing through matter, see equation (2-2). I_0 and I are the initial energy of the gamma ray and the energy of the gamma ray after traveling through a material, respectively (Knoll 2010).

$$\mu = \tau(photoelectric) + \sigma(Compton\ scattering) + \kappa(pair\ production) \qquad (2\text{-}2)$$

The linear attenuation coefficient (μ) depends on the energy levels of the gamma rays and the medium which gamma rays interact with. It is important to note that the linear attenuation coefficient changes with the density of the matter that the gamma rays interact with, even though the elemental compositions are kept the same. Therefore, the mass attenuation coefficient is defined in the form of the equation (2-3) to be consistent with the physical state of the materials.

$$m = \frac{\mu}{\rho}, \qquad (2\text{-}3)$$

where *m* is the mass attenuation coefficient. So, formula (2-1) can be rewritten as:

$$\frac{I}{I_0} = e^{-m\rho x}. \qquad (2\text{-}4)$$

The mass attenuation coefficient (*m*) unit is cm^2g^{-1} . For Compton scattering *m* is the same for all materials with the approximation of Z/A=1/2 (in which Z is atomic number and A is mass number of the minerals) which is the case for the majority of minerals (Knoll 2010). Hence, Compton scattering is highly influenced by the density of matter.

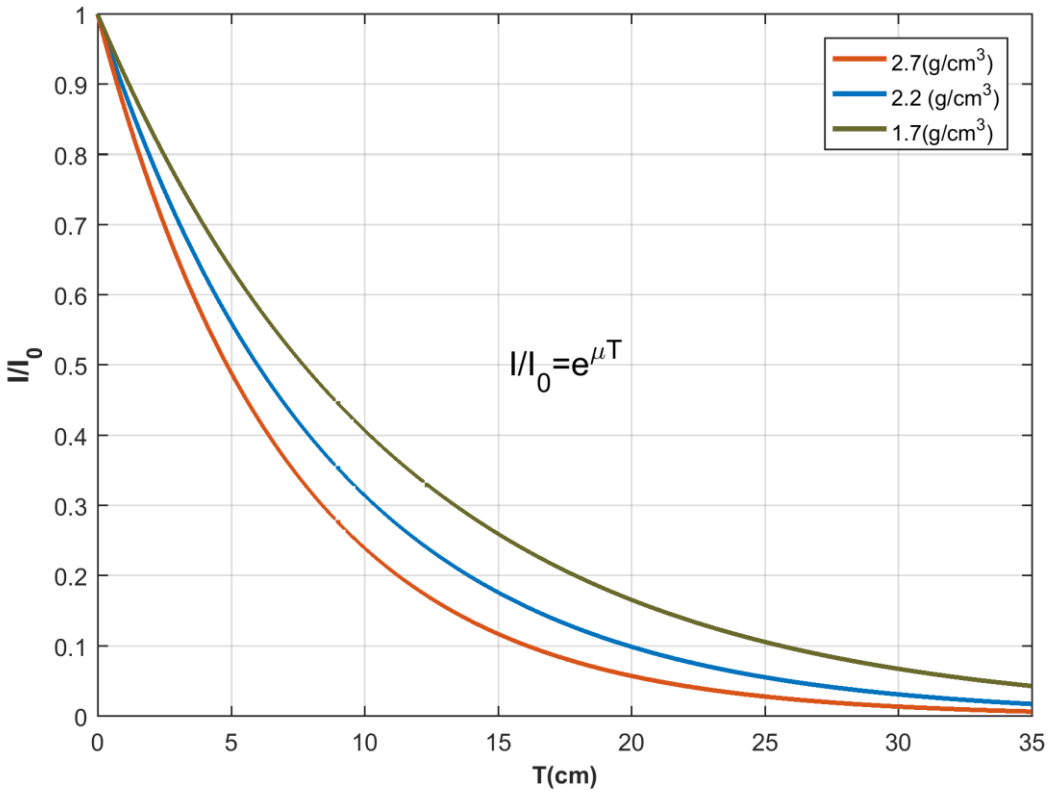

Figure 2-2 Attenuation of 1.46 MeV gamma rays for three medium with the same composition but different density. The media have similar compositions contain only Silicon (Si), leaving density the only variable. The abscissa represents the medium thickness in cm and μ is 11.56×10^{-2}. Attenuation is dependent on the physical state of the medium and can be seen to increase with increasing density.

2.1.4 Fundamentals of gamma ray interactions

The most important interactions of gamma rays in matter are as follows:

Photoelectric absorption is a process by which a gamma ray is totally absorbed and its energy is used to eject an electron from its bound shell, usually from the K shell as shown in Figure 2-3. The photoelectric effect is the major mode of interaction for gamma rays of relatively low energy. The probability of photoelectric absorption depends on the energy of the gamma rays and the atomic number of the absorber. There is no solid analytical expression for this probability but a rough approximation is (Knoll 2010),

$$\sigma_{pe} \cong \frac{Z^n}{E_\gamma^{3.15}}, \tag{2-5}$$

which depends on gamma ray energy and n varies between 4 to 5. The expression shows the high dependency of photoelectric absorption on the atomic number (Z). Since rocks contain different elemental compositions, thus different Z photoelectric absorption characteristics vary accordingly. The pore fluids have a low Z, so they cannot have a major influence on the Z of a rock (Ellis and Singer 2008). Therefore, photoelectric absorption can be applied as a tool to detect variations in lithology or rock types as will be demonstrated in this thesis.

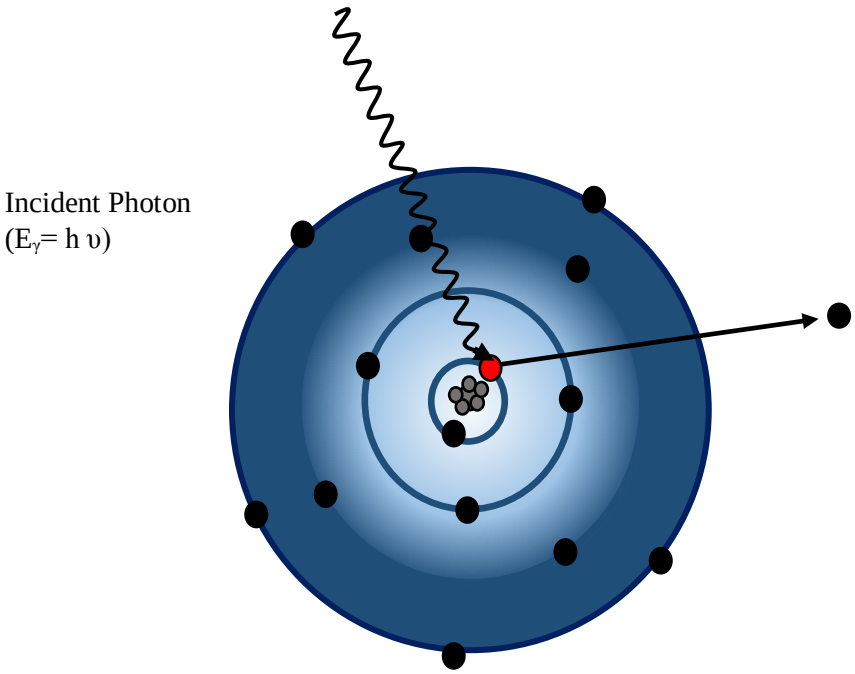

Figure 2-3 Schematic diagram showing the photoelectric effect. The gamma ray interacts with an inner shell electron (red circle) and transfers all its energy to it causing the electron to be ejected from the atom.

The next dominant gamma-ray interaction is Compton scattering. In this process the incoming gamma ray collides with an electron and is diverted by angle Θ from its initial direction. Then it imparts part of its energy to the electron. Considering this interaction as an elastic collision between two particles, we can express the gamma ray energy as a function of scattering angle Θ and incident gamma ray energy as follows:

$$E' = \frac{E_\gamma}{1 + \frac{E_\gamma}{m_0 c^2}\,(1 - \cos\Theta)}, \qquad (2\text{-}6)$$

where E' and E_γ are gamma ray energies after and before scattering, respectively. The equation (2-3) is based on the conservation of energy and momentum law. Compton scattering engages free electrons, outer shell or unbounded, therefore it does not highly depend on Z but rather the density of the scattering electrons (Knoll 2010).

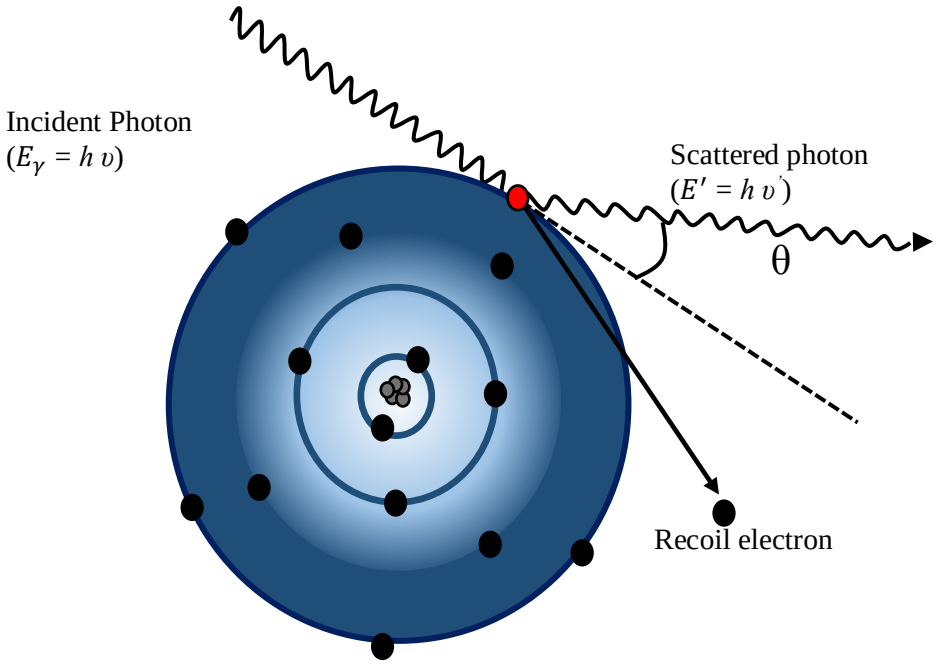

Figure 2-4 Compton scattering mechanism. The gamma ray scatters off an outer shell electron (red circle) transferring a fraction of its energy to it. The gamma ray propagates with a reduced energy E' at an angle θ with respect to its un-scattered direction.

The final important gamma ray interaction is pair production. Pair production is possible when gamma ray energy exceeds more than two times the electron rest-mass energy, 1.02 MeV. In this process, the gamma ray is absorbed and an electron-positron pair is created. In practical terms, gamma ray energy should exceed more than several MeV for a high probability of this interaction to take place (Segre 1977). After the interaction, the energy of the gamma ray above 1.02 MeV converts into kinetic energy that is shared between the electron and positron as illustrated in Figure 2-5. Since the positron is finally annihilated in the absorbing matter, two annihilation photons are generated as another product of this mechanism (Knoll 2010). There is no simple expression for pair production probability per nucleus; however, its value depends approximately on the inverse square of the atomic number of an absorbing medium (Evans 1955).

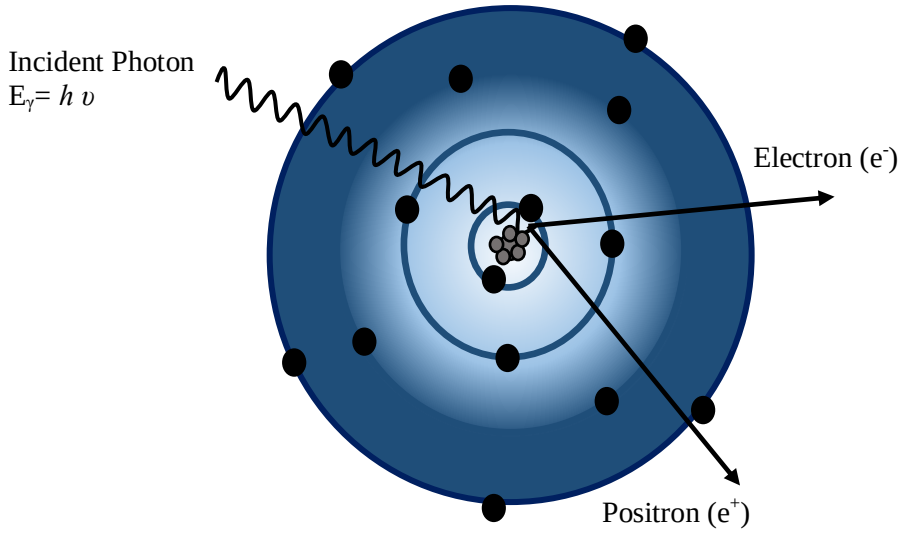

Figure 2-5 Schematic plot of Pair production mechanism. The gamma ray loses all its energy to produce an electron and a positron pair.

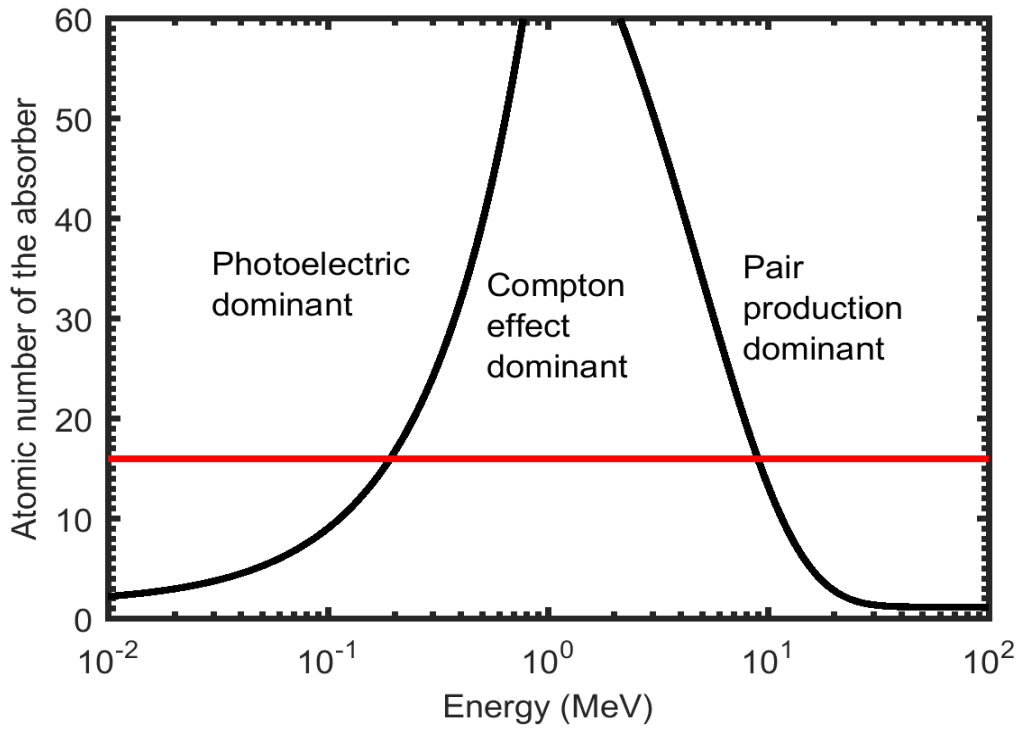

Figure 2-6 An experimantal plot of the relative importance of different gamma ray interactions. Gamma ray interactions depend on the atomic numbers of the medium and energy of incident gamma rays. The dominant scattering mechanism, at any particular energy, depends on the effective atomic number of the scattering medium. The red line represents an atomic number of 16. For most rocks in the earth the average atomic number is approximately less than 16 (Ellis 1988).

2.1.5 Gamma ray spectroscopy

Gamma ray interactions in a medium need to be recorded and analysed. For this purpose a detector generates output pulses with voltage magnitudes that are proportional to the deposited energy of an incident gamma in the detector (Crouthamel, Adams, and Dams 1970a). Regardless of the type of detectors, recorded spectra have many common features. In order to better present the features, we plotted a spectrum from a mono-energetic gamma ray source, Figure 2-7.

Full energy peak, region A, is related to the gamma rays, which deposits all energy in the detector. Within the detector these gamma rays undergo a single or several Compton scatterings that are followed by photoelectric interaction but all the energy is detected. The width of this peak depends on the detector feature and the pulse-processing electronics. For instance, better detector resolution results in a smaller width for peak A. Therefore, the detector plays an important role in gamma-ray spectrum measurement. In section 2.1.7, we introduce the different features of a detector and in section 3.4 we explain in more detail how a detector operates to measure the energy of gamma rays.

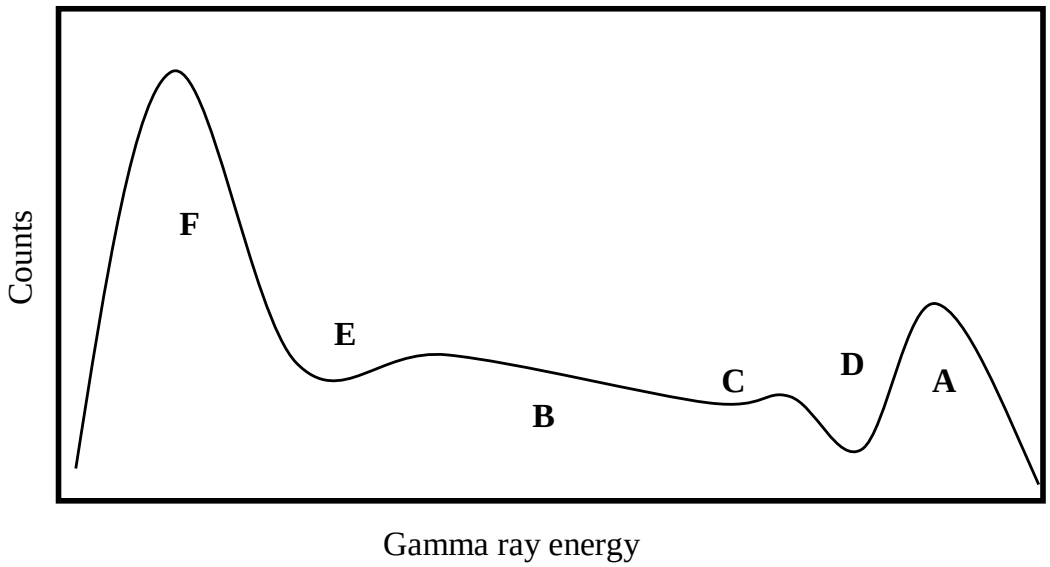

Figure 2-7 Schematic spectrum from a mono-energetic gamma source.

Moving to the slightly lower energy part of the spectrum there is a very small peak; section C, which is called the Compton edge. This corresponds to a Compton scattering, where a gamma ray transfers the most energy to an electron. In this condition, an electron

moves forward and a photon scatters with an angle of 180^0 with the respect to the original direction. Another region of the intersection is the Compton background continuum, B, where the partial energy of a gamma ray deposits in the detector under Compton scattering interactions. There is a small peak in the energy range 200 to 250 keV, E area, which is called a backscattered peak. When gamma rays from the source first collide with surrounding rock and scatter in 180^0 with respect to the original direction, a backscattered peak forms. The final important feature in a spectrum is located at a very low energy part, less than 150 keV, where gamma rays with these energies can mostly have a photoelectric interaction, region F. It is important to note that in most cases, this region is contaminated with low-amplitude electronic noise in the detector system, especially at very low energy, less than 50 keV (Reilly 1991).

2.1.6 Gamma ray measurement application

The most common gamma-ray logging method, which only records the total of gamma ray counts in a broad energy window, has been used on most other logging services to provide depth control. It also has been applied to correlate zones between different wells (Hoyer and Lock 1971). Moreover, it can identify zones with higher than normal radioactivity such as shales in formations. Advances in natural gamma-ray logging leads to developing a natural gamma spectral tool that also records gamma ray energies. Measuring gamma ray's energy is important since different rocks include different natural radioactive sources. For instance, in most cases of base metal zones, potassium is the main source of radioactivity of the rocks due to alterations, hence measuring potassium variations can help us to target mineralisation zones (Killeen 1997a).

From the preceding sections, it is shown that the spectra formed from gamma rays passing through a medium contain information related to that medium. Therefore, we can exploit this characteristic to obtain knowledge regarding the formations where gamma spectra are collected. The photoelectric part of a spectrum reflects the variation in lithology and density, and Compton scattering depends on the density of formations. Therefore, an adequate analysis of the spectra can provide a good understanding of the surrounding mediums. In recent years, developments in gamma ray spectral tools have also provided opportunities in improving spectral analysis techniques. In the following sections, we briefly introduce some of these tools.

2.1.7 Gamma ray measurement instrumentation

In this section, we briefly introduce the common instruments used in gamma ray spectroscopy and their functions. As we explained in previous sections, gamma rays are registered in a detector after their interactions with the medium they travel through. The gamma rays' energies deposited in the detector are proportional to the output pulse amplitudes from the detector and electronic system (Reilly 1991). A common gamma ray spectral tool includes a detector where a gamma ray interaction produces a weak electrical pulse. The detector is followed by a preamplifier, an amplifier and a multichannel pulse height analyser (Figure 2-8). A detector includes a crystal where gamma rays are converted into light pulses and enter into a Photomultiplier tube (PMT). The role of the PMT is to convert a light pulse into a voltage pulse as an output. These voltages are amplified and analysed in a Multichannel Analyser (MCA) and displayed as a spectrum. More discussion related to each component is presented in section 3.3.

2.2 SPECTRAL GAMMA RAY IN CURRENT LOGGING PRACTICE

2.2.1 Spectral gamma tool

As mentioned in previous sections, a spectral gamma-ray toolmeasures the energy of the natural radioactivity of a formation. The measurements are capable of detecting variations in gamma rays associated with the decay of daughter products in potassium (K^{40}), uranium (U^{238}) and thorium (Th^{232}) concentrations individually (Killeen 1997a). Most spectral gamma tools measure gamma rays in an energy range between 0.5 to 2.5 MeV. The effective concentration of K^{40}, U^{238} and Th^{232} are computed in percentage (%), ppm and ppm respectively (Knoll 2010). Analysing a gamma-ray spectrum by separating radioactive sources reduces errors in interpretations. This analytical technique can also be implemented for potassium minerals or uranium exploration (Hoyer and Lock 1971).

Spectral analysis needs to be performed to measure the effective concentration of each of these three radioactive sources. A common spectral analysis is known as spectral stripping. In this technique the measured spectrum is divided into a number of windows, commonly five, then counts of gamma rays are computed for each window, see Figure 2-9 (Marett 1976). Variations in the radioactive concentrations for different formations is well studied in the literature (Hassan 1976). Therefore, spectral gamma measurements can be implemented

to detect different formations. 2-10 shows a schematic example of applying the gamma-ray spectral analysis stripping technique in identifying different formations.

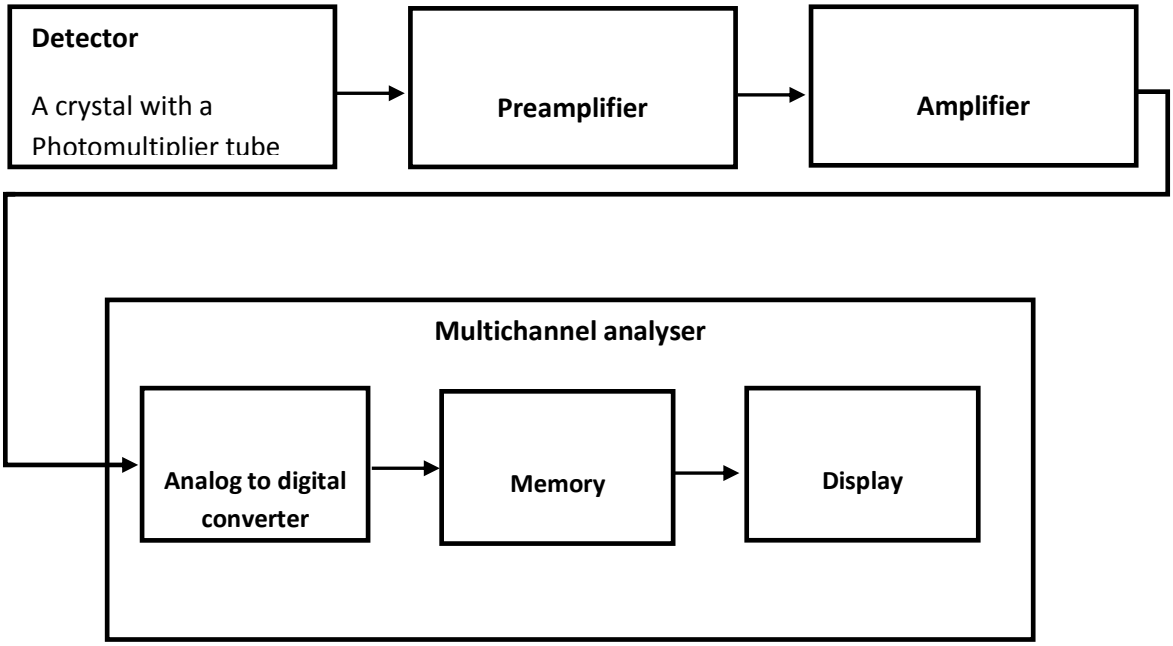

Figure 2-8 Functional diagram of gamma-ray spectroscopy system (Reilly 1991).

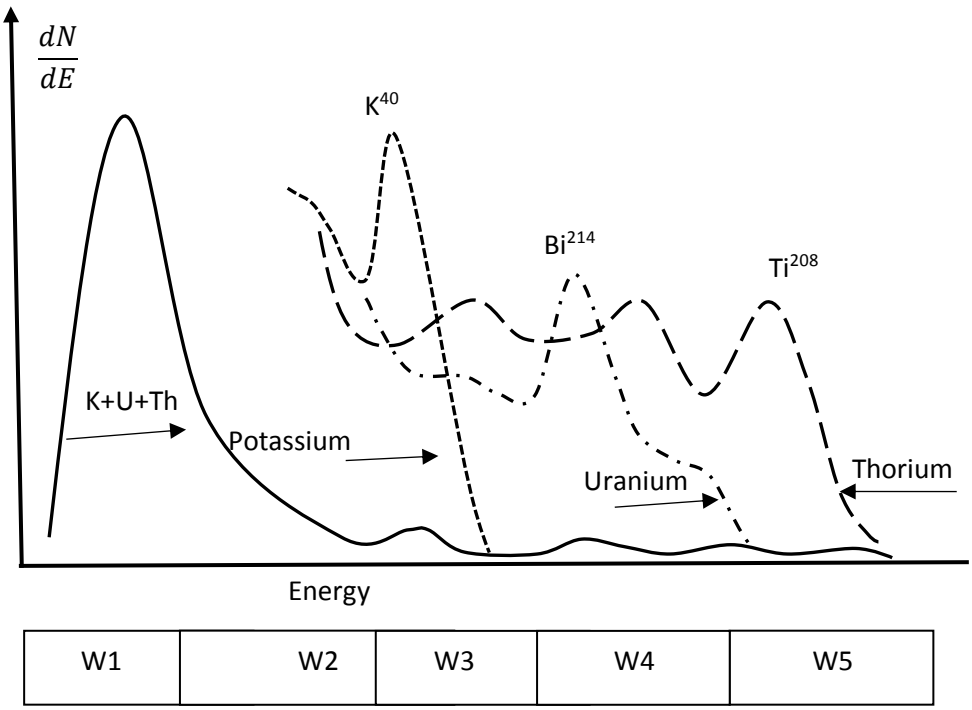

Figure 2-9 A schematic spectrum of natural gamma rays with measuring windows. Five different energy windows are shown on the plot. W1 covers mostly the photoelectric region, W2 includes the Compton area, W3, W4 and W5 select K, U and Th peaks of the spectrum respectively. On the top of the spectrum K, U and Th peaks along with their isotopes are plotted separately.

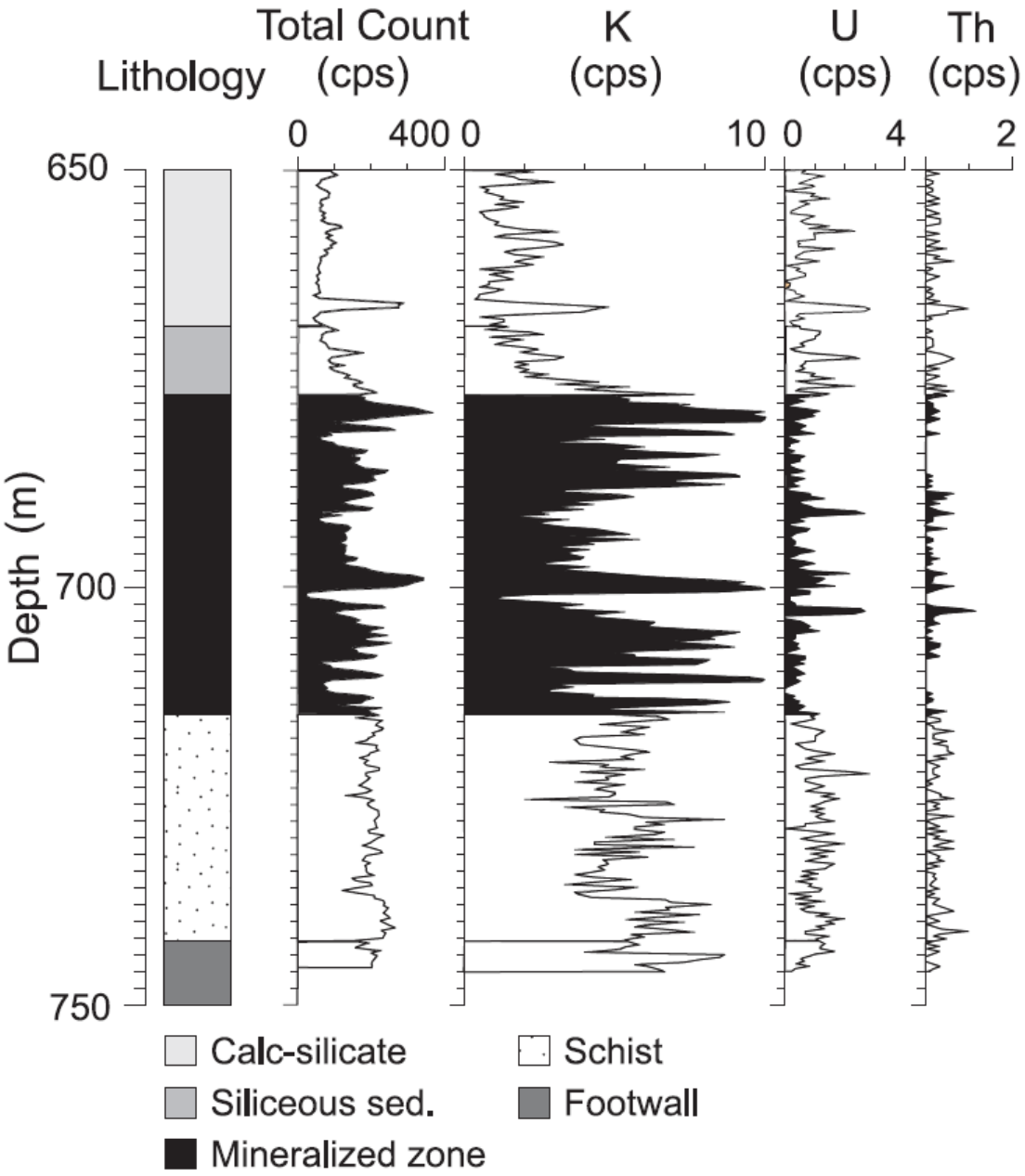

Figure 2-10 Typical responses of the total count of gamma and spectral gamma-ray logs, taken from (Killeen 1997). Spectral gamma log recorded through a mineralized zone in the Helmo gold mining area.

2.2.2 Litho-density tool

The litho-density tool is similar to a formation density tool in that it includes short-spaced and long-spaced detectors. However, the distance between the detectors has been reduced to decrease the statistical fluctuations in the counting rate (Ellis 1985). The litho-density tool normally has a 1.35 Ci radioactive source of Cs^{137} that emits gamma rays at an energy of 0.662 MeV (Bertozzi, Ellis, and Wahl 1981). The source is placed in a way that most of the radiations are injected directly into the formations. A fraction of these gamma rays finally are registered into detectors forming the spectrum (Watson 1983). The detectors are two NaI scintillator crystals with amplifier assemblies, which also include two weak Cs^{137} sources as gain stabilisers (Ellis 1985). For gain stabilising, Cs^{137} peak is kept in the predefined channel during all of the measurements. Moreover applying two detectors is necessary for the mud correction (Stoller et al. 1997). Density can be calculated using empirical equation (2-7) for a long space detector and empirical equation (2-8) for a short distance detector (Ellis 1985):

$$\rho_{LS} = \alpha + \beta\ ln(LS) + \gamma\ ln(Lith), \tag{2-7}$$

$$\rho_{SS} = \alpha + \beta\ ln(SS/\rho_{LS}) \tag{2-8}$$

where LS is the gamma-ray count in the Compton window and Lith is the gamma-ray count in the photoelectric window. These windows are chosen from a spectrum measured with a long spacing detector, refer to Figure 2-11. In the spectrum formed from the short spacing detector, SS is the gamma rays computation in the Compton window, Figure 2-12.

Besides calculating density, the litho-density tool is also used to infer the lithology of formations. It is because low-energy gamma rays, in the photoelectric region, are affected by the atomic number of the elements in the formation they travel through; refer to equation (2-5). In the case where density is constant while Z_{eff} varies for different mediums, the photoelectric part of the spectrum changes with the variation of Z_{eff}, whereas the Compton region remains consistent, refer to Figure 2-11. Applying equation (2-5), the photoelectric absorption cross section (σ_{pe}) is plotted vs the atomic number, refer to Figure 2-13. In this

figure σ_{pe} is calculated for gamma rays with four distinct energy levels and six different elements (Z). The equation (2-5) can be rewritten as follows:

$$\frac{\sigma_{pe}}{Z} = K \times (Z)^{3.6} . \quad (2\text{-}9)$$

σ_{pe} has the unit of barn/atom and Z has the unit of electron/ atom, hence $\frac{\sigma_{pe}}{Z}$ has the unit of barn/ electron. This index is defined as (Bertozzi, Ellis, and Wahl 1981)

$$P_e = (Z/10)^{3.6} \quad (2\text{-}10)$$

.

$$\frac{1}{P_e + C} = c_1\left(\frac{Lith}{LS}\right) + c_2 . \quad (2\text{-}11)$$

P_e is an empirical value (directly measure from a spectrum), which is calibrated using reference formations with known lithology units such as sandstone, limestone or dolomite. Once the calibration curve has been provided, P_e values are calculated and is then used to estimate the lithology variations in boreholes (Ellis 1985). The photoelectric region depends on both the density and elements in a formation, while the Compton area is mostly related to the density of a formation. Therefore, the ratio of Lith and LS windows can eliminate the density effect. The relationship between the P_e and Lith/LS ratio is shown in equation (2-11) (Stoller et al. 1997), where C, c_1 and c_2 are constant. Hence, by calculating the number of gamma rays in Lith and Ls windows from the spectrum and by applying equations 2-10 and 2-11 the elemental composition of the formation can be estimated.

Note that what one can estimate from using the litho-density tool is the effective atomic number of formations, $Z_{eff.}$ In other words, the atomic number of each element with its weight percentage in a formation is considered which are calculated from the equation (2-12)

$$Z_{eff} = \sqrt[2.94]{\sum_{i=1} f_i \times (Z_i)^{2.94}} \quad (2\text{-}12)$$

where f_i and Z_i are the fraction of each element and its atomic number, respectively (Muty 1965).

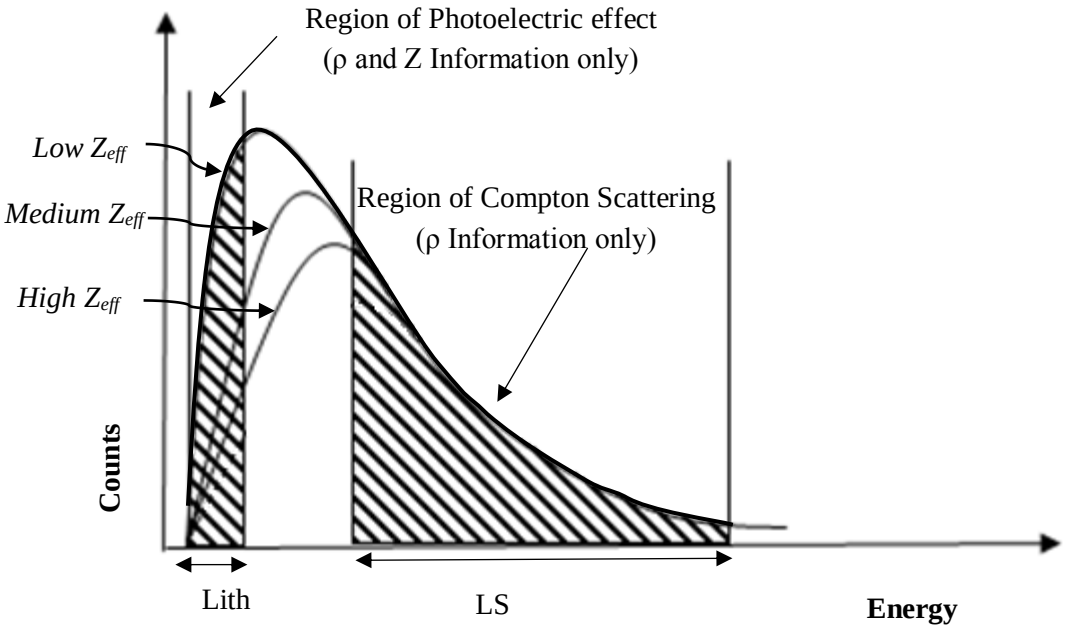

Figure 2-11 Overlaying schematic spectra from formations with different atomic numbers but constant density (Ellis 1985). In the LS window, spectra are merged since the density is the same for all spectra. However, in the Lith window the spectra can be separated based on Zeff variations.

2.2.3 Developments in spectral gamma-ray logging

The most challenging aspect when using the spectral gamma-ray tool is collecting a high-quality spectrum. This is due to the fact that the low natural radioactivity of some areas results in a poor quality spectrum. To tackle this problem some developments have been made on this tool. Improvements have been made in both the system electronics by applying a multichannel digital acquisition, and the detector's efficiency where the conventional 1×12 in NaI crystal is replaced with 2×12 in CsI (Na), which is larger and has a higher density (Mathis 1984).

For increasing vertical resolution, a tool is developed by applying a multi-sensor spectral gamma ray. This tool includes four small 5×10 cm NaI detectors, which are 60 cm apart with an accelerometer to measure precisely based on logging speed. Data from all four detectors that are measured at the same depth are summed to obtain equal effectiveness and increase vertical resolution (Goldberg2001).

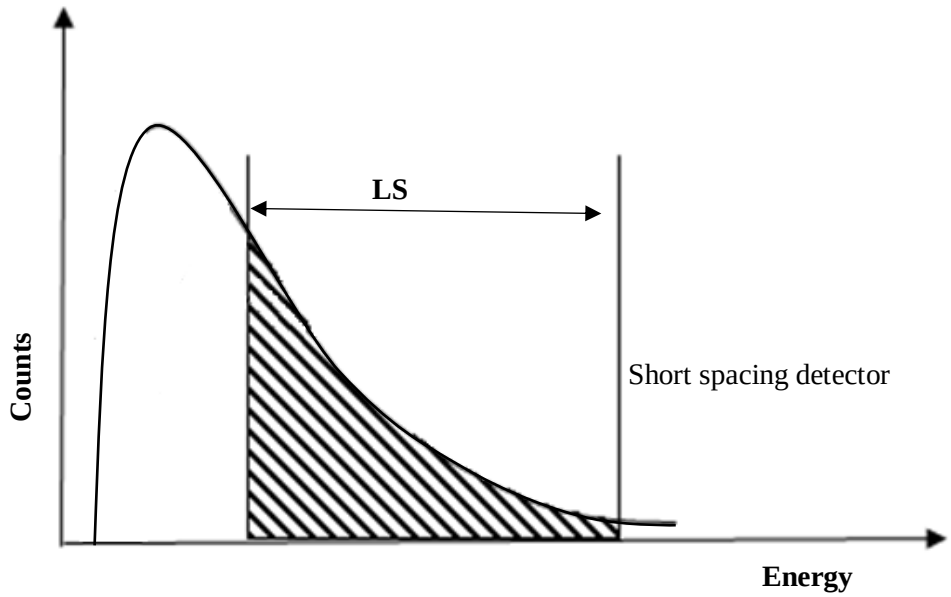

Figure 2-12 Spectrum from the SS detector. The LS window is chosen in the Compton region to calculate the density of a formation. Since this detector is closer to the source gamma rays spend less time in the formation, hence include less information (Gearhart and Mathis 1986).

The other advancement in natural gamma tools is the logging while drilling (LWD) technology. This technology was developed in the petroleum industry; however, this practice is not well appreciated in mineral exploration drilling (Collett et al. 2012). This originates from challenges related to the mining industry, such as the need for smaller inner diameters of drill strings (<100 mm) and budget limitations in mineral diamond drilling (Witherly 2012); (Greenwood 2015). In recent years LWD in diamond drilling has been achieved by applying a new technology called autonomous Auto-shuttle. This technology has been developed in the Deep Exploration Technology CRC (DET CRC) project 2.2. Auto-shuttle is placed with the bottom-hole assembly above the core barrel. It operates during drilling and is retrieved at the end of each drill run along with the rock core (Greenwood 2015). Since the tool spends the same time as the drilling process in a borehole, which is a slow process, more gamma rays can be registered in a detector, which lead to a better quality of spectrum. Therefore, this new technology provides a platform for high-quality data acquisition, which is one of the motivations for this research.

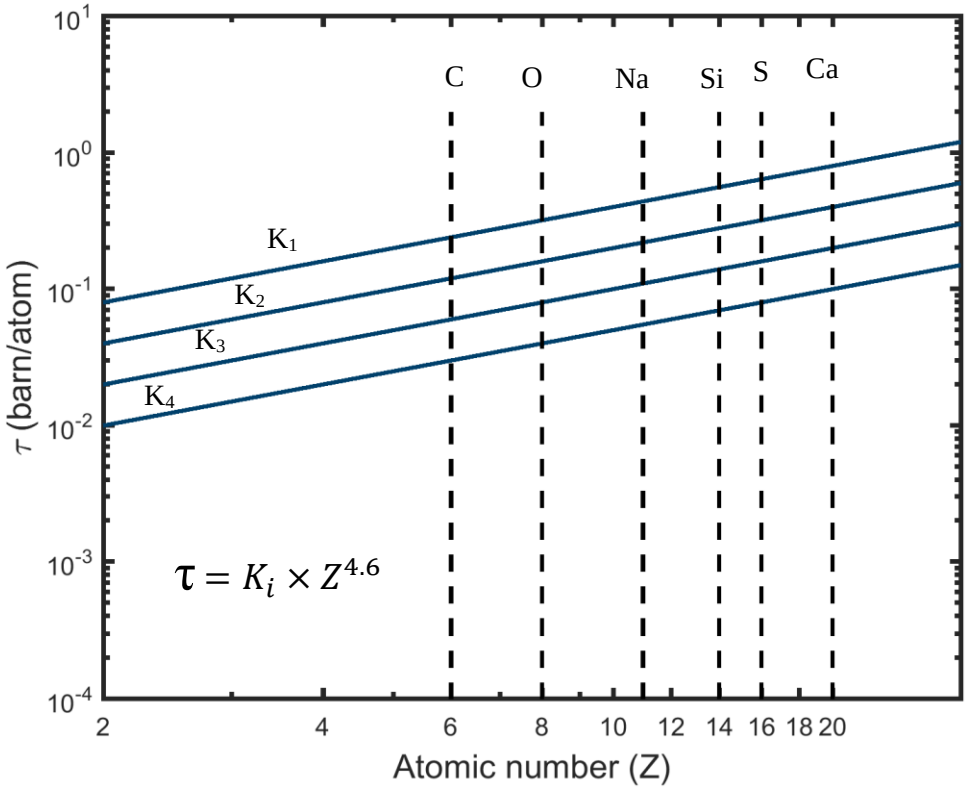

Figure 2-13 Photoelectric absorption cross section (τ) vs atomic number (Z) (Gardner 1980). Six elements, C, O, Na, Si, S and Ca are depicted on the plot. The plot shows that the photoelectric absorption cross section is dependent on atomic numbers and K_i coefficient. Increasing the atomic number results in more photoelectric absorption cross section.

2.2.4 Heavy Metal Indicator (HMI)

In situ assessing the base metals has been practiced and is well covered in the literature (Killeen 1989). The method of applying the ratio of two different parts of the spectrum, high-energy over low-energy windows, to determine the alteration in the atomic number of formations is not a new approach (Killeen 1997a); (Bertozzi, Ellis, and Wahl 1981); (Ellis 1988). Killeen has done much work related to this subject in the mining area; however, all of his research is based on using a radioactive source. As we discussed in the background physics in previous sections, the ratio of high to low energy parts of a spectrum is a good factor for determining the lithology of the formations. In this research the concept of SGG ratio, as it is named (Killeen 1997a), is exploited to advance further in heavy metal investigation. The spectral analytical technique improved in this research (the HMI method) is also based on calculating the ratio of different windows of a spectrum. However, there are some other aspects covered in this research. Our method is relies on natural gamma spectra.

We took advantage of the new shuttle technology to acquire a high-quality gamma-ray spectrum, which is essential for our analysis. The common method for processing the natural gamma spectrum in the mining industry is via stripping cross-element interference and removing the background. In this method only the three radioactive elements of K^{40}, U^{238} and Th^{232} are extracted from a gamma-ray spectrum. In this research, we apply the HMI technique to analyze natural gamma spectra.

The HMI technique is based on the ratio of gamma counts in a section of the Compton region region (the Compton window) and a section from the photoelectric region, (the photoelectric window) of the spectrum. A key aspect is the correct choice of these windows. The first step in developing this technique is determining the Compton window. For this purpose, we considered parts of the spectrum where natural radioactive sources (K^{40}, U^{238} and Th^{232}) and their isotopes are avoided. Studying a typical gamma ray measured from a rock shows that choosing the 250 to 500 MeV part of a spectrum for the Compton window is very suitable as a starting point. This window can be a good choice since major isotopes of a radioactive source are avoided (

Figure 2-14). Next we normalised the whole spectrum over this window to guide us to the choice of a second window, the photoelectric window. The best choice of a photoelectric window is where the normalised spectra are well separated. To illustrate six spectra measured in media with different elemental compositions and normalised over Compton windows are overlaid in

Figure 2-15. This shows that spectra are separated to a convergence point where all overlay on the same line. Therefore, the photoelectric window starts from 50 keV to the point of separation. We do not select a window with less energy than 50 keV, as it may be contaminated with system electronics. If we cannot find a separation point on the overlayed spectra, the spectra are not reasonably distinguishable; we should then change the Compton window and repeat the whole process to achieve a desirable photoelectric window. Once both windows are selected, gamma rays are counted for each window and their ratio is calculated. The calculated values, which we named HMI values, can then be interpreted to reflect the variations in the lithology of formations.

The suggested windows for the photoelectric and Compton windows (50-200 keV and 250-500 keV respectively) are practical in most cases but these windows are subjected to change. In order to achieve the best result, which refers to achieve better resolution in indicating the

heavy minerals, all steps explained in the previous paragraph should be taken to choose the windows.

Another new approach for analysing the natural gamma-ray spectrum was also attempted where the radioisotope concentration was to be normalised to produce an estimate of density. This technique, called CPR (Compton Scattering to Peak Ratio), is based on a ratio of the Compton window over the potassium peak. It assumes most of the radioisotopes are from potassium. The results of this work were inconclusive, and largely unfinished as it was becoming a whole thesis in itself; with lab studies showing some potential and airborne analysis producing inconclusive, or counter-intuitive results. In Appendix A this work is discussed in more detail.

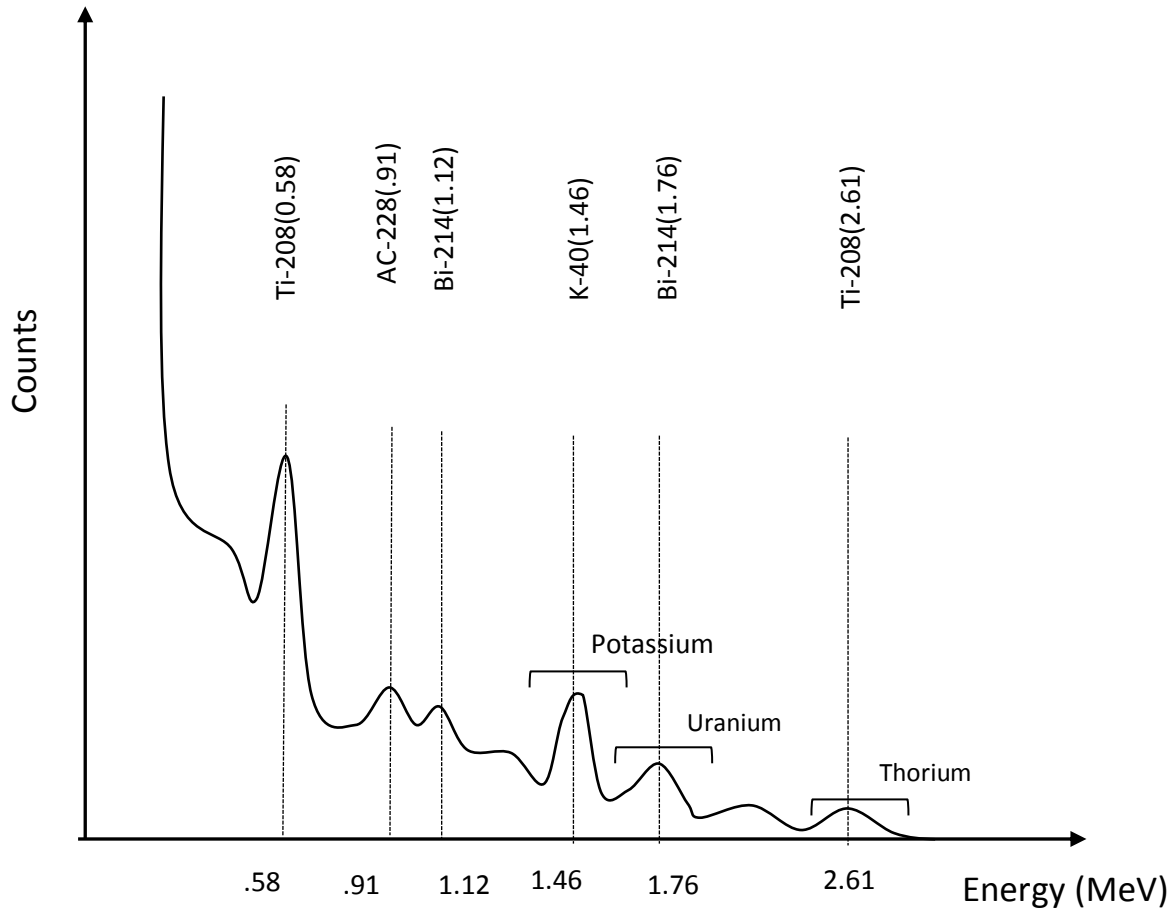

Figure 2-14 A typical natural gamma-ray spectrum showing the K, U and Th energy windows and the energies of their major isotopes (Minty 1992) ; (Blum 1997). It is important to consider significant radioactive isotopes (parents and daughters) for choosing Compton and photoelectric windows.

.

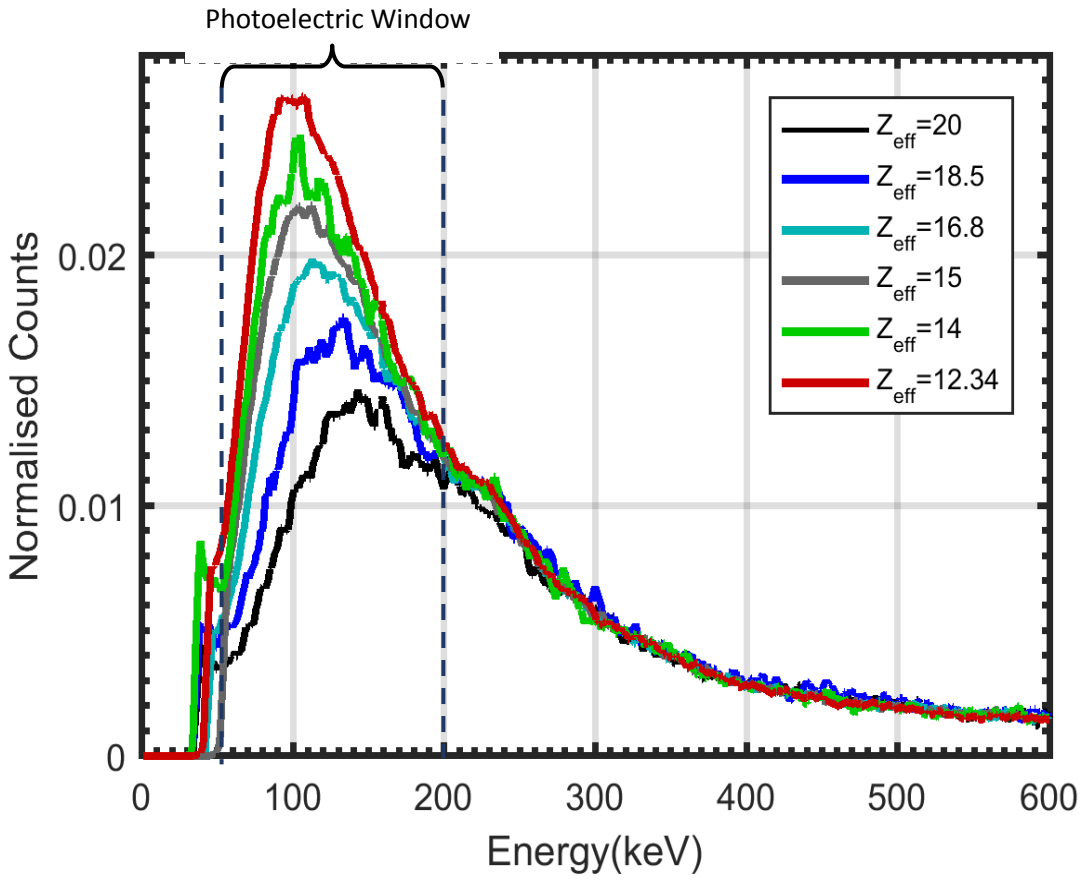

Figure 2-15 Laboratory spectra from media with different effective atomic numbers, normalised by the value in the Compton window, which helps in choosing an appropriate photoelectric window for subsequent analysis. The part of the spectra that is separated the most is selected for the photoelectric window.

CHAPTER 3. GAMMA SPECTRUM ANALYSIS - HMI

3.1 COMPUTER SIMULATION

In this research, we carried out Monte Carlo calculations using GEANT4 to study new methods in the analysis of gamma-ray spectra. GEANT4 is a simulation tool kit which was created by an international cooperation of institutes and laboratories in experimental physics (Agostinelli 2003). GEANT4 is a comprehensive software package for modelling in High-Energy Physics (HEP). It provides a wide range of physics processing tools to simulate the behaviour of particles during interaction and passage through matter (Apostolakis et al. 2000). Its ability to handle particles transported through complex geometries, offers the user the ability to design models with different geometries, shapes and materials. The main objective of this chapter is to implement GEANT4 simulation to derive gamma-ray spectra, forming from their interactions with media with different geometry, compositions and density then test the validity of the introduced methods to analysis the spectra. For this purpose, we built C++ classes to describe the geometry, materials, detector, the primary particle generator (such as particle position, energy and type) and all important physics to be modelled.

In this study different models are designed to simulate measurements under various borehole conditions. All models were simulated by applying GEANT4's various geometry and elements. For the sake of visualisation, the basic structure used in each model is plotted schematically in

Figure 3-2. Each model consisted of a rock, a borehole, a detector and a source that were all located inside a big volume named "the world volume". In order to design each model the following steps were taken: First, we determined "the world volume", a cube with dimensions 3 × 3 m, filled with air. The world volume provided an encapsulating environment where all the model structures are placed inside. The centre of the world volume is the reference point where all parts of the model (a borehole) are placed in with the respect to this reference (

Figure 3-2). Second, a detector was placed in the centre of the world volume and was parallel to all other structures such as where the borehole and rock were located. In our model, the detector is simply the scintillator crystal. It was not necessary to model the actual scintillation process, or the optical photon collection by the photomultiplier tube. We were only interested in the energy deposition spectrum resulting from gamma ray – matter interactions prior to getting to the detector. The same detector was applied for all models: a BGO crystal with dimensions 1.75 cm in a radius and 5 cm in height encapsulated in an aluminium case with the same height and 3 mm thickness. A BGO crystal was chosen as the scintillator detector crystal, since the high density, 7.1 g/cm^3, satisfied the need to capture as many gamma rays as possible in the crystal (Kepic et al. 2015). Other parameters such as borehole geometry, rock geometry and materials in the model are detailed in the following sections.

The rock formation is considered homogeneous in composition and in radioactive concentrations. For all models, the chosen radioactive source was K^{40}, evenly distributed within the medium with an isotropic radiation pattern. As explained in section 2.2.1, the main natural radioactive sources are K^{40}, U^{238} and Th^{232} with K^{40} associated with the most abundant element of these natural gamma-ray radioactive elements on the upper part of the earth's crust with an amount of 2.7 %, compared to uranium 2.5 ppm and thorium 10.5 ppm (Ahrens 1995). Moreover, K^{40} has the simplicity of a single gamma-ray energy emission with no daughter products, while U^{238} and Th^{232} have 346 and 458 discrete gamma-ray energies in their decay series, respectively (Maučec et al. 2009). Including all natural gamma-ray sources (K^{40}, U^{238} and Th^{232}) made designing the model much more complicated and also slowed down the computation time, without adding any significant outcome. Therefore, only K^{40} is used as a radioactive source in the modelling since it is significantly more abundant in the earth, simpler in simulation and speeds up the computations and learnings.

GEANT4 (Monte Carlo) simulations were initiated with gamma rays with energy of 1460 keV (K^{40}) generated from a single point source at a random location in the rock. Gamma rays start off in a random direction and intract with the surrounding rock; the most important interactions are the photoelectric process, Compton scattering and pair production (production of an electron and positron). In the last stage, the tracked gamma rays are registered in the detector. The gamma rays are tracked in the Monte Carlo simulations and end in the following main processes:

- Gamma rays deposit all their energy after their interaction with the rock, the borehole and the crystal.
- Gamma rays deposit some of their energy in the crystal and get photo-electrically absorbed into the rock.
- They deposit some of their energy in the crystal and exit from the world volume.
- Gamma rays scatter in the rock and without having any interaction with the crystal escape from the world volume.

Model building was made-up of three main steps or components:

1- Detector: The detector was a cylindrical shaped crystal, 1.75 cm radius and 5 cm height, with the physical properties of BGO and was placed in the centre of the world volume.

2- Borehole: It had a cylinder shape geometry positioned in the centre of the world with dimensions of 21 cm height and 5 cm in radius. The detector was centered inside the borehole. In some early models, the borehole wall was designed to be composed of polyvinyl chloride (PVC) and filled only with air.

3- Source (Rock): As described before, a gamma-ray source was an isotropic emission, mono-energy K^{40} that was distributed homogeneously in the rock. Rock geometry was described as a cylinder and placed surrounding the world volume with its centre at the reference point. Generally, most of my experimental simulations involved changing the rock materials in the simulations with different density and elemental compositions.

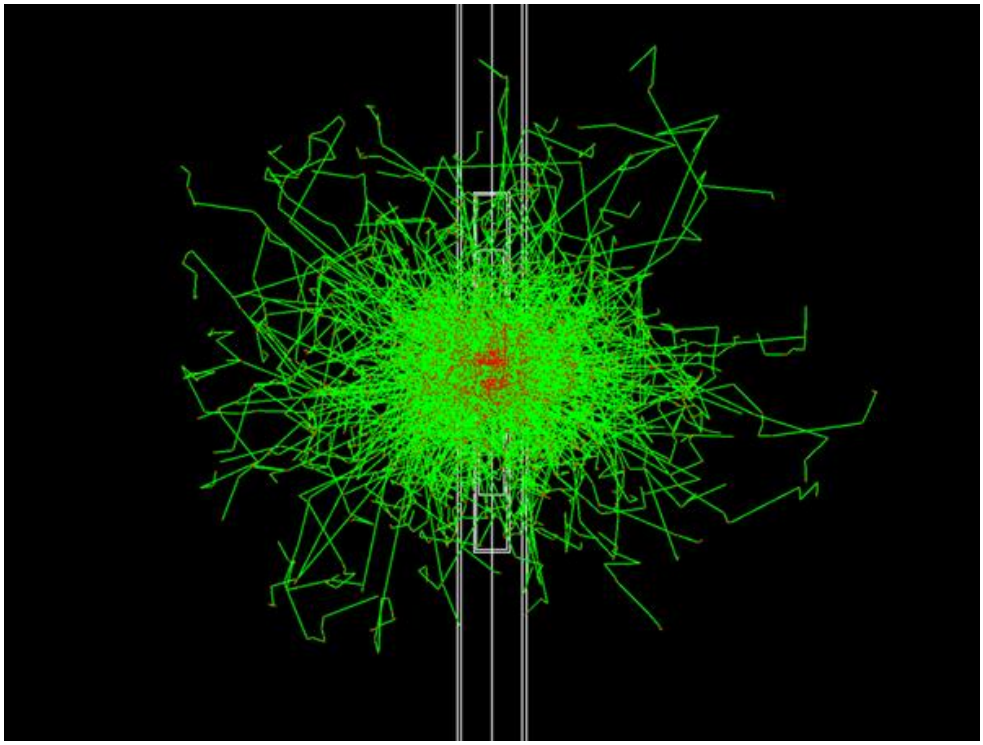

Figure 3-1 A plot of gamma rays interactions (green lines) and deposit in the detector crystal (red region). The white rectangular in the centre is a rock.

Apart from some airborne simulations discussed in appendix A, the first two steps were the same for all models, and the parameters of the rock were varied in step 3. The outputs of the GEANT4 simulations are lists of the energies deposited by gamma rays in the detector volume to form the gamma-ray spectra. Afterwards the gamma spectra were analysed to investigate the HMI measure for the further analysis of the spectra.

3.2 HEAVY METAL INDICATOR INVESTIGATION

3.2.1 Simple borehole model with variable composition

This section discusses how we studied the potential of the HMI measure to predict variations in the atomic number of rocks that gamma rays travel through. To this end, we simulated the models keeping all the parameters the same except for the atomic number of the medium (rock). The overall model included a detector and a borehole with make-up as described in the model building in the previous section. The medium (rock) was a cylinder shape with dimensions of 15 cm radius and 21 cm height located in the centre of the world.

For simplicity, all models were simulated to consist of a mix of iron and cement with different concentrations. This simple choice of material for the mix enabled us to verify them later experimentally. The effective atomic number of the rocks changed by varying the ratio of these two main material proportions. A list of materials used in these models, including their elemental compositions with their percentage and density are presented in Table 3-1.

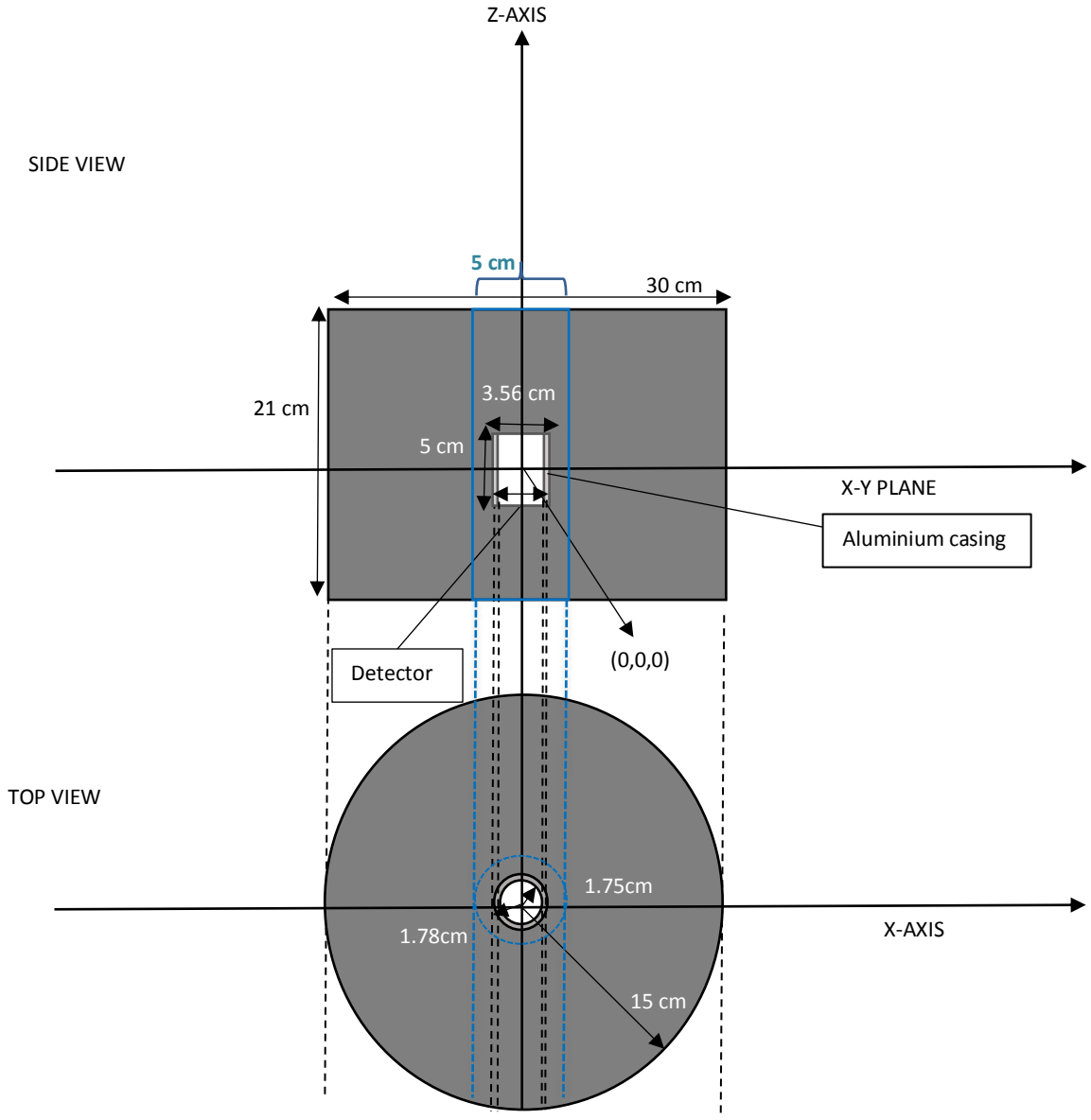

Figure 3-2 Schematic figure of a fundamental structure of a model. It consists of a BGO crystal as a detector, a borehole and a rock, which are all located in the centre of the cubic.

	Materials	Elements		Density
		E	**%**	**g/cm3**
Rock	cement	Si O H Ca Al Fe	22 60 0.9 0.4 0.1 0.02	2.6
	Iron	Fe	100	
Detector	BGO ($Bi_4Ge_3O_{12}$)	Bi Ge O	21 16 63	7.13
Borehole	PVC (C_2H_4)	C H	14.37 85.62	0.946
Detector housing	Aluminum	Al	100	2.7

Table 3-1 List of materials used in the computer simulations. Elemental compositions, percentages and density of the materials are presented.

The initial model contained 10% iron and 90% cement. Then the iron gradually increased in percentage in steps of 10% to reach 70% concentration for iron and 30% for cement. Variations in iron concentration realistically resulted in significant changes in the average atomic numbers (Z_{eff}). Hence, we had 7 models with different $Z_{eff,}$ ranging from 12.5 to 21.5. The rock density for all of the models was kept the same as in 2.6 g/cm^3 (which is not realistic, but allowed us to consider one aspect at a time). The source gamma rays were K^{40} that were uniformly distributed in the rock. To improve the quality of the resulting simulated gamma spectrum each simulation modelled the interaction of $5x10^7$ gamma rays. The simulation tracked each gamma ray until it was either photoelectrically absorbed or exited the

world volume. Gamma rays can scatter and get absorbed in all regions of the model formation and detector. However only those gamma rays that deposited energy in the scintillator were recorded.

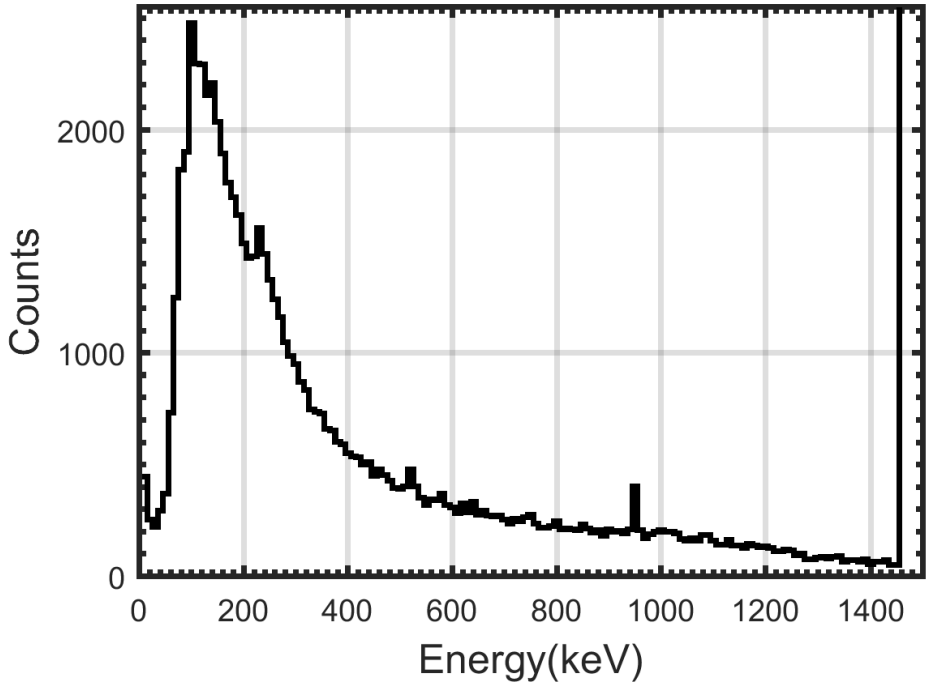

Figure 3-3 is an example of a simulated spectrum, where the x-axis is the gamma rays' energy deposited in the detector and the y-axis is the number of gamma rays with that energy. Since gamma rays all started with energy of 1.46 MeV, the maximum energy of a gamma ray in the spectrum could not exceed this amount. For all of the models, calculated HMI values are computed and plotted versus Z_{eff} in Figure 3-4. A double x-axis was used to demonstrate the dominant role of increasing iron on Z_{eff} values, which for every 10% increase in iron concentration added 1.5 to the Z_{eff} values. Iron has a relatively high atomic number compared to the silicates and Al, Na, Mg and other major constituents of rocks. As expected, the HMI values varied significantly with $Z_{eff,}$ with a linear fit and strong correlation coefficient (R^2= 0.99).

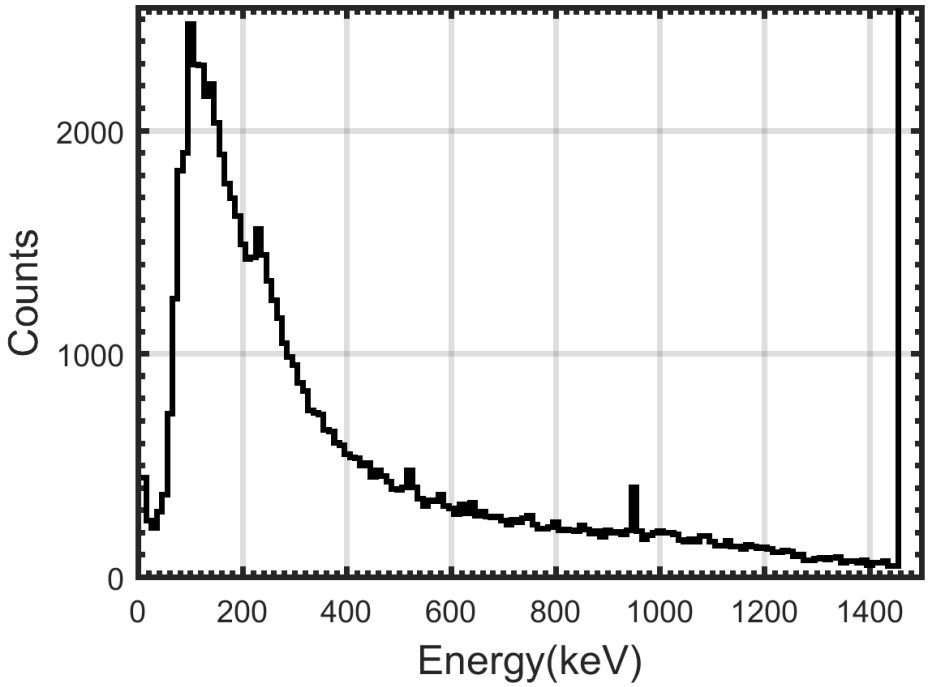

Figure 3-3 A spectrum from the simulated model. Notice that no gamma ray exceeds the initial energy 1460 keV. For the spectrum to be more visible, gamma-ray counts at energy 1460 keV are not shown.

To calculate the HMI two energy windows were used: from 50 to 200 keV for the low energy photoelectric sensitive region, and 250 to 500 keV for the high energy Compton sensitive region. Both window regions are equally sensitive to electron density (almost the same is gravimetric density); thus this factor is normalised out when the ratio is evaluated leaving only a dependency upon Z_{eff}. The method for calculating HMI values is explained in section 2.2.4 in more detail. The calculated errors were very small at about 1.1%, which were due to the high gamma- ray counts in the gamma-ray spectrum (leading to high precision). For the last two models the iron concentrations were very high which resulted in higher Z_{eff}, thus the error increased to 1.3%, which was still small. The increase in error was due to increases in $Z_{eff,}$ which lead to less counts in the spectrum, as more gamma rays were absorbed in the rock before being registered in the detector.

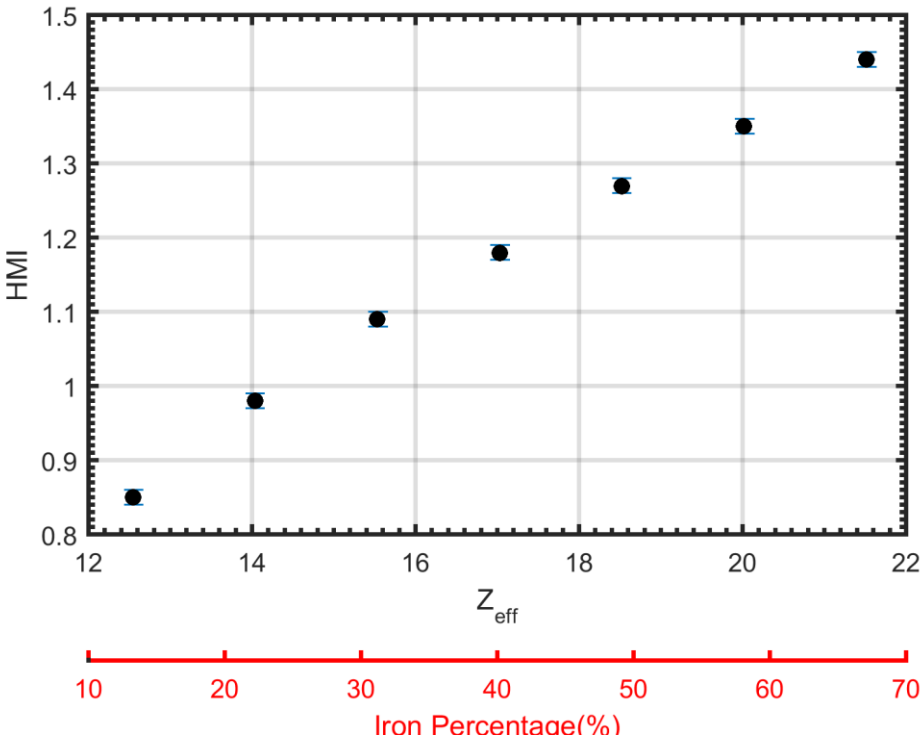

Figure 3-4 HMI values calculated for the models with different Z_{eff}. On the x-axis, both iron percentage and Z_{eff} are shown for each model. It shows that the increase in the iron percentage causes a linear in Z_{eff} values. HMI values vary with Z_{eff} as well as iron concentration.

The results plotted in Figure 3-4 demonstrate that for cement-rich rocks with iron HMI values increase linearly with increases in Z_{eff} with a significant correlation of $R^2 = 0.99$. Such a result might be expected from theory since the probability of photoelectric absorption (in the low energy part of a spectrum) is directly related to Z_{eff} (Knoll 2010) and that the iron can only realistically be present from 0 to 60% (pure iron oxides). Our computer simulations show that the HMI can resolve changes in ΔZ_{eff} of 1.5 with better than 95% accuracy. Hence, the HMI should be sensitive to Z_{eff} variations. Also, variations in iron concentration amongst the common elements, has the greatest impact on Z_{eff}. The GEANT4 simulations shown in Figure 3-4 suggest that the HMI should be mostly related to the iron content. However, these encouraging simulation results are generated from very simple models.

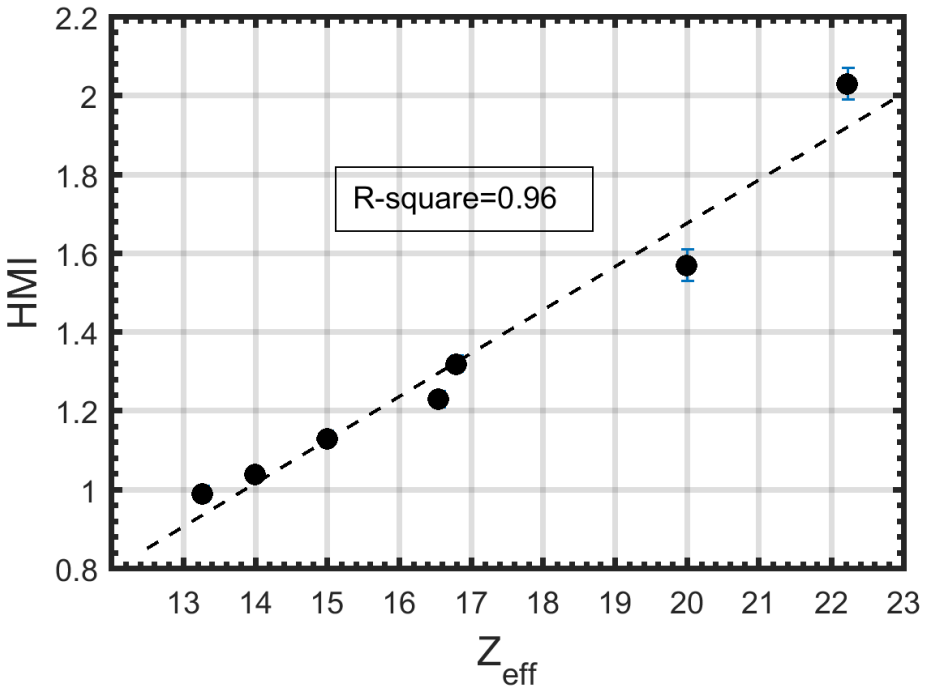

Figure 3-5 HMI ratio calculated for simulated models with different average atomic numbers ($Z_{eff.}$).

3.2.2 Are HMI and Z_{eff} closely linked for earth-like materials?

In this section, we investigate whether the HMI values calculated from the spectra derived from the computer models, will provide similar values for the same Z_{eff}, even if the mixture of materials is slightly different. To test the idea that the HMI is only linked to Z_{eff}. I synthesized rocks with different compositions, that could be later be verified under laboratory conditions. The models were designed in a testable laboratory scale size and included materials that could be easily gathered (section 3.3.2). The geometry of the models were identical and the same as those discussed in section3.2. Each model consisted of a mixture of materials such as barite, sand, iron, pyrite, zinc and cement to provide some variety in mixtures indicative of "natural" minerals.

Table 3-6 summarises the elemental composition for each model simulated. We chose materials based on their availability for laboratory experiments. Hence all models contained some potassium sulphate (potash) to ensure sufficient natural radioactivity for the experiments (otherwise the background radiationm in the lab would dominate or alter the measurement significantly).

Models	Materials name	Materials in %	Average Atomic numbers	HMI values	HMI errors
Cement	Cement	67.22	13.27	0.99	0.01
	Potash	32.78			
Zinc2	Zinc	17	14.00	1.04	0.01
	Sand	63			
	Potash	20			
Zinc1	Zinc	30	15.00	1.13	0.01
	Sand	50			
	Potash	20			
Pyrite	FeS_2	30	16.55	1.23	0.01
	Sand	50			
	Potash	20			
Zinc3	Zinc	60	16.80	1.32	0.01
	Sand	20			
	Potash	20			
Iron	Cement	35.56	20.00	1.57	0.02
	Potash	20			
	Iron	39			
Barite	Sand	70	22.22	2.03	0.02
	Potash	20			
	Barite	10			

Table 3-2 List of simulated models with their materials, Calculated Average Atomic numbers, HMI ratio and estimated relative error.

An isotropic and homogeneous gamma ray emission from K^{40} was modelled with energy of 1.46 MeV. Before running the simulation an average atomic number ($Z_{eff.}$) of each

model was computed based on the equation (2-12). Overall, 7 simulations with Z_{eff} ranging from 13 to 22 were performed with GEANT4. This range is where the Z_{eff} of most rocks should fall (Hart 1969). The geometry for all models was the same: a cylinder 21 cm in height and of 15 cm radius. The detector was a CsI crystal of 35 mm radius and 110 mm in height placed in the centre of the rock (

Figure 3-2).

The spectra generated from the simulations were used to calculate HMI values for each composition. HMI values were computed with the same energy windows that were used in the previous section: 50-200 keV for the photoelectric region and 250-500 keV for the Compton region. As the gamma counts were reasonably high for each spectrum (more than 40,000 total gamma-ray counts per spectrum) the statistical errors (arising from the Monte Carlo methodology used in the GEANT4 simulations in generating the HMI values) were not significant.

The results of HMI versus Z_{eff} for the various mixtures are plotted in Figure 3-5, these results are very similar to the binary mixtures shown in Figure 3-4. Similar to the study of binary mixtures there is good agreement between the HMI values and Z_{eff} for the various mixed element simulated models, where a linear fit with correlation co-efficient is R^2=0.96. Therefore, different elemental compositions with the same Z_{eff} provide the same HMI values. This is not entirely predictable as the formula for Z_{eff} is a summation of the various elements, of atomic number Z, to some power and not a linear weighting of Z values. For most rocks with relatively low average Z values in the mixture the linear link between HMI and Z_{eff} is reasonable, but that may not be the case with mixtures of base metal sulphides. Additionally, HMI values are independent of density of the rock since the density is kept constant in the modelling.

3.2.3 Modelling the effect of steel casing (or Rods)

When considering the measurement of the HMI, there is an additional aspect worth considering: the effect of the steel outer drill rods or casing. In all previous models, the borehole wall was made of PVC and without a steel casing. However, if we are to consider sensor systems, such as the DET CRC Auto-shuttle system that measures gamma rays whilst

in the drill-rods, then the effect of steel and the relatively heavy elements close to the detector also needs to be considered. The use of a relatively low-energy window, 50-200 keV, for a HMI calculation comes with issues of interference from other borehole materials and structures. This low energy region is more easily absorbed by barriers such as the steel casings of a borehole or the outer drill rod surrounding of Auto-shuttle/sonde sensor. Boart Longyear Q drill rods are a popular choice for diamond coring drills and are used worldwide (Longyear 2009). Important size attributes of these rods are presented in

Table 3-3. For the most common rods, the thickness varies between 4.5 to 5.5 mm, which is a relatively narrow range. To evaluate the significance of a steel barrier in biasing HMI values (to higher values assuming that steel has a higher effective Z than the average rock), simulations of 5 models with steel thicknesses of 4, 5, 8, 10 and 13 mm were performed. This range covers rod thickness variations plus additional casing thicknesses (generally, we would expect mostly just the drill rod rather than the drill-rod and casing).

Rods	OD (mm)	ID (mm)	Thickness (mm)
BQ	55.6	46.1	4.75
NQ	69.9	60.3	4.8
HQ	88.9	77.8	5.55

Table 3-3 Different Rods specifications (Longyear 2009).

The simulation model parameters such as geometry and source distribution were the same as in previous models. Regarding earth materials, all of the earth models were composed of some zinc-sulphate silicon and potash, with a lot of silicon-dioxide. For all five earth models, the only variable to be changed was the thickness of the steel case/rod. Spectra generated from these models indicated an overall drop in total gamma-ray counts with increasing steel thickness. However, there was relatively more reduction in counts in energy

channels from 50 to 200 keV, the region where the photoelectric absorption of gamma rays was significant compared to other mechanisms of gamma energy loss, which is displayed in Figure 3-6. The impact of the steel rods or casing on the photoelectric region was visually evident. However, to what degree was the effect significant in a quantitative sense? To analyse the effect of the steel casing the HMI values were computed for models with different steel rod/casing thicknesses as shown in

Figure 3-7. In this plot HMI values are presented in two different colours. The first colour is dark blue, which represents the HMI value for a model without any casing. The black dots demonstrate the HMI calculated from models with different steel thicknesses. The results indicate that HMI values do change with the steel thickness, and the change with increasing thickness is fairly linear for thicknesses less than 6 mm where the effect tends to plateau. Increases in steel thickness attenuate the gamma rays in photoelectric regions more than the higher energy (and more penetrating) Compton region. As HMI is a ratio of Compton counts versus Photoelectric counts in two windows, the effect of the steel is to increase HMI values as the steel is now part of the "environment" and of a higher average atomic number compared to most rock. In

Table 3-3 the thickness of the three most common drill rod sizes have similar steel thickness; thus, we can use a correction factor common to the NQ size to remove the effects of the nearby steel. In addition, it should be noted that the reduction in gamma signals which means that measurements performed within the drill string will have less "contrast" in HMI values (and more noise due to reduced signal) is due to the nearby amount of Fe in the steel

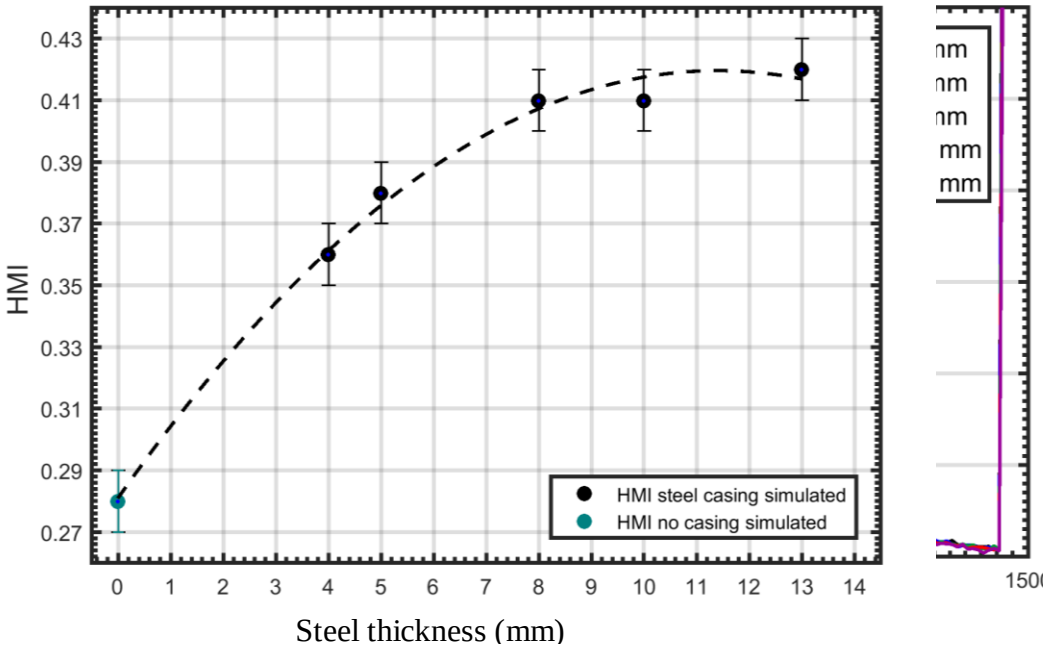

Figure 3-6 Spectra form models with different steel casing thickness. Increasing the thickness principally reduces gamma-ray counts in the photoelectric region.

Figure 3-7 HMI values for different steel casings. For thickness less than 5 mm, HMI values are not affected with casing with one sigma errors. The dotted line indicates the trend of data.

3.2.4 Minimum number of gamma rays for a usable spectrum

One of the most important measures of the quality of the gamma spectrum are the total number of gamma rays that form the spectrum. The counting statistics (or the natural variations in the energy windows) in a spectrum determine the minimum detectable signals for K, U, Th elemental concentrations and the level of precision in measures such as HMI. Therefore, what is the minimum number of gamma rays in entire a spectrum (total gamma-ray counts) so that we can usefully apply to calculate a reliable HMI values? To address this question, we generated artificial spectra, each with a different number of counts, randomly forming a gamma-ray spectrum measured in the laboratory. The number of total counts ranged from 10^3 to 10^6 per spectrum and for each spectrum HMI and its error were calculated. In Figure 3-8 we plot HMI fractional error (HMI error over HMI values), which is calculated for every spectrum versus the number of gamma rays in the spectra. We observed, for spectra with more than 200000 gamma rays, that the HMI fractional error does not change

significantly by increasing the counts in the spectra. The fractional error only improves by 0.5% by increasing the number of counts from 40000 to 200000. Therefore, 40000 statistical counts provide a sufficiently good spectrum for HMI analysis.

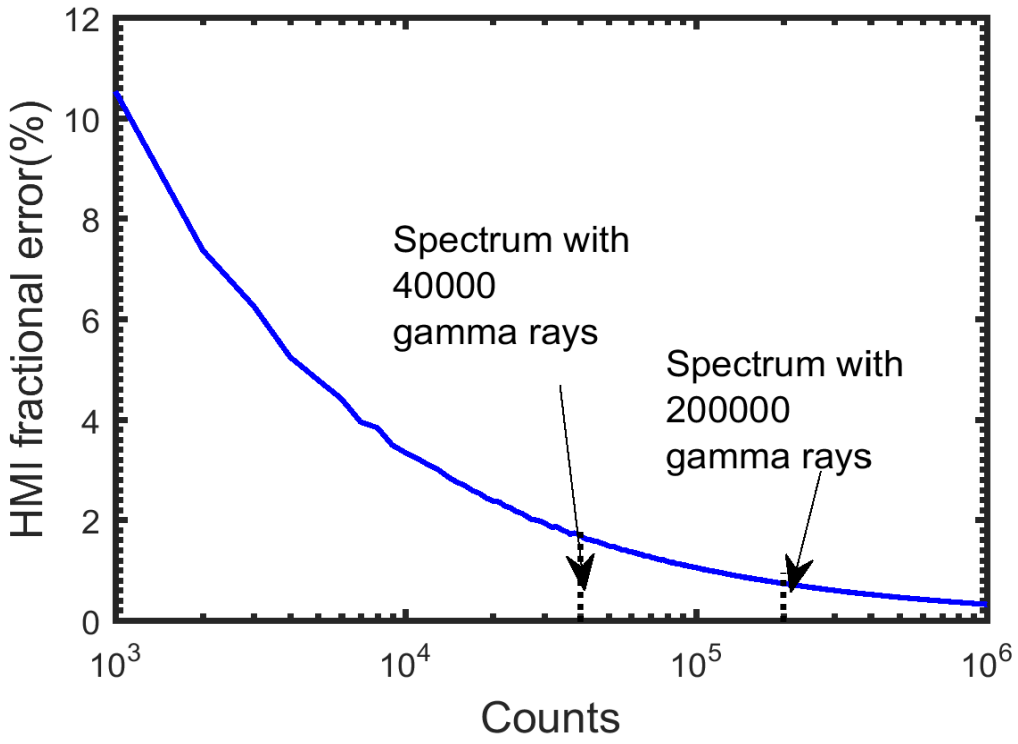

Figure 3-8 HMI fractional error versus counts in spectrum. Increasing gamma rays in a spectrum results in decreasing the fractional error to a point where very little further benefits results, at about 200,000 counts.

3.3 LABORATORY TESTS FOR HMI

3.3.1 Model constructor parameters

The first set-up of the experiments was designed to verify the HMI simulation results. As we explained in section 2.2.4, HMI values change with variation in atomic numbers of the medium of interest. Therefore, we designed boreholes that could be constructed in our laboratory. While simulated models has only included a scintillator crystal, in laboratory measurements, we applied a detector consisting of a scintillator crystal, a photomultiplier tube (PMT) and a multichannel analyser, which we will explain briefly in the following sections.

3.3.2 Scintillators

When gamma rays enter into certain materials, it produces scintillation light. The illuminating characteristic of these materials is being exploited to detect gamma rays (Knoll 2010). There are different types of scintillation materials however the ones we are particularly interested in are classified as inorganic crystals. A good scintillator crystal should have features such as high efficiency and linearity in converting the kinetic energy of a charged particle into measurable light (Grabmaier 1984). The other parameters that should be taken into account for choosing a crystal are good thermal stability, high stopping power and high density (Kepic et al. 2015). Not every scintillator contains all these parameters, however common inorganic scintillators such as NaI(TI), CsI(TI), CsI(Na), BGO, $ZnWO_4$ and $CdWO_4$ offer better conversion efficiency than the organic scintillators, a high probability of photoelectric effect and high absorption efficiency (Hamamatsu 2007).

To provide better insight as to how to select a scintillator crystal the typical specifications required are summarised in

Table 3-4. The last column, in the table indicating the light yield in photons, provides an estimation of the total number of photons produced from the deposition of 1 MeV of energy of a fast electron. The decay times of the different crystals are presented in column four, it shows that the shorter the decay time the more gamma rays can be registered. A crystal with high density can provide more gamma rays captures, see the second column in

Table 3-4. A reflective index is desired to be close to the glass reflective index (1.5) to provide better coupling with PMT. Comparing the listed crystals specifications shows that $ZnWO_4$ has a higher scintillator efficiency, and it can be used on thin screens since it is provided as a polycrystalline powder. BGO is another good choice for detecting gamma rays, since it has high density, 7.13 g/cm^3 and a short decay time. $CdWO_4$ could also be considered as a good candidate since it has the highest density, however a major drawback is that it has a very slow decay time. Therefore, it is best used when the counting rate is not high. NaI(Tl) shows very good light yield. Its non-proportionality behaviour is less in comparison to other inorganic scintillators. Its decay time is highly dependent on the temperature of the environment as such it responds faster at higher temperatures. CsI scintillators come with two different types of CsI(Tl) and CsI(Na) which show very different characteristics. CsI(Tl) has

a long decay time compared to CsI(Na). On the other hand CsI(Na) yields in a spectrum similar to NaI(Tl) (39000 and 42000 Photons/MeV for CsI(TI) and NaI(Tl), respectively) while CsI(TI) has higher density than NaI(Tl) .

Crystal	Density	Reflective Index	Decay Time(μs)	Light Yield in Photons/MeV
NaI(Tl)	3.67	1.85	0.23	42000
CsI(TI)	4.51	1.8	0.68	65000
CsI(Na)	4.51	1.84	0.46	39000
BGO	7.13	2.15	0.3	8200
$ZnWO_4$	7.8	2.2	44	8000
$CdWO_4$	7.9	2.3	11	15000

Table 3-4 The scintillation properties at room temperature of a collection (Knoll 2010).

In our experiments we examined different crystals to select the best choice of scintillator crystal for the measurements, see Figure 3-9 (Kepic et al. 2015). We initially chose BGO as a scintillator crystal; however, during our laboratory measurements it showed high temperature sensitivity where the potassium peak positions changed with the repetition of measurements, refer to **Error! Reference source not found.**. CsI(Na) had higher density compared to the common scintillator NaI(Tl) making it our best option for use as a scintillator crystal. Hence we replaced the BGO crystal with a CsI(Na) crystal.

Figure 3-9 Crystals which have been examined in the laboratory, left side. PMT used for laboratory measurements, right side.

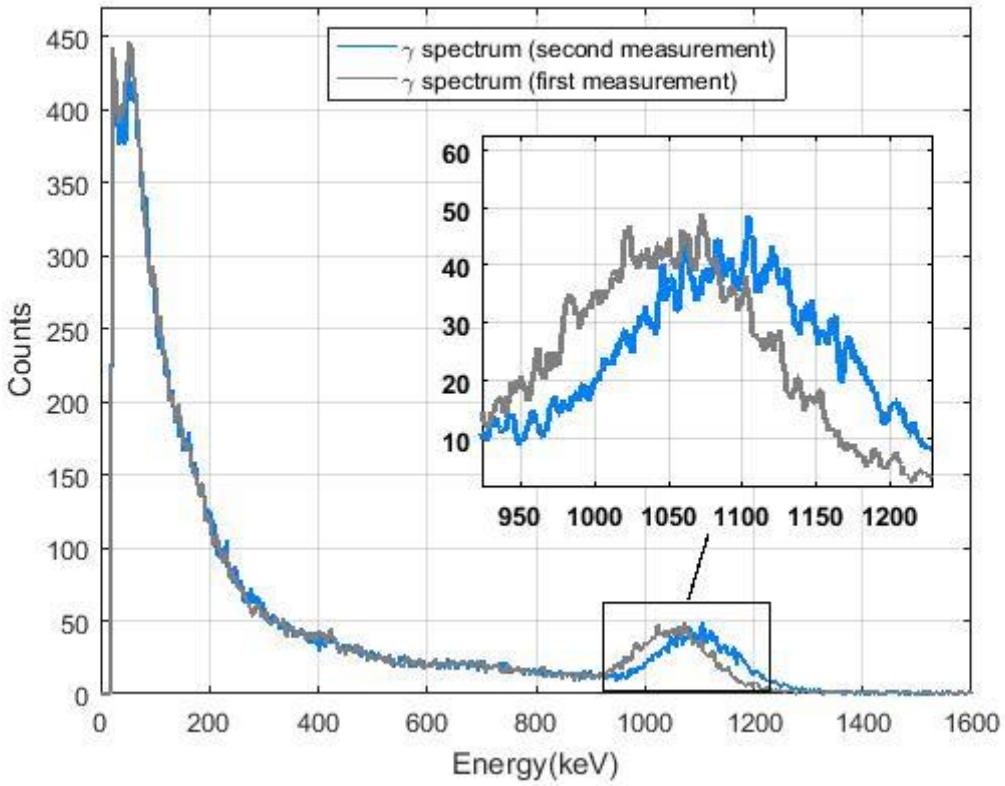

Figure 3-10 Repeating measurements with a BGO crystal in the detector, showing that the potassium peak has shifted noticeably.

3.3.3 Photomultiplier Tube (PMT)

A photomultiplier tube (PMT) is a vacuum tube that the converts input photons to output electronic signals by the photoelectric effect. The PMT consists of an input window, a photocathode, a focusing electrode, dynodes (electron multiplier) and an anode, refer Figure 2-11. Light detection is carried out through the following processes; a light enters through the input window, which then releases electrons from the closet photocathode by photoelectric effect. The photoelectrons are emitted into the vacuum and aligned by the focusing positive electrode onto the first dynode. The electrons are multiplied by the chain of dynodes with increasingly higher voltages which are collected by an anode the last dynode (Birks 1964). The PMT hence records the individual light flashes that are produced when a gamma ray photon interacts with the scintillator material, which are then amplified and counted as explained earlier. The photon count rate is a function of gamma ray flux through the crystal in addition to the detector size and efficiency (Crouthamel, Adams, and Dams 1970b). Another important factor for a crystal is called quantum efficiency (QE) and is related to

photocathode sensitivity. This factor is defined in the following equation (Knoll 2010), (noting that for an ideal photocathode QE would be 100%):

$$QE = \frac{number\ of\ photoelectrons\ emitted}{number\ of\ incident\ photons}. \qquad (3\text{-}1)$$

The PMT output signal, which consists of voltage pulses with different intensity, is fed to an Amptek Multichannel Analyser (AMPTEK 2016). The peak amplitude of these voltage pulses is in proportion to the energy of the gamma rays that scintillated in the crystal.

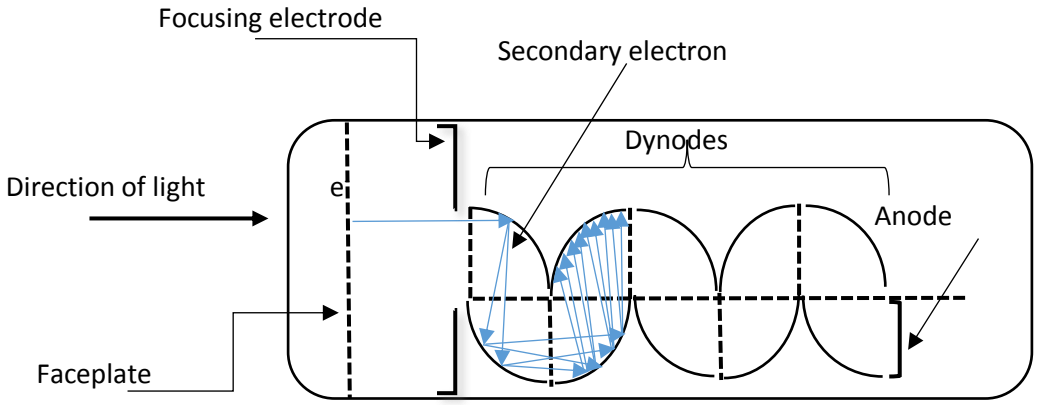

Figure 3-11 Schematic shape of PMT construction.

The PMT that we used in the laboratory was from the Hamamatsu, series H11432, with its specifications mentioned in

Table 3-5. To minimise optical loss a good coupling should be provided between the PMT and scintillator. For this purpose, silicone oil is used as a coupling material between the PMT and scintillator to provide good transmittance over the emission spectrum. Silicon grease has an index of refraction almost as much as a PMT faceplate, hence it provides good optical coupling (Hamamatsu 2007).

Parameters	H11432	unit
PMT Tube Size	38 (1-1/2)	mm
Photocathode Area Shape	round	
Photocathode Area Size	34 (diameter)	mm
Photocathode Material	bialkali	
Wavelength (Peak)	420	nm
Anode to Cathode Voltage	6	V

Table 3-5 List of PMT features for the PMT used in the laboratory (Hamamatsu 2017).

3.3.4 Multichannel Analyser (MCA)

The role of a Multichannel Analyser (MCA) is separating scintillation pules into different channels or bins based on their energies. The MCA is a pulse height analyser that measures the intensity of an incoming scintillation pulse peak and updates a histogram that is the pulse height spectrum. This histogram or pulse height spectrum is essentially a gamma-ray energy spectrum, but not calibrated to energy.

3.3.5 Description of the laboratory scale construction

Six laboratory scale boreholes (LSB) were fabricated in cylinder-shape containers with dimensions of 308 mm in radius and 210 mm in height. In the centre of each LSB, a plastic pipe (PVC) with an inner diameter of 55 mm, outer of 60 mm and 260 mm in height was inserted to accommodate a detector. The detector was a sensitive PMT coupled to a CsI(Na) scintillator crystal. The crystal was also cylindrical in dimensions of 35 mm diameter and 110 mm height, which was covered in an aluminium case of 41 mm diameter and 123.4 mm height.

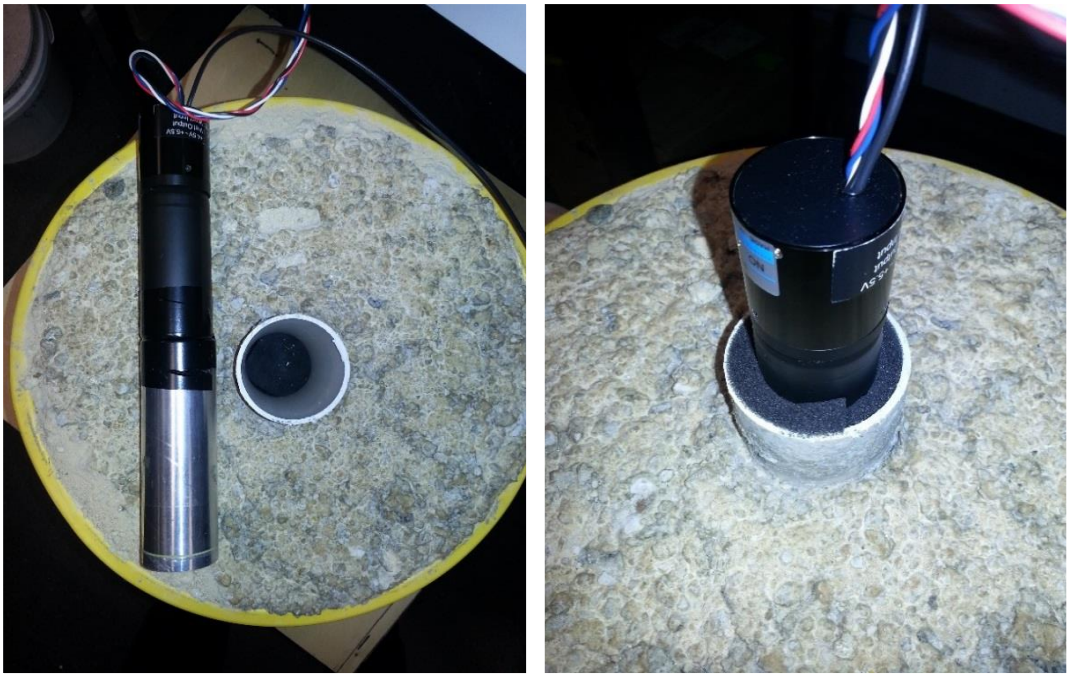

Figure 3-11 Photos of one of the LSB with the detector.

We placed the detector in the centre of the PVC tube shielding the top to eliminate the background light, refer to Figure 3-12. The LSB were filled with different materials to provide variation in atomic numbers (Z_{eff}). The same materials, which were applied in the simulations, were used in the laboratory experiments. A list of materials used with their concentrations is presented in

Table 3-6.

For increasing the natural radioactivity, we included potash or KCl in all of the LSBs. We measured natural gamma radiation spectra for each LSB. The amount of potash (7.5 Kg) may be high and does not seem realistic, but our focus is testing HMI technique. Thus high amount of potash potash in the experiments not only increase the spectrum quality also decreases the measuring time. In order to limit back ground radiations (gamma rays coming from the surrounding sources) measurements were taken at least 1 m away of any outer gamma-ray sources such as concrete walls or the floor. Moreover, high amount of potash in LSB makes signals strong enough that the background gamma rays cannot influence the results significantly.

Materials	B1	B2	B3	B4	B5	B6
Iron	…..	…..	1.25 Kg	4 Kg	2 Kg	15 Kg
Potash	7.5 Kg	…..	7.5 Kg	7.5 Kg	……	10 Kg
Sand	11.25 Kg	11.2 Kg	10.12 Kg	12.5 Kg	4 Kg	13.8 Kg
Kcl	……	4.8 Kg	…..	……	8 Kg	…….
Z_{eff}	12.34	14	15	16.8	18.5	20

Table 3-6 List of materials applied in LSB construction.

In order to verify the repeatability of the measurements the detector in each LSB was exposed 10 times and for a time length of 3 minutes each time. The statistical results from the measurement repetitions for one of the buckets was a standard deviation 0.027, standard error 0.006 and mean 1.75. For ten times measurements the error was 1.1% (error =standard deviation/Mean values), which was very low. Therefore, the confidence for the repeatability of the measurements was high. The histogram plot from the repetition measurements of the bucket is presented in

Figure 3-12 HMI for 10 measurements on the same LSB.

As discussed in previous chapters, the acquisition of quality gamma-ray spectra played an important role in our analyses. A high-quality spectrum provides better counting statistics, which according to the statistics of the Poisson distribution characteristics decreases the potential for statistical errors. The window time of 3-minute measurements provided us with a good quality spectrum at a modest 300000 total counts.

In Figure 3-13, we present four spectra measured in four different LSBs that have different Z_{eff}. To obtain suitable accuracy of the results the following procedures were applied:

- Gamma-ray spectrum calibration (energy calibration) for each measurement
- Selecting the optimum windows for the low and high energy section

Calculation of the ratio of the high to low energy windows (HMI calculation)

Figure 3-12 HMI for 10 measurements on the same LSB.

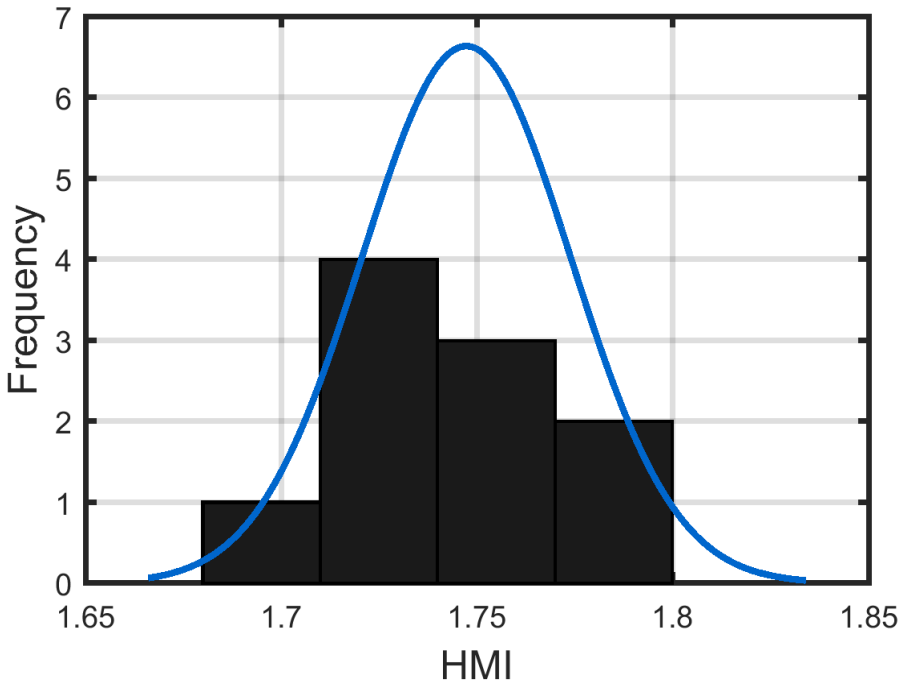

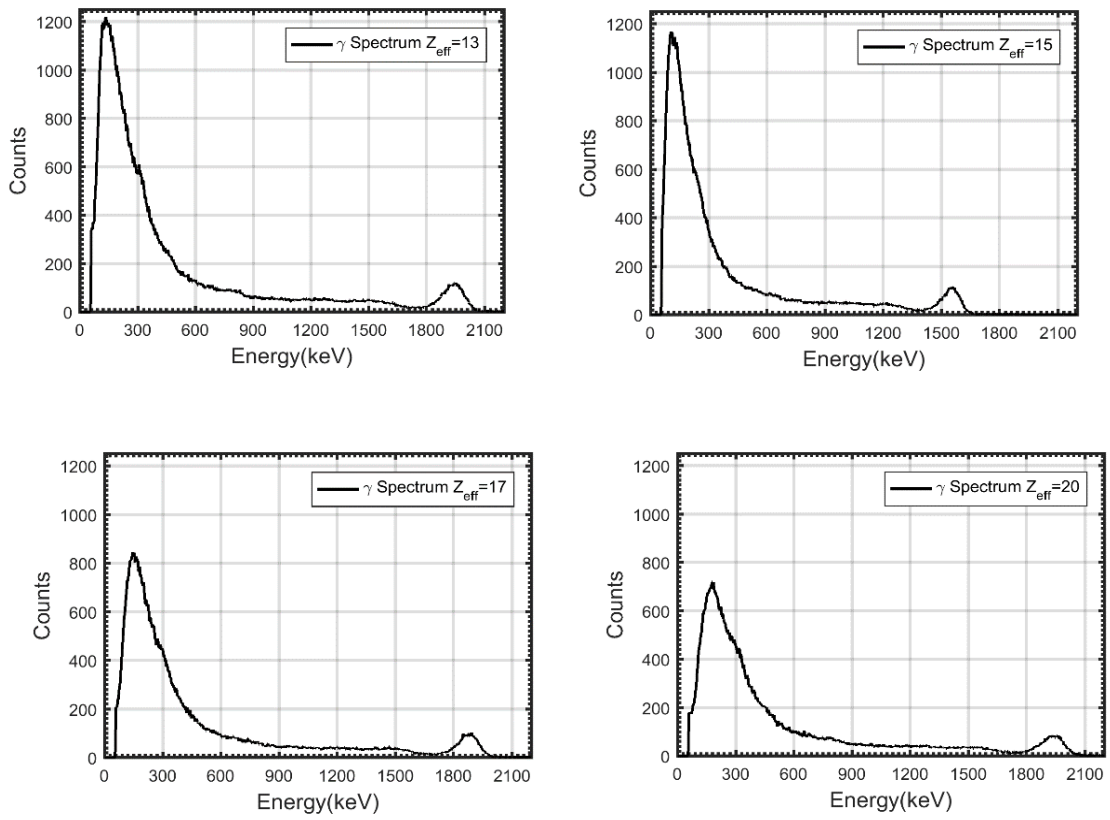

Figure 3-13 Spectrum measured from each LSB.

3.3.6 Gamma-ray spectrum calibration

As explained in the previous section, the initial output of the MCA is a histogram, which consists of the number of events in each pulse height channel. The channel numbers vary based on the system gains and voltages. Therefore, before further analysing, we converted channel numbers into energy channels. This calibration helped to draw an accurate comparison between the different spectra. In this procedure, the channel location of the known energy peak such as potassium is determined and fitted to the energy, which it deposited in the detector, 1460 keV in this case. Linear energy calibration can be applied on high resolution detectors as follows (Relly 1991):

$$E = mx + b, \qquad (3\text{-}2)$$

where E= energy deposited in detector, *m* is the slope, *x* is amplitude of output pulse and *b* is the energy intercept. Generally, for low resolution detectors the intercept value can be set to zero.

In order to determine the intercept value for high resolution detectors, it is possible to obtain more accurate calibration two known energy peaks are applied. Therefore the variable in equation is written as follows (Relly 1991):

$$m = \frac{(E_2 - E_1)}{(x_2 - x_1)}$$
$$b = \frac{(x_2 E_2 - x_1 E_1)}{(x_2 - x_1)} \qquad (3\text{-}3)$$

In Figure 3-14 gamma-ray spectra are shown before and after energy calibration. Since other peaks such as uranium or thorium cannot easily be detected, we only applied one peak calibration, which was a potassium peak. For this purpose, a window was defined around the potassium peak to determine the channel where the maximum value was located. In this case, the window was placed in the channels from 1780 to 1980. The maximum value in this interval, which corresponded to the potassium peak, was located at channel 1878. This channel was taken as energy of 1.46 MeV, energy of K^{40}, and the whole spectrum was resampled accordingly.

3.3.7 Window selection for HMI calculation

In Chapter 2, we discussed that the HMI technique is based on the ratio of two different parts of the spectrum, namely high over low energy regions. Hence, proper determination of these energy windows was essential. For this purpose, we normalised each spectrum so that the average value over the energy window, which was set between 250 keV to 500 keV would be the same. This window is a part of the Compton region of a spectrum that avoids most of the radioactive daughter isotopes. Potassium just identified with energy of 1.46 MeV, however uranium consisted of isotopes which release gamma-ray energies of 0.352 MeV, 0.609 MeV, 1.2 MeV, 1.76 MeV and 2.204 MeV when decaying. As for thorium, gamma rays emitted as part of the decay series with energies of 0.239 MeV, 0.583 MeV, 0.911 MeV

and 2.614 MeV (Minty 1992). Therefore, a window with energy ranges of 250 MeV to 500 MeV could avoid these isotopes.

Notice that the Compton region is highly affected by the density of the medium that gamma rays travel through while the low energy part of the spectrum is sensitive to both density and the atomic number (Z_{eff}). For this reason, normalising over the Compton region accounts for any density effects (Bertozzi 1981). We overlay all normalised experimental spectra to determine a point from which the spectra separate at lower energies (

Figure 3-15). From the literature we had expected that before 200 keV drastic changes would be observed as the atomic number varies and after this point all spectra overlay on the same line (Bertozzi 1981). This provided a guideline from which to choose our low energy window where it would only change according to the differences in atomic numbers. Thus, our two sets of windows were 0 to 200 keV for low energy and 250 to 500 keV for a high energy portion.

The last step was applying the selected windows to compute the HMI ratio. Errors for each calculation were also computed. In the following section, we present our experiment results with comparison to the simulated data.

3.3.8 Experimental results

Results from our experimental measurements in six LSBs and seven computer simulations are summarised in Figure 3-16. Since we repeat the measurements 10 times on each LSB, an averaged HMI ratio is considered. As we explained in previous chapters, the HMI ratio should increase with increasing atomic numbers. We can observe this increased trend on the experimental results and the synthetic ones. The relationship between the experimental HMI ratio with the atomic number is statistically significant R^2=0.96. In addition to this, because of good counting statistic in each measurement, errors are very small (1.2 %). The experimental results are noticeably close to those of the modelled response. A small shift is observed between the simulations and measurements. The offset between the two trend lines, may originate from the fact that we did not include the whole detector system in our models. For instance, we did not include the PMT and MCA system in our simulations, which on their own can affect the results.

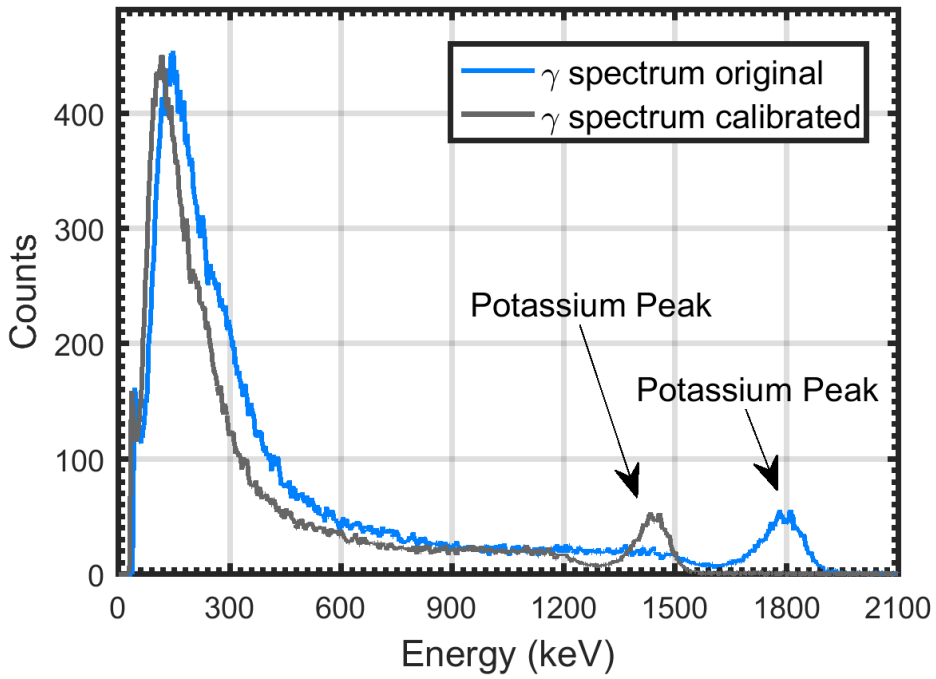

Figure 3-14 Gamma-ray spectrum from laboratory measurement. Blue spectrum is the original output of the MCA system. The potassium peak can be easily detected. We applied this peak to calibrate it to the energy channel, which when calibrated becomes the grey spectrum.

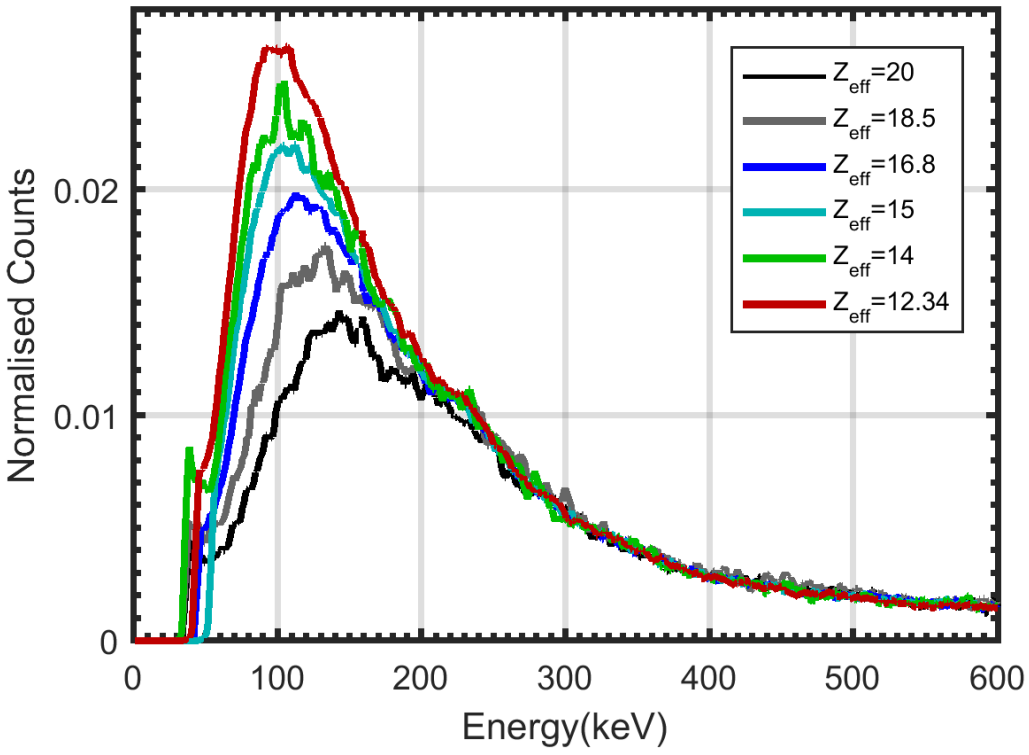

Figure 3-15 semi-logarithmic scale of gamma-ray spectra measured in different LSB. Smoothed experimental spectra, normalised over energy window 250 keV to 500 keV to eliminate for density variations. They are discriminated up to energy channel 200 keV where all spectra merge together (200 keV).

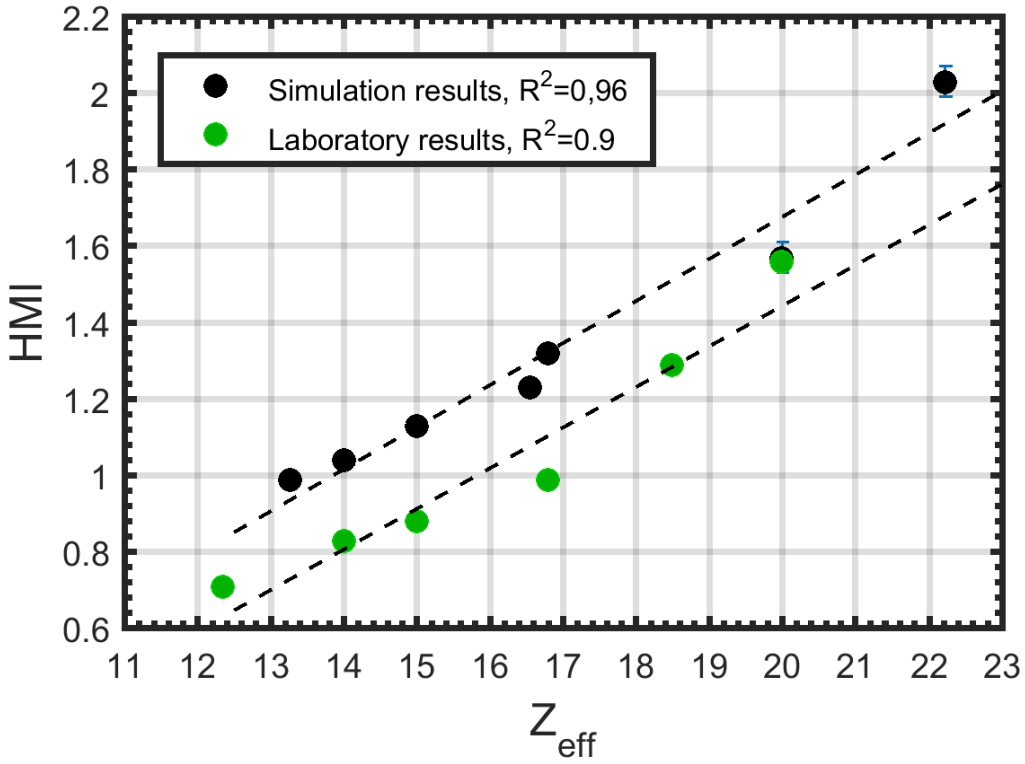

Figure 3-16 HMI ratio calculated from experiments (green symbols) and simulations spectra (black symbols) vs effective atomic numbers. There is a clear correlation between the HMI values and atomic numbers for both cases where trend lines from experimental and modelled data are just 3% different. The shift between the lines is a result of the detector's response, which was not included in our modelling.

CHAPTER 4. HEAVY ELEMENT LOGGING FROM NATURAL RADIOACTIVITY

Geophysical measurements of naturally occurring radioactivity are usually carried out in order to determine the elemental concentration of K, U and Th. These three radioactive elements are common radionuclides and are used indirectly as markers for either rock units or alteration patterns. In base metal and gold exploration, often the main natural gamma radioactive source of interest is potassium since sericitization tends to increase potassium, (Killeen 1997a). Another example is in sedimentary rocks where sandstone is distinguishable from shales because of its lower potassium content (Killeen et al. 1996). The other parts of the natural gamma-ray spectra have been neglected in mineral exploration, as the scattered radiation components do not have specific elemental traits. Since gamma scattering effects are strongly dependent on the atomic number of the originated medium, further information can be extracted from the gamma-ray spectrum related to the elemental compositions. Such additional information should enable a more informed interpretation of the surrounding rock formations.

The work described in Chapter 3 demonstrates that the gamma-ray spectrum can yield information about the concentration of heavy elements, such as iron and copper, within a rock. However, this is only feasible if the measured spectrum is of sufficient quality. The quality is determined, in terms of the number of gamma counts received principally in the low energy windows (50-150 keV, where photoelectric effects tend to dominate scattering) and in the higher energy windows (upwards from 500 keV to 1 MeV, where Compton scattering processes dominate); the precision is primarily determined by counting statistics. The longer time a tool is spent in recording a spectrum, the more gamma rays are collected in the spectrum thus counting statistics (which is a measure of spectrum quality) increases. Wireline logging typically moves the tool too quickly (more than 2 m/min) to allow good quality spectra to be recorded. Whereas, a logging-while-drilling tool, equipped with a 256-1024 channel gamma-ray spectrometer can potentially record data of sufficient quality as drilling speeds are much slower (0.1-0.3 m/min in diamond drilling) than logging with wireline. Such a tool, the Auto-shuttle, is under development within the DET CRC project 2.2 “Sensors for rapid rock characterisation” project. A prototype version of this was deployed at the Brukunga (former) pyrite mine in SA and has yielded encouraging results.

In this chapter, we report on the field trials where we simulated the Auto-shuttle measurements using a gamma-ray spectrum sonde and also conducted measurements applying a prototype Auto-shuttle. The study of natural gamma-ray spectra, which were collected with a standard commercial wireline gamma-ray sonde tool (using the standard logging speeds) in the Stavely Project in Victoria, is also analysed in this chapter. The aim of this study is to compare the quality of the spectrum measured from a commercial wireline sonde versus Auto-shuttle to highlight the importance of having sufficient counting statistics to produce reasonable spectrum quality in order to apply the HMI calculation.

4.1 BRUKUNGA DATASET

4.1.1 Site information

The Brukunga Drilling, Research & Training Facility, was established at the former Brukunga Mine site in the Adelaide Hills, South Australia. It is located 4 km north of Nairne, and 40 km east of Adelaide in the Mount Lofty Ranges of South Australia, refer to Figure 4-1. A number of boreholes have been drilled on the site providing, detailed petrophysical and geological information. The first hole, RD01, has had extensive wireline logging and elemental assay performed.

The rock formations in the area are a series of pyrite- and pyrrhotite-bearing greywackes and siltstones at the base of the Kanmantoo Group. On a small-scale, sulfide-rich bands are distributed parallel with the bedding (Skinner 1958). Iron-sulfide mineralisation occurs in 15-30 m thick lenses that are separated by waste beds approximately 6 m thick (LaGanza 1959). These lenses are psammitic to pelitic metasedimentary units which are intersected by dolerite dykes and can be alternated considerably (Kitzig, Kepic, and Kieu 2016).

The borehole used for this study, RD01, was drilled to a depth of 300 m at an angle of 60^{o} (perpendicular to the stratigraphy), refer to Figure 4-1. RD01 has been well studied with a variety of petrophysical logs having been acquired in 2012. A professional wireline service company conducted different log measurements such as magnetic susceptibility, density, self-potential, velocity, induced polarisation and natural gamma-ray logs. Moreover, geochemistry information from drill-core retrieved from RD01 is provided with 1 m spacing.

Therefore, the lithology and many properties of the rocks within the borehole are well defined. This borehole was particularly good in that we could relate elemental information to petrophysical information to evaluate the HMI technique. Hence, RD01 was a good candidate to carry out our testing.

4.1.2 Data collection

The natural gamma-ray spectra were collected with a customised wireline gamma spectrometer tool modified to simulate, a new logging-while-drilling (LWD) spectral gamma tool with performance similar to the Auto-shuttle. The Auto-shuttle is a new tool that provides continuous logging while diamond drilling. It has been designed to connect into the Bottom Hole Assembly (BHA) at the surface level prior to drilling. The Auto-shuttle is positioned above the core barrel and below the back-end assembly, which allows for the collection of data while drilling is performed (Figure 4-2). At the end of the core run, the Auto-shuttle is retrieved along with the rock core and the data are collected. Since diamond drilling is a relatively slow process, at 0.1-0.5 m per minute, this technology should provide high-quality natural gamma-ray spectrum over 1 minute intervals (Greenwood 2015). This new LWD spectral gamma Auto-shuttle may become commercially available over the next year (Hillis 2014); hence the customised wireline gamma spectrometer tool was able to be deployed in a manner to simulate the logging speeds that would occur during diamond drilling; approximately 5 minutes per half metre (0.1 m/min).

The sonde incorporated a Hamamatsu H11432 Photomultiplier Tube optically (PMT) coupled to a 35 mm diameter × 110 mm CsI(Na) encapsulated crystal. This crystal was chosen for its good resolution and relative stability of light output in the 25-40 degree Celsius range anticipated in the borehole. An amplifier buffered the PMT signal through 700 m of cable to a MCA analyser on the surface. Such an arrangement allowed us the flexibility of using a better MCA (which could not fit into a 45 mm space). The whole system was placed inside a stainless steel-tube case of 1.2 m height with 50 mm outer and 46 mm inner diameters. Our initial choice of crystal was a BGO, 38 mm in diameter and 50 mm long. Initially the BGO crystal seemed to be a reasonable candidate, since it has a high density of 7.1 g/cc (Hooshyari, Kepic, and Podolska 2015). However, because of its poor resolution and a strong negative temperature dependency on light output (Kepic et al. 2015) it was replaced by the CsI(Na) crystal. While CsI(Na) has a lower density of, 4.5 g/cc, it has a higher

resolution, 8.0% compared to 23.55% for the BGO. It was felt that the larger size allowed for more gamma rays to be captured (Kepic et al. 2015) overall and compensated somewhat for the poorer capture capability. Figure 4-3 shows a picture of the sonde on the ground, calibrating before measurements on the left hand side and applying it for our measurements in the borehole on the right hand side.

The spectral gamma-ray sonde was deployed in RD01 with a 700 m winch equipped with a calibrated depth counter. The winch cable used 4-core wire, which allowed for power to the detector system plus analogue data transmission to the surface MCA acquisition. Based on the known lithological and geochemical information the intervals selected for data collection was 60 m to 170 m. This range of depth contained a number of lithological contrasts that were expected to demonstrate the utility of using spectral gamma. Operational constraints restricted us to logging an average of 20 meters a day. This is the normal rate of drilling on a shift with diamond drilling, so it would have been unrealistic to log faster when simulating a logging-while–drilling technology. The whole interval was logged over 6 days. Once deployed to the relevant depth the acquisition was started as the tool was brought slowly up the hole. Simulating Auto-shuttle speed with the winch wireline system proved to be impractical due to being unable to control the winch at such low speeds; thus, we implemented a stop-start measurement approach to provide the same data resolution as the anticipated Auto-shuttle speeds. The sonde was moved into position to measure the natural spectral gamma rays at 50 centimetre depth intervals for 5 minutes between intervals to be consistent with the Auto-shuttle logging speed.

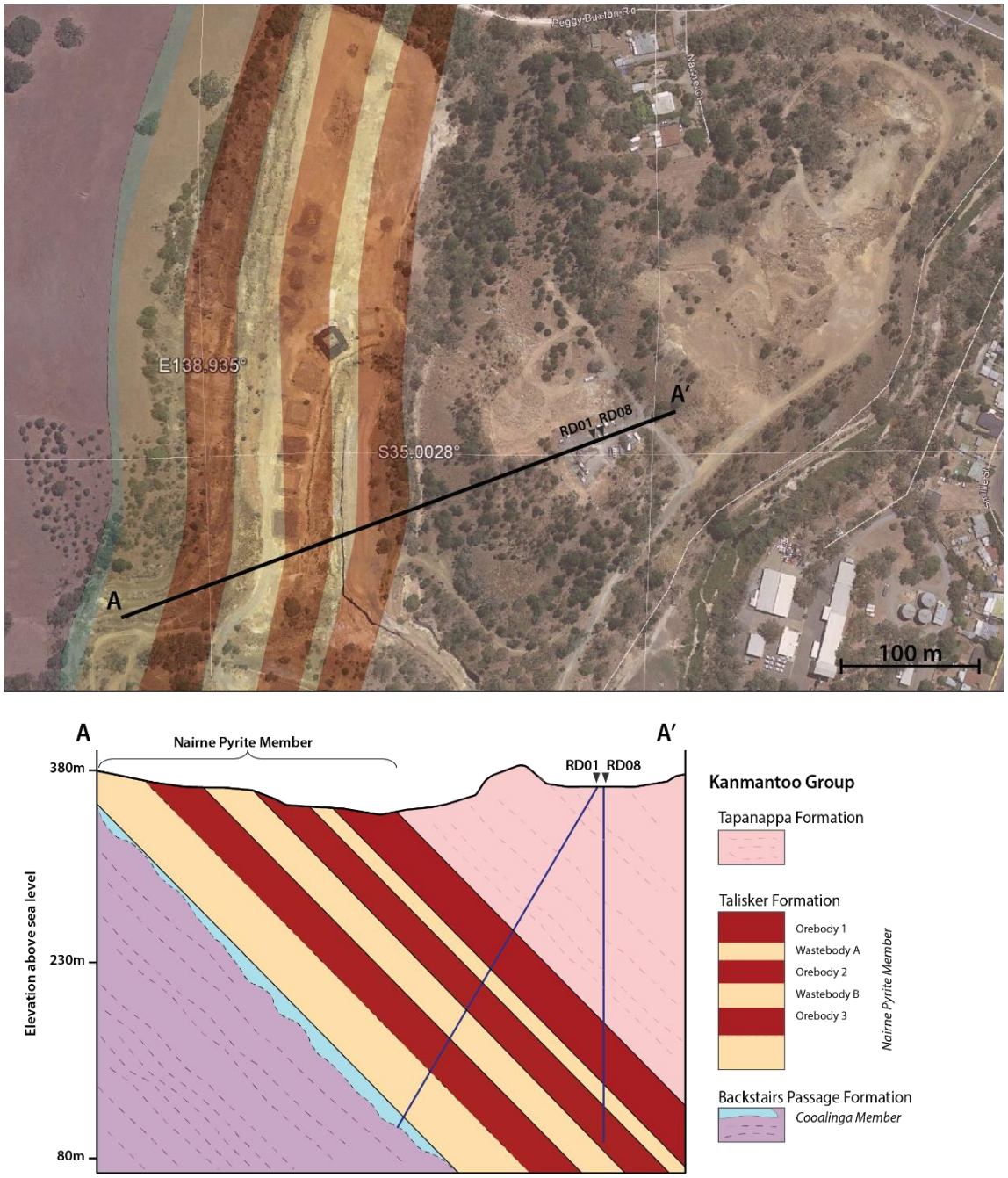

Figure 4-1 Location of Brukunga Drilling Research & Training Facility site on Google maps (2017). A simplified geological map and section of the Brukunga test site area shows a series of dipping pyrite layers interleaved with metasediments at depth. The intervals logged in our tests were in the upper Tapanappa formation, which is above the main pyrite belts, due to acid groundwater concerns. Preparation courtesy of C. Kitzig, orebody-waste classification after (George 1969).

Figure 4-2 An example of the Auto-shuttle being tested in another hole nearby (as this thesis was being written). The Auto-shuttle is located between the back-end-assembly on the left and the inner tube on the right. The operator in the photograph is downloading the raw data from the Auto-shuttle, which is then uploaded to a PC for processing.

.

Figure 4-3 Our spectral gamma sonde assembly lying on the ground (foreground left) and being deployed at Brukunga in hole RD01 (right).

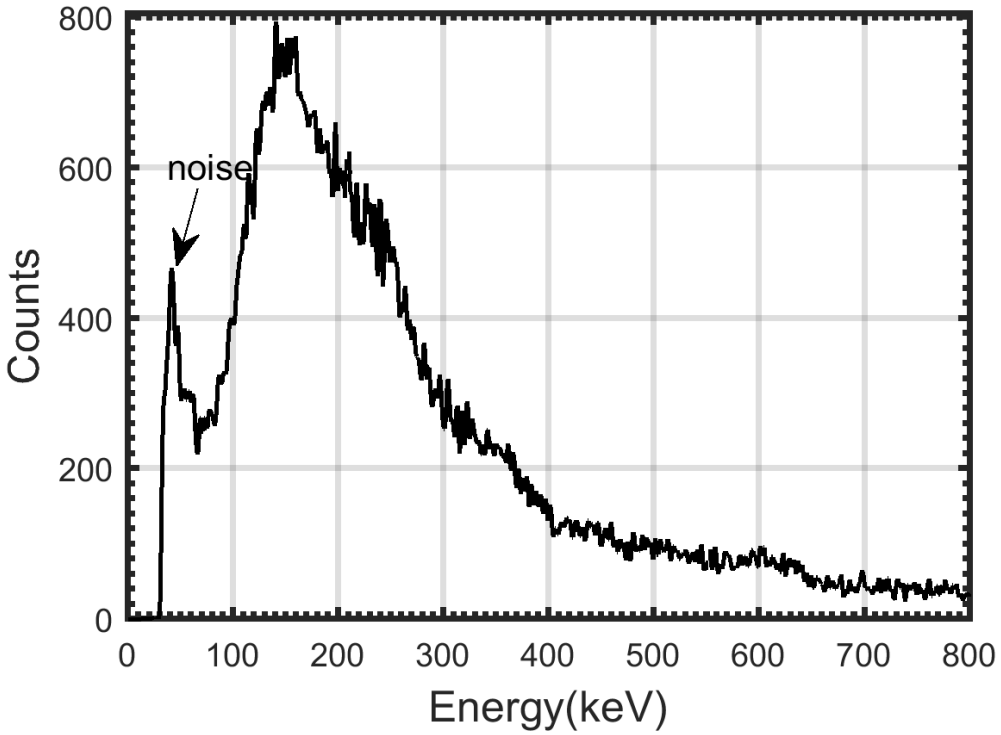

Figure 4-4 An example of gamma-ray spectrum acquired at depth 150 m from RD01. Typically only the spectrum above 60 keV are used in the spectral analysis.

During data collection, we encountered several issues that made later data processing difficult at times. Firstly, there was significant background noise on the winch analogue signal lines that originated from a nearby petrol generator. The noise mostly affected the low energy parts of the spectrum, less than 50 keV. Hence after further analysis (refer Figure 4-4), we cut the spectra from 0 to 40 keV. Losing this part of the spectrum did not significantly affect our HMI calculations as other parts of the spectrum, 50-150 keV had more gamma counts and were strongly affected by photoelectric effects. A couple of intervals had very low gamma counting rates (such as depth 143 m and 161 m) and these were more significantly affected by this particular electrical interference. Another notable issue was occasional systematic errors in the depth measurement. This was due to the slippage of the winch cable through the guide wheel that increments the depth-counter. In addition, removing the sonde at the end of each day then starting from the surface the following day meant that the log might not be continuous with depth. Repeat measurements at the start and the end of each day were performed to lessen this issue, but it was still difficult to correctly align the data from different days. To address this problem we matched the total count of the gamma rays (TC)

from our measurements with those from existing TC logs in RD01. WellCAD software provided the ability to match the depths from different logging measurements. For this purpose, one or two points at noticeable features were chosen from both logs to be used as the referencing points. By linking these points, the position of whole dataset was shifted accordingly to match the new depth (Figure 4-5).

4.1.3 Calibration and spectral analysis

The same calibration and analysis technique described in section 2.2.4 was applied to extract the HMI measure from the wireline spectra in RD01. Examination of the gamma spectra (shown in

Figure 4-6) shows that the spectra tended to merge at the 260 keV energy where Compton scattering dominated in determining the shape of the spectrum. Windows of 50 keV to 200 keV for the low-energies and 600 keV to 800 keV for the high-energies were used to calculate the HMI number. The interval 600-800 keV for the Compton region provided better results than 250-500 keV used in the calculations for the laboratory datasets. as 600 to 800 keV, avoided the gamma peaks from the daughter isotopes of radioactive sources while a similar number of gamma rays were registered (degrading the counting statistics).

As discussed in previous chapters (Section 2.3.4 and in detail in Chapter 3) HMI is a measure of Z_{eff} of the medium through which gamma rays are absorbed via the photoelectric effect. Mineralised zones should have higher Z_{eff} because the rock is made with higher atomic number elements, such as Fe, compared to the rest of the formation, which are comparatively richer in Al, K, and Mg. Therefore, Z_{eff} should follow the mineralising trend of the mineralised zones, which in this case is mainly pyrite (FeS_2). To evaluate this relationship Z_{eff} of RD01 was calculated using core assay geochemistry data from the borehole. These data are sampled in 1 m intervals and has less resolution compared to the natural gamma-ray spectral measurements, which were recorded in 50 cm intervals.

Figure 4-7 shows Z_{eff} vs Fe assay for RD01 with colour coding based on lithological information, host rock in orange, mineralised zone in purple, doleritic dykes in green, and shales in blue coloured symbols.

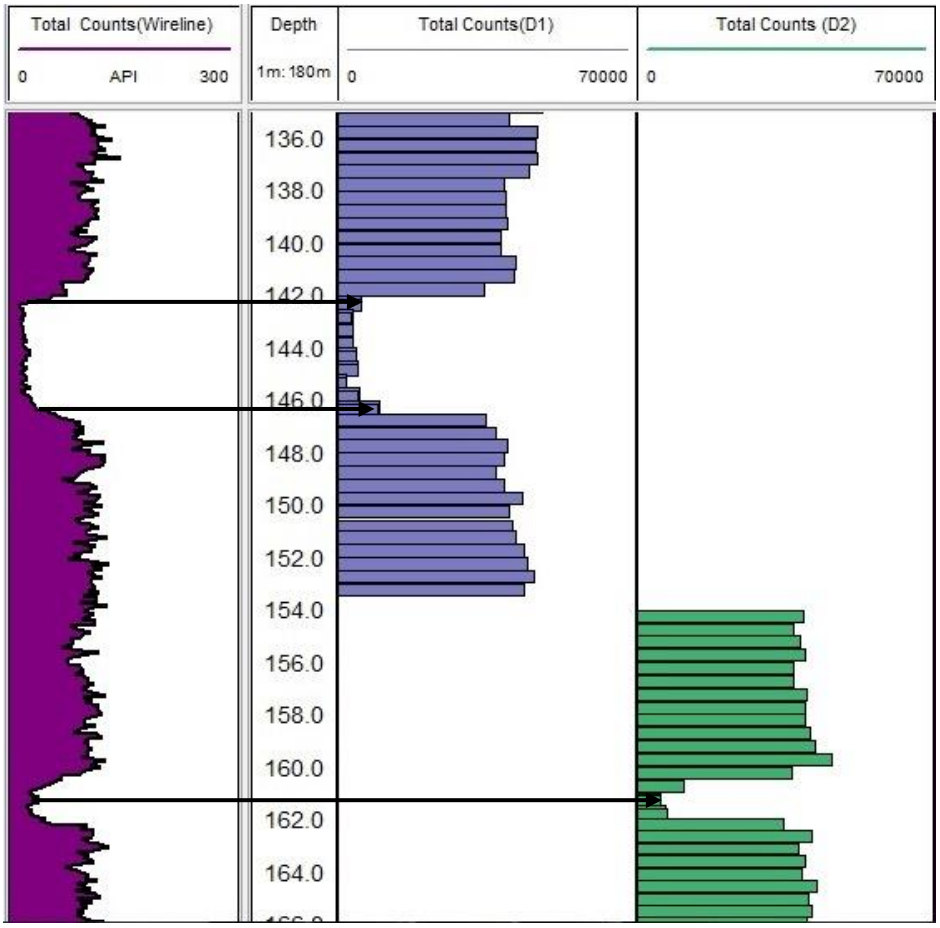

Figure 4-5 Depth matching with the aid of WellCAD software for RD01. The purple plot is the total gamma-ray data collected by a wireline company and the blue and green plots are the total gamma-ray counts from each spectrum, which were carried out on different days (two different colours in this example).

The correlation between Z_{eff} and Fe assay is very good with $R^2 = 0.96$, as iron rich minerals dominates the variations in Z_{eff}. Most of the Z_{eff} versus Fe data points, shown in

Figure 4-7, are clustered around the best-fit line except near the centre of the plot where the dolerite data is located. The principal reason for this shift from the otherwise trend line is due to the higher amounts of Cu in the dolerite. Cu also has a relatively high atomic number of 29 that influences the Z_{eff} number when it is abundant. Some prior knowledge of the local geology assists in deciding if the variation is a result of iron or other mineralisation.

Figure 4-8 shows HMI values calculated from the spectra measured with Auto-shuttle simulation in RD01 and plotted against Z_{eff}, The lithology of the formation has been categorised into the same four groups as in

Figure 4-7. The mineralised zone, in the purple symbols, is well distinguished from the host rock, in the yellow symbols. HMI targets Z_{eff} regardless of composition. However, the iron-rich minerals should be responsible for most of the observed changes in HMI that we derived from the spectra gamma data. Note that both Z_{eff} and HMI show two groupings of values.

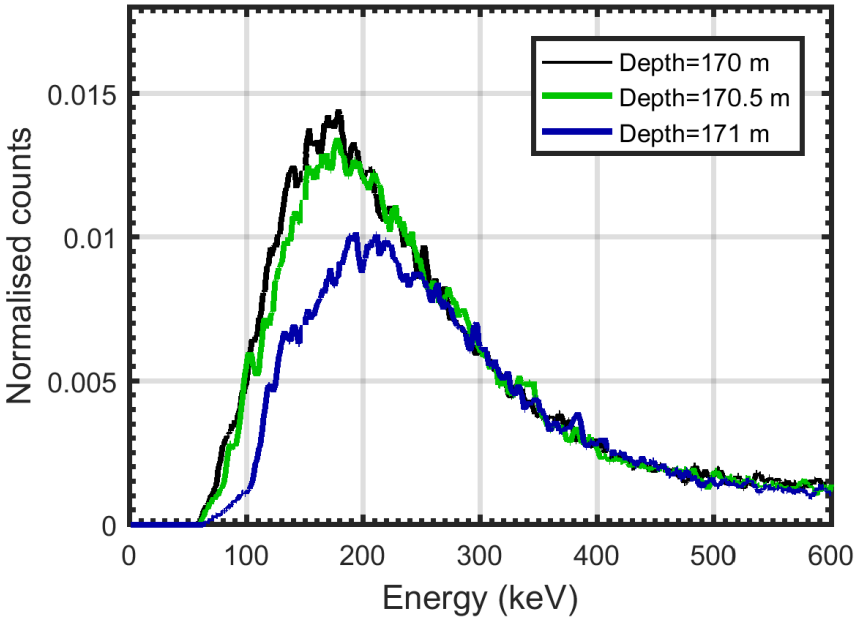

Figure 4-6 Overlaying spectra from 3 consecutive intervals.

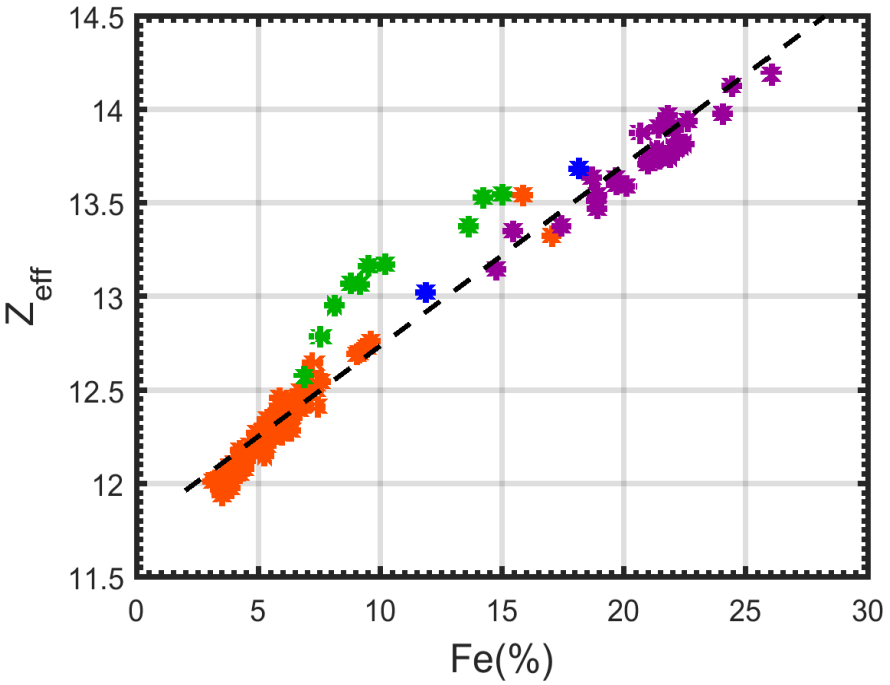

Figure 4-7 Z_{eff} vs Fe for RD01 borehole in Brukunga with colour coding based on lithological classification. The correlation between Z_{eff} and Fe assay is very good with $R^2 = 0.96$ Host rock in orange, mineralized zone in purple, doleritic dykes in green, and shales in blue coloured symbols.

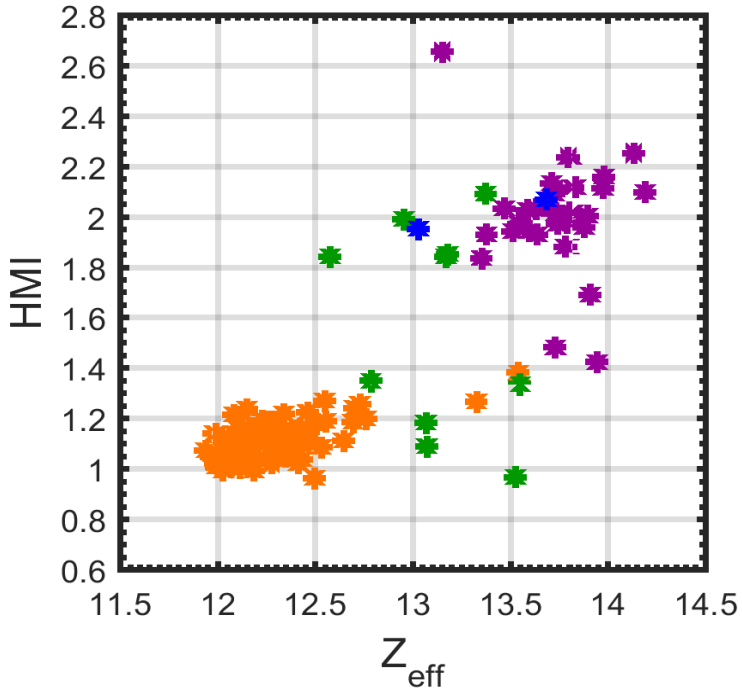

Figure 4-8 HMI calculated from gamma-ray spectrum measured in RD01 hole in Brukanga is cross plotted with Z_{eff}, calculated from the geochemistry assay data. It is colour coded based on lithology the same as the previous plot.

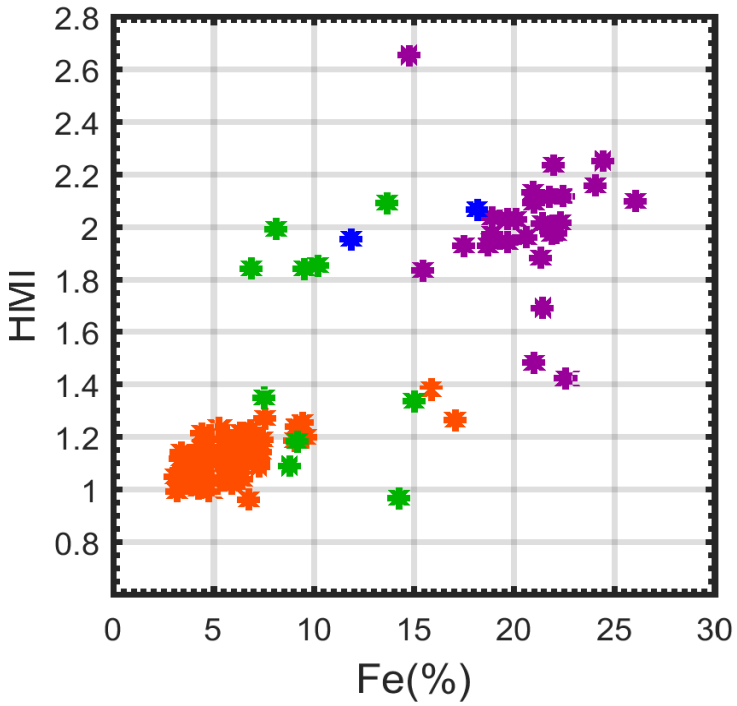

Figure 4-9 HMI values vs Fe assays collected in RD01borehole located at Brukunga site with lithology colour coded the same as the previous two plots. The mineralisation zone in the purple symbols can be separated from the host rock in the orange symbols. In the centre of the plot the green symbols, which correlated with doleritic dyke are spread. This is due to higher amounts of Cu in this section. Cu also has a relatively high atomic number of 29 that influences the Z_{eff} number when it is abundant.

The good correlation observed between Fe and Z_{eff}, see

Figure 4-7, suggests that we can replace Z_{eff} with Fe assay in Figure 4-8. So, HMI can follow variations in Fe. In Figure 4-9 HMI is cross-plotted with Fe for RD01 borehole at Brukunga with the same lithology colour coded used in the previous two plots. The mineralisation zone is separated from the based host rock. However, the doleritic, rocks do not match linearly with Fe content. Hence, it cannot differentiate zones where less concentration of Fe_2O_3 is accompanied with other heavy elements. Mineralised zones in Brukunga are a composition of iron (Fe) and sulphur (S), hence regions high in both elements correspond to mineralised zones.

To better illustrate the performance of HMI in tracking mineralisation we plotted it along with five other logs, Fe_2O_3, Cu, S assay logs, gamma-ray total counts and a lithology log as shown in

Figure 4-10. At depths, 67 m to 69 m we observe that HMI values increase corresponding with higher values in Fe_2O_3 and Cu, while the S assay does not increase. Thus, these increases in HMI values, which are not very significant, are unrelated to sulphide

mineralisation. Moreover, total gamma-ray counts decreases in this section. In the lithology log this structure is defined as a dolerite dyke, denoted with a green block in

Figure 4-10. Moving further down to a depth of 78 m, a similar feature, a narrow dolerite dyke plotted in green bar, is repeated. From depths 96 m to 104 m, HMI values increase significantly due to two pyrite/pyrrhotite mineralisation bands that correlate thus increasing the values of all assay logs (Fe_2O_3, Cu and S logs) and also gamma-ray total counts (TC). These mineralised zones are presented as purple blocks in

Figure 4-10. Pyrite –rich mineralisation starts again at depths of 134 m and continues to 170 m. However, the zones of disseminated to massive mineralisation are intersected by dolorite dykes and shale bands, coloured dark blue in

Figure 4-10. The shale zones correspond with low values for HMI, TC and Fe assay. The correlation between the HMI values and the mineralisation zones is strong enough that it may be possible to use jointly with TC data to aid in identifying different lithological structures in the Brukunga area.

Note that spectra quality matters for calculating HMI, in particular the number of gamma rays in the important energy windows. Gamma ray emission follows a Poisson distribution for a given concentration of radioisotopes where the variance increases with the average rate of gamma emission. Low gamma rates lead to poor counting statistics in a spectrum, which then increases errors, since the standard deviation for this model is approximately computed by $\sigma = \sqrt{x}$ where x is the number of counts in a single measurement. Therefore, the relative error is $Error = 1/\sqrt{x}$ (Bevington and Robinson 2003). On average the total number of gamma rays in each spectra across all energy levels is more than 43,000 counts collected at each station, which provides good counting statistics as the two HMI energy windows use between 5,000-10,000 gamma rays to compute the HMI figure. The standard error anticipated from counting statistics tends to be dominated by the high-energy window counts, and is of the order of 3 % relative to the HMI value (as it is a ratio relative errors are added). With such good counting statistics in the spectra measurements, why is the strong correlation between Z_{eff} and Fe seen in Figure 4-9 not reflected between HMI and Fe in Figure 4-9? It is mostly likely that the rock sampled by coring and later assay is not representative of the radius of influence associate with the gamma detector. Whereas, the assay derived from Z_{eff} and Fe content values will tend to be

self-consistent because both measurements are from the same sample. Also, poor depth registration in wireline versus core can also give the impression that the quantities are barely related if a number of transitions are mis-registered.

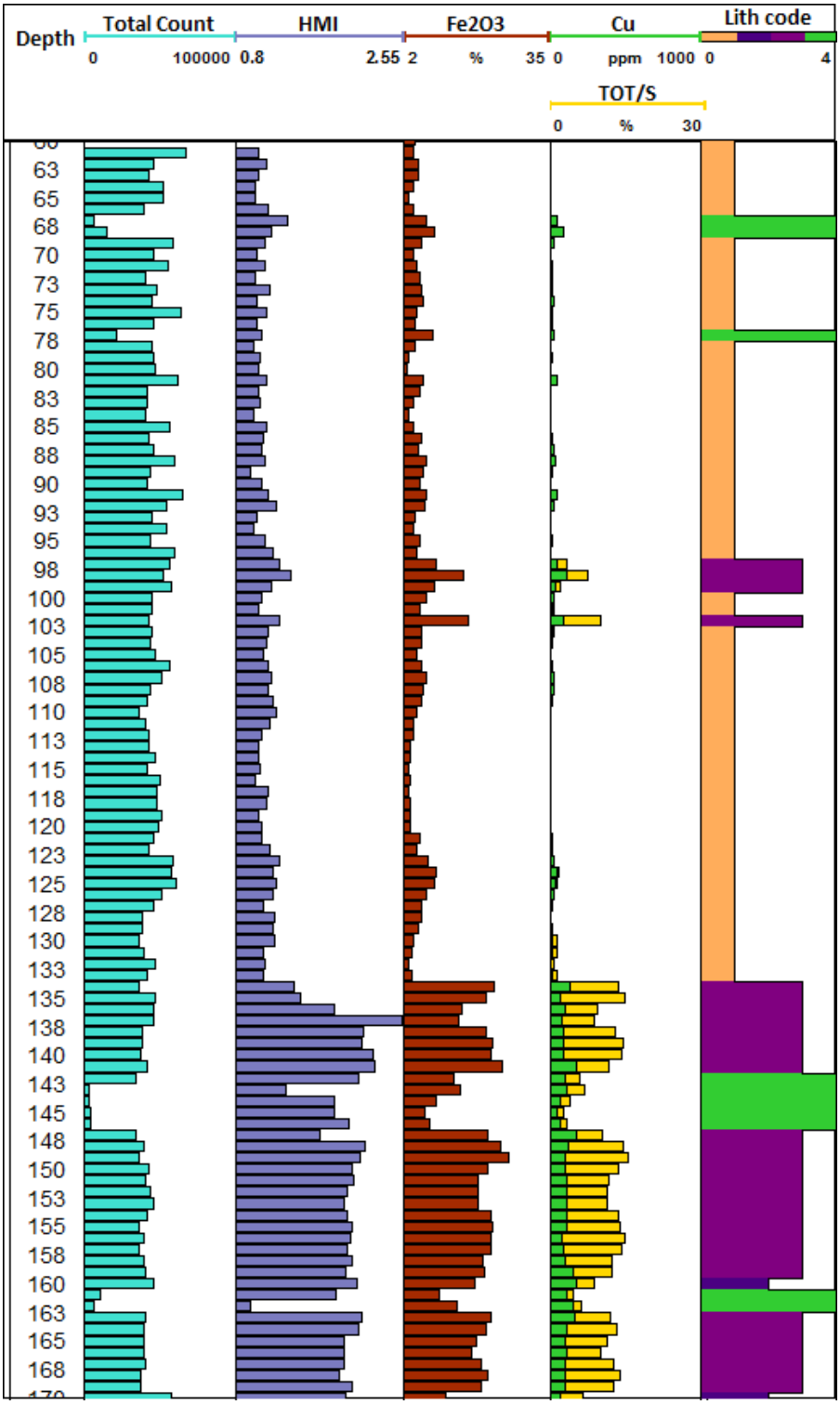

Figure 4-10 Total counts log, HMI, Fe, Cu (in green), S (in yellow), lithology logs vs depth for RD01borehole at the Brukunga site. From depths of 96 m to 104 m, HMI values increase significantly due to two pyrite/pyrrhotite mineralisation bands (in purple). Pyrite –rich mineralisation starts again at depths of 134 m and continues to 170 m which is well reflected on the HMI log by higher values (Hooshyari, Kepic, and Carson 2016).

4.2 USING COMMERCIAL WIRELINE TOOLS TO CALCULATE HMI

4.2.1 Can we use current wireline tools?

In the previous section, it was stated that a good gamma spectrum has many counts so that statistical fluctuations are minimised. Moreover, from the results of the computer simulations presented in Chapter 3, a good correlation between HMI and Fe content is observed from the high-quality spectrum. However, despite having quite high gamma counts in our field experiments the correlation between HMI and Fe content was not as high as the fluctuation errors might indicate, perhaps having steel case surrounding the detector could attenuate signal. That result is from the Auto-shuttle simulation performance, now the question is "will a wireline tool with only hundreds to thousands of gamma counts in the spectrum be good enough to be analysed using the HMI technique? We expect the answer to be" it is not good enough", however we tested this idea on commercially wireline spectral gamma data collected in a drilling program.

4.2.2 Site information

The Stavely Project was a collaboration between the DET CRC (supporting this research), the Geological Survey of Victoria and Geoscience Australia. The drilling and later logging campaign was conducted during 2014, the aim of which was to obtain a better understanding of sub-surface geology, and its (gold-base metal) mineral potential. The project area was located in southeast Australia, approximately 230-300 km west and northwest of Melbourne in western Victoria, refer Figure 4-11. The region consists of some belts, the Stavely Arc, and of poorly-exposed Cambrian volcanic and intrusive rocks that have the potential to host world-class magmatic-hydrothermal ore deposits (Crawford 1978). Around Mount Stavely and the Black Range, where the volcanic rocks are exposed, mineralisation related to porphyry Cu-Au and volcanic-hosted massive sulphide is known. However this area still has significant potential in terms of economic deposits which need to be discovered (Skladzien 2016). In all, fourteen drill holes were completed with a total length of 2708 m (Skladzien 2016). Geochemistry and geology information as well as comprehensive density, resistivity and spectral gamma wireline logs data were only provided for the Stavely-01 borehole (many holes collapsed before logging could commence). Therefore it was a good candidate for our study and an evaluation of the results of gamma-ray spectrum analysis.

Table 4-1 shows the drill collar information for Stavely 01.

4.2.3 Data acquisition

Spectral gamma-ray data was collected from a sonde deployed on a wireline. The spectral gamma tool used for these measurements is a QL-40 SGR from Mount Sopris Instruments. This tool is equipped with a BGO scintillation crystal with dimensions of 2.22 cm × 10.16 cm. The tool provides a 256-channel energy spectrum plus total counts. It can measure up to 3MeV in open or cased boreholes (Mount Sopris Instruments 2017). Measurements were taken at notional 1 cm intervals (interpolated and resampled in the acquisition software) and were mapped into 300 energy channels, each channel having an energy width of 10 keV. Logging was carried out at typical logging speeds between 3 and 4 m/s (Theys 1999), much faster than the Auto-shuttle which has an operational (drilling) speed of typically 10 to 20 cm/min. Geochemistry data was used to calculate Z_{eff} in order to compare with that determined from the HMI from the natural spectra recorded with the sonde. Geochemistry data was collected with the recently developed Lab-at-Rig^{TM}, which provides on-site geochemical and mineralogical information using portable X-ray fluorescence (XRF). Lab-at-Rig^{TM} is a new technology that analyses the powders produced during diamond drilling a proxy for a representative sample. The powders are collected at the collar and separated from the drilling fluids (Uvarova 2013). A small sample is enough for XRF analysis. Portable XRF (PXRF) analyses were applied on powder material using Olympus X-5000 and Olympus Delta Premium instruments (Uvarova 2013).

Hole ID	Drilling type	Latitude (GDA94)	Longitude (GDA94)	Total depth (m)	Basement lithology (generalised)
STAVELY01	Diamond	-38.018	142.878	249.5	Amphibolite

Table 4-1 Drill hole collar information (Skladzien 2016).

Figure 4-11 The location of Stavely project area in Victoria state, Australia (Skladzien 2016)

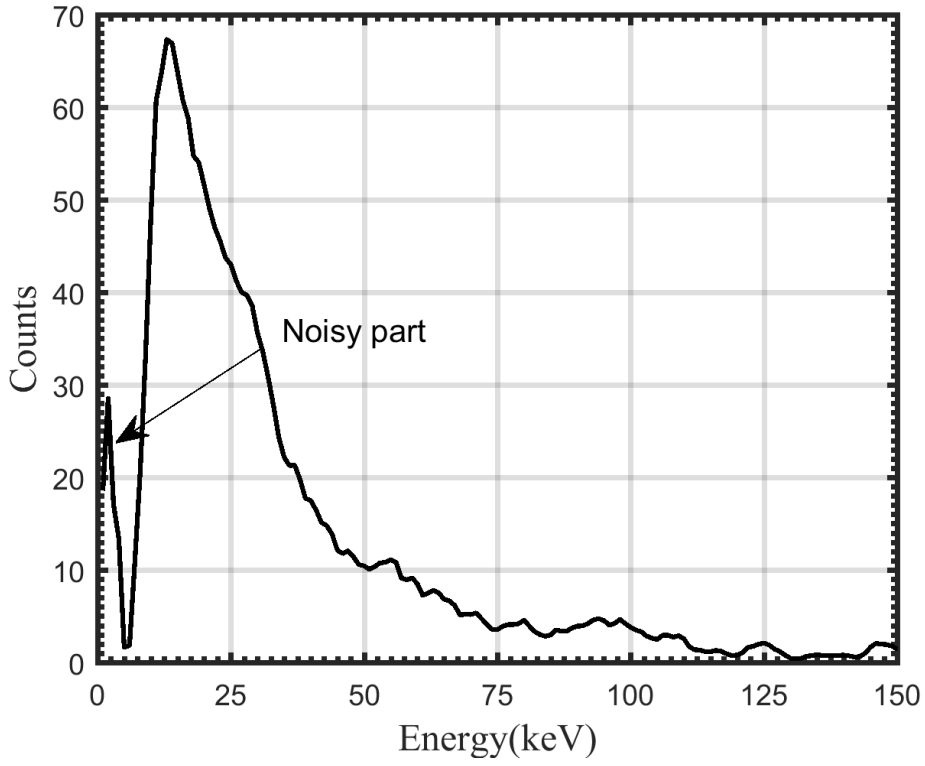

Figure 4-12 A spectrum from Stavely01, the first three channels are very noisy.

4.2.4 Calibration and spectrum analysis

A preliminary look at the data (Figure 4-12) shows that the first three channels are dominated by noise (likely electronic). The contamination of the very low energy part of a spectrum is very common with these tools (because they are not used in later analysis in standard radio-isotope identification). It is not an issue for HMI analysis since the energy windows chosen for HMI calculation also avoid this part of the spectrum. In order to improve the counting statistics of the recorded spectra, the data were summed/accumulated over 50 cm intervals and HMI was calculated for each interval. Figure 4-13 shows HMI as a function of depth along with total count gamma (TC), Z_{eff} and lithology for Stavely 01. Unlike the data recorded in RD01, we did not observe any strong correlation between HMI, Z_{eff} or lithology.

To investigate the lack of correlation between HMI and Z_{eff}, the data from Stavely 01 was considered in two distinct sections, see Figure 4-13 and

Figure 4-14 respectively. The first section contains contrasting lithological units that are reflected in changes in the Z_{eff} log over this section. The relative variation of Z_{eff} (σ/Avg(Z_{eff})), is 5.3% whilst for HMI it is 4.7 %. The second section, where the lithology is uniform, has only a 1.4% fractional variation in Z_{eff}; whereas the variation in HMI is comparable (about 5%) to its value in the 1st section (

Table 4-2). Thus, it appears the variance of HMI is largely independent of geology for these small changes in Z_{eff}. The reason for this lack of correlation seems to originate from the poor counting statistics in the spectra collected from Stavely 01. This is difficult to calculate from the raw data (LAS files) provided by the logging contractor as the data has been significantly normalised and interpolated to API equivalent rates, which is normal practice apparently. Thus, it is difficult to know whether there really are enough gamma rays to describe the Z_{eff} of the geology. The lack of change in variance between uniform and changing geology seems to indicate strongly that there are insufficient counts to keep counting errors down.

4.3 HMI FROM AUTO-SHUTTLE TESTS AT BRUKUNGA

As mentioned in the previous section, the Auto-shuttle is a new tool, developed in the Deep Exploration Technology CRC (DETCRC) that measures natural gamma-ray spectrum

during drilling a borehole (Figure 4-2). Unfortunately, spectral gamma measurement with Auto-shuttle technology over many tens of metres was not available during the writing phase of this thesis. However, some data from sporadic Auto-shuttle tests during the drilling of another borehole, RD08, in the Brukunga research site, acquired in the later writing phase, will be briefly analysed (refer to Figure 4-1 for the location). The Auto-shuttle was set to log gamma spectrum rays at 50-second intervals.

	Depth From	**Depth To**	**Ave**	**SD**	**SD/Ave (%)**
Z_{eff} (Sec 1)	30	66	14.22	0.75	5.27
HMI(Sec1)	30	66	0.64	0.03	4.68
Z_{eff} (Sec 2)	2	12	14.83	0.21	1.42
HMI(Sec2)	2	12	0.73	0.04	5.44

Table 4-2 Statistical information for both sections of borehole Stavely 01.

A gamma-ray spectrum from RD08 is shown in Figure 4-15. There is some electrical noise in the spectrum at energy channels less than 40 keV, which is below any region of interest. The most important feature of the spectrum is the quality: for each spectrum measured over 50 seconds an average of 30,000 total counts are recorded and distributed into 1024 channels. As discussed in section 3.2.4, the minimum number of gamma rays needed for a high-quality spectrum is considered more than 20,000 counts as a general rule of thumb to compute HMI and radionuclide concentrations. Auto-shuttle technology does appear to provide the high-quality natural gamma-ray spectrum anticipated for useful HMI calculation. Based on the time spent on the drilling and the length of core drilled over a 50 second time-span a gamma-ray spectrum is measured every 25 cm.

From a small interval measured with an Auto-shuttle tool, 220 m to 245 m, we calculated HMI from the collected gamma-ray spectrum and plotted these with the Fe_2O_3, Cu and S log calculated from assay data. The lithology log is also presented for this interval, on

Figure 4-17. The same lithology legend applied for RD01 is used for RD08. Z_{eff} calculated for this interval, from the assay data, is well correlated with Fe_2O_3 (Figure 4-16) with correlation of 96%.

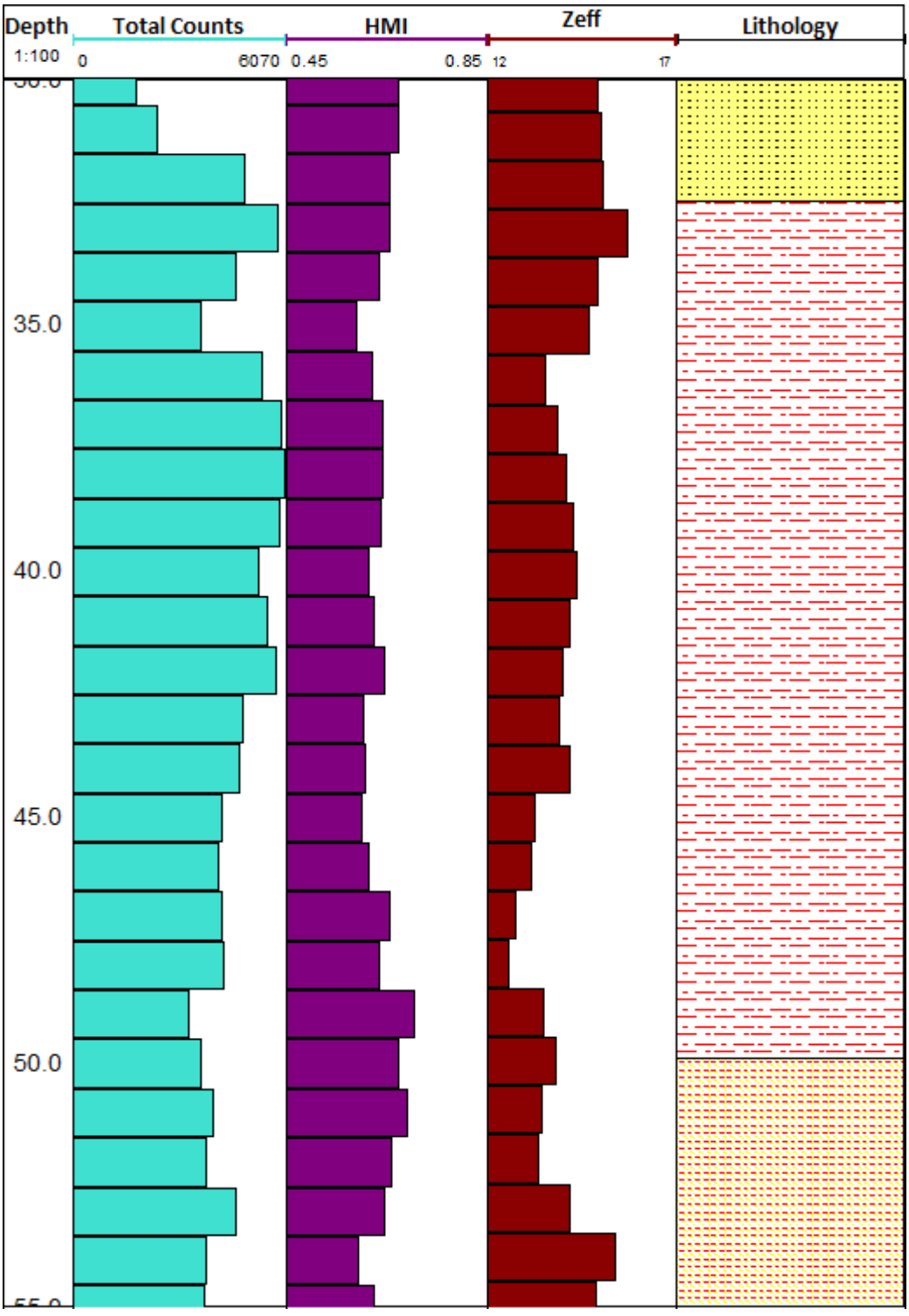

Figure 4-13 A section from borehole Stavely-01 where the lithology and Z_{eff} varies in three places (but not sharply as the lithology log implies). However, the computed HMI log does not change where anticipated.

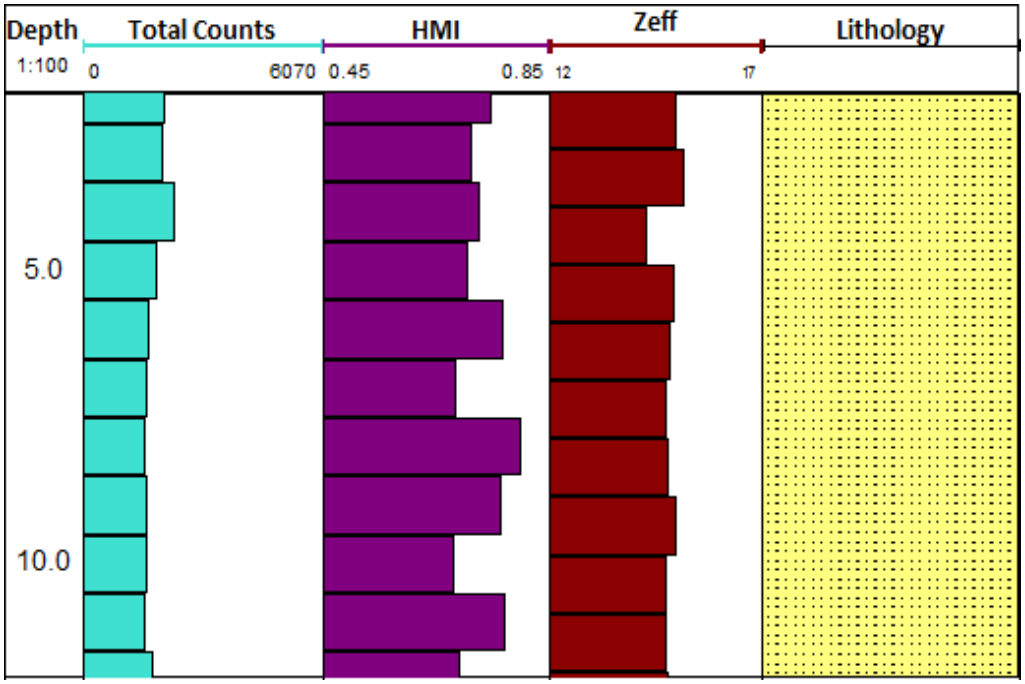

Figure 4-14 A section of TC, HMI, Z_{eff} and lithology logs for Stavely 01 where little change in response is expected as it is fairly uniform by all measures.

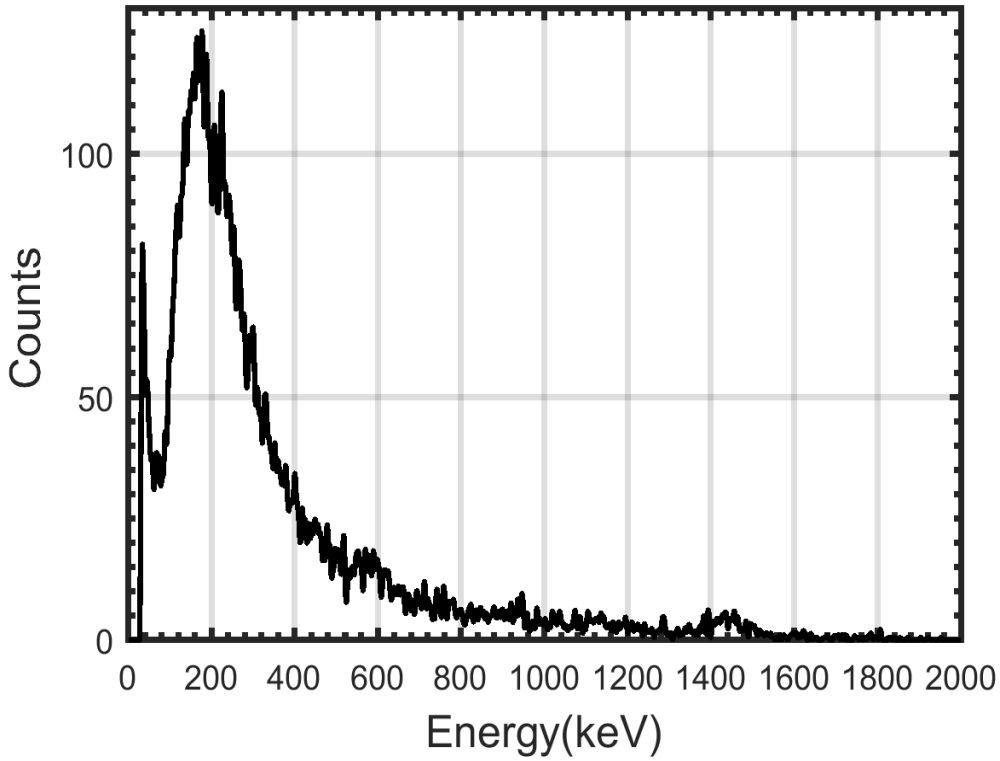

Figure 4-15 A spectrum measured in RD08 borehole at Brukunga research site using an Auto-shuttle tool. Natural gamma-ray spectra measured while drilling for one interval of 50 seconds. X-axis is energy channels where the potassium peak is easily discernible at around 1450 Kev (note that energy calibration was done on this spectrum)

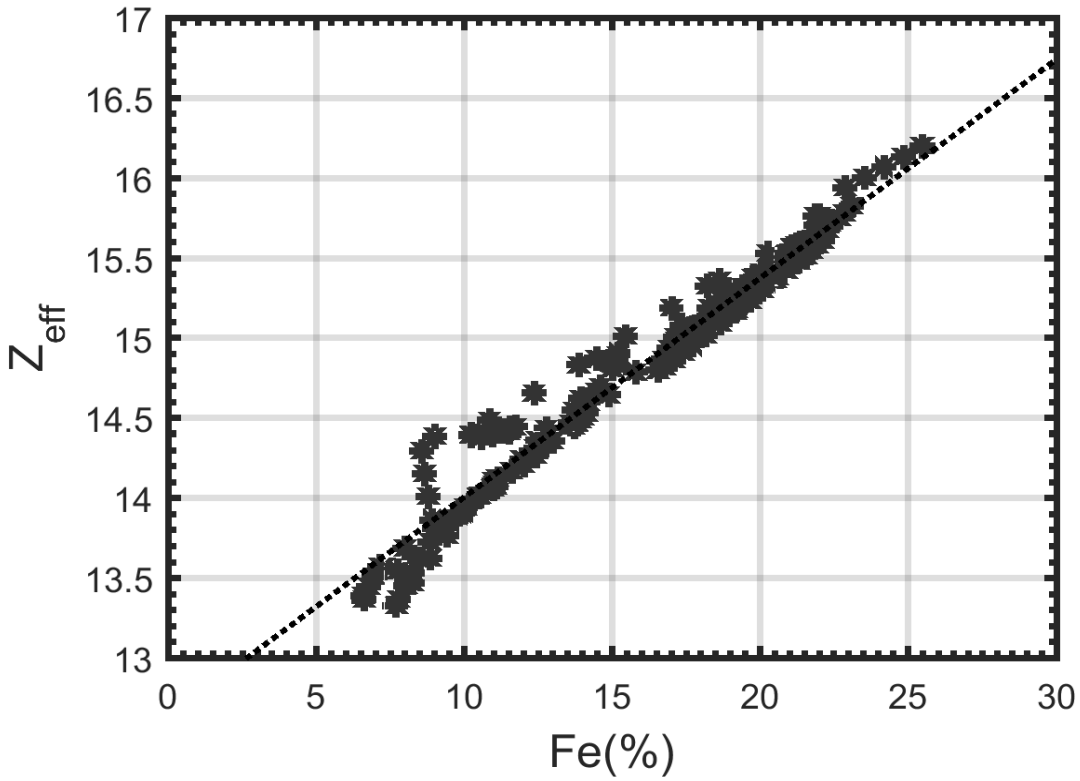

Figure 4-16 Z_{eff} is crossed plotted with Fe assay for RD08 hole in the Brukanga research site. A good correlation of R^2=0.96 shows that Fe has highly dominated variations in Z_{eff}. Hence for our studies it can be applied as a substitution for Z_{eff}.

From depths, 222 m to 228 m HMI values increase corresponding with an increase in Fe_2O_3 and S assay values, however the Cu assay does not change significantly. Thus, this increase would be related to the pyrite band (purple). Further down from depth 229 m to 240 m, the HMI values increase with significant increase in Fe_2O_3, S and Cu assay logs suggesting the mineralisation zone and the pyrite/pyrrhotite band. This band is intersected with a dolerite dyke, denoted in the green block, and is registered with low gamma-ray total counts (TC), refer to

Figure 4-17. From depth 240 to 244 m, the HMI values increase following with higher values in the S and Fe_2O_3 assay logs, reflecting a pyrite band where the Cu assay is insignificant. Moving towards the bottom of the logs, the Cu assay values increase due to mineralisation; this is well reflected in the HMI log, by increasing the values significantly. In summary the HMI log is influenced by all heavy elements. In the mineralisation zones with high S assay values there are higher values of many heavier metallic elements; thus, it provides a stronger correlation with HMI values. The gamma-ray data collected from the (LWD) Auto-shuttle when analysed with the HMI method can aid in identifying variations in the Z_{eff}.

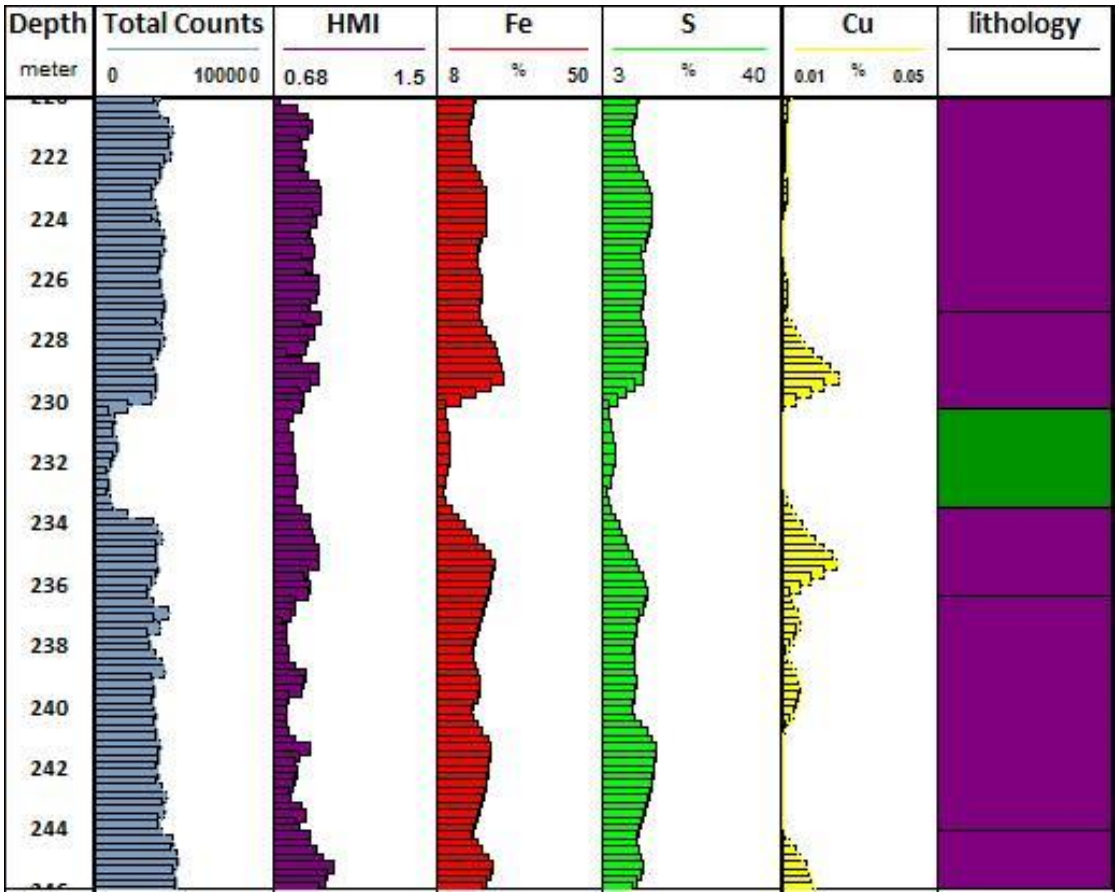

Figure 4-17 Total counts log, HMI, Fe, S, Cu assay and lithology logs vs depth for RD08 borehole at the Brukunga site, from depths 220 m to 245 m. HMI values increase significantly due to pyrite/pyrrhotite bands of mineralisation and Cu at the bottom of the hole and the dolorite dyke interbedded in the mineralisation zone can be detected by a reduction in HMI values in addition to gamma ray counts.

4.4 SUMMARY

Three natural spectral gamma-ray datasets have been used to evaluate the HMI technique in targeting the variation in the elemental composition of surrounding formations. Datasets have been collected with different measuring technologies. Firstly, data was analyzed from RD01 at the Brukunga mining site collected in a manner so as to simulate the Auto-shuttle LWD technology concept. The data from RD01 provided a high-quality spectrum that is essential for HMI computation. The HMI calculated from this dataset followed variations in elemental compositions (Z_{eff}) and Fe assay in the mineralised zones. This result confirms the expectation arising from simulation and laboratory tests. The second

dataset was acquired with conventional wireline logging technology. In this method the spectral gamma rays were measured while pulling up a probe, at a speed of 3-4 m/s, this resulted in low quality spectra with poor counting statistics. Hence, the HMI technique cannot be implemented reliably with wireline logging collected at such fast logging rates. The comparison between the natural gamma rays results from Stavely-01 and the RD01 and RD08 Brukunga datasets emphases the role of the future Auto-shuttle logging technology in providing high-quality spectra to apply calculations such as the HMI.

.

CHAPTER 5. HMI ANALYSIS OF SPECTRAL GAMMA-GAMMA DATA

The data presented in this chapter were kindly made available by BHP Billiton. Specifically, the data were gathered from the wireline logs of two drill-holes from iron ore deposits in the Pilbara. In each borehole two series of gamma-ray logs were carried out using two different tools. The first borehole was logged using a litho-density tool equipped with a Co^{60} source, which recorded the scattered gamma rays in the form of a spectrum. The second log was measured with a spectral gamma-ray tool, which does not employ a radioactive source but rather records the naturally occurring radioactivity of the formation. There are two main reasons, which make these datasets suitable for this study. First, data is collected in iron ore bearing formations, which provide a better opportunity to examine the ability of the HMI technique to track bands of iron ore deposits. Second, we can also compare the data from these two tools.

In the following, first we present the HMI calculated form spectra recorded with the litho-density tool and compare HMI values with iron assays to evaluate the correlation with iron. In the following section HMI is calculated and compared with iron assay using data from the natural gamma-ray spectral tool. We also compare the iron assay correlations with HMI values for both tools. This comparison allows us to determine which data acquisition approach results in better HMI and iron assay correlation. Finally information provided from the HMI and the total counts of the gamma logs (from both tools) have been used to describe the lithology log.

5.1 DATASET FROM LITHO-DENSITY TOOL

The gamma-ray logging was carried out by Surtron Technologies using a prototype litho-density (id code 7301), supplied by Century Wireline Services. This tool uses a 2 GBq Co^{60} radioactive source to irradiate the formation. It also includes a 5 mCi Cs^{137} source located next to the short-spaced gamma-ray detector in order to stabilise the gain. As with all litho-density tools it consists of both a long and short spaced detector. Both detectors are large CsI crystals with dimensions of 3.81 cm radius and 30.48 cm in length. The gamma-ray spectra are recorded in 256 channels and for depth increments of 1 cm. The boreholes were

logged with the common speed for wireline practise which is 3-4 m/min. More information about this tool is summarised in Table 5-1.

The provided dataset was not in raw format and the logging company applied some calibrations and processing prior to our analysis. For example, some negative values were found in the data, which might be the result of some initial settings and processing such as tool calibration and background noise removal. Unfortunately, the logging contractor did not provide sufficient information related to the pre-acquisition settings. To overcome problems related to negative values in the data, all negative values were set to zero prior to analysis. An example spectrum from borehole 01 (BH01) is plotted in Figure 5-1. Important peaks such as Co^{60} Compton edge, Cs^{137} peak and Cs^{137} back scatter can be identified. At the end of the spectrum the Compton edge of Co^{60} is observed at around channel 220 (Rapach 2008). The Cs^{137} peak is also present at channel 165 with its back scatter peak at channel 50 (Rapach 2008). This initial spectral analysis can help to define proper energy windows in order to calculate HMI. As explained in previous chapters (section 4.1.3), in order to obtain the best results, the HMI was calculated using different window ranges and compared to the iron assay data. The first sets of windows selected are from channels 10 to 45 for the low energy part (photoelectric region) and from energy channels 50 to 170 for the high energy window (Compton region). Note that HMI values are unit less, whether the studied spectrum is plotted vs channel numbers or energy does not affect the results. Hence there is no need to always convert channels to energies.

7301 litho-density tool	
Length	167 cm
Temperature	65 ^{o}C
Diameter	60.96 mm
Pressure	232 kg/cm^2
Weight	16.82 kg
Voltage required	60 VDC

Table 5-1 Litho-density tool characteristics from Century Wireline Services.

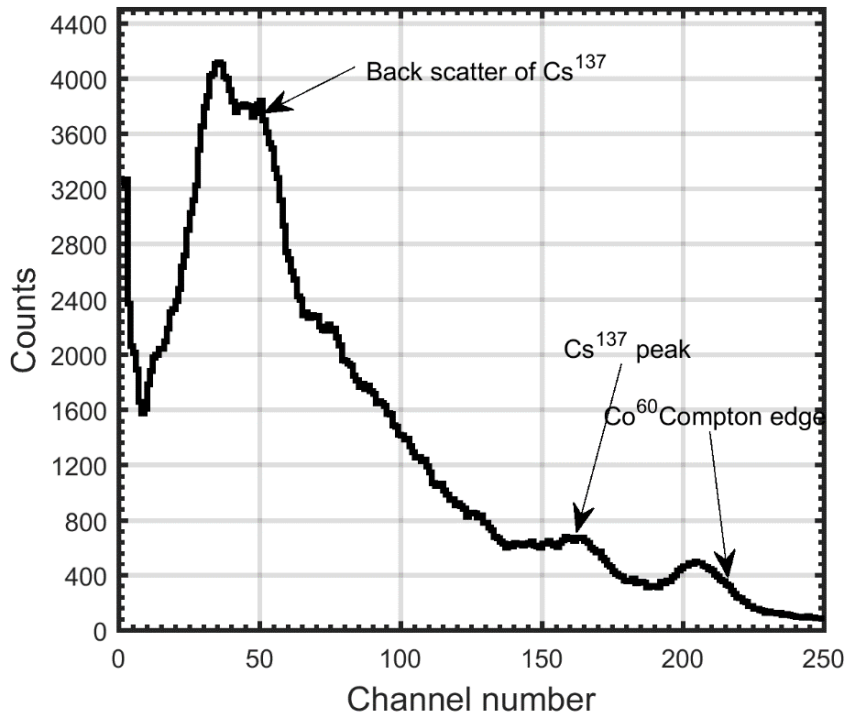

Figure 5-1 An example of gamma-ray spectrum of BH01 recorded with the 7301 litho-density tool. Y-axis presents gamma-ray counts and the x-axis is recording channels. The Cs^{137} peak, Co^{60} Compton edge and Cs^{137} backscatter peak are shown on the spectrum. Identifying these features helps us to have a better choice for the Compton window.

The HMI calculated using these windows are cross-plotted with the iron assay for BH01 as shown in Figure 5-2. The square of the correlation coefficient between HMI and iron is 0.64, which is acceptable. For the second set of windows, the low energy part is kept the same and for the high energy region a narrower window from channel 100 to 150 is chosen to avoid the Cs^{137} peak and its backscatter (Figure 5-3). The results improved noticeably from an R^2 value of 0.64 to 0.75. This shows the importance of the proper selection of windows. In this case, the Cs^{137} source is applied to stabilise the detector, but the emitted gamma rays do not interact with the surrounding medium. Therefore, the Cs^{137} peak and its backscatter do not contribute any information related to the surrounding formation and excluding these energy regions increases the quality of the analysis.

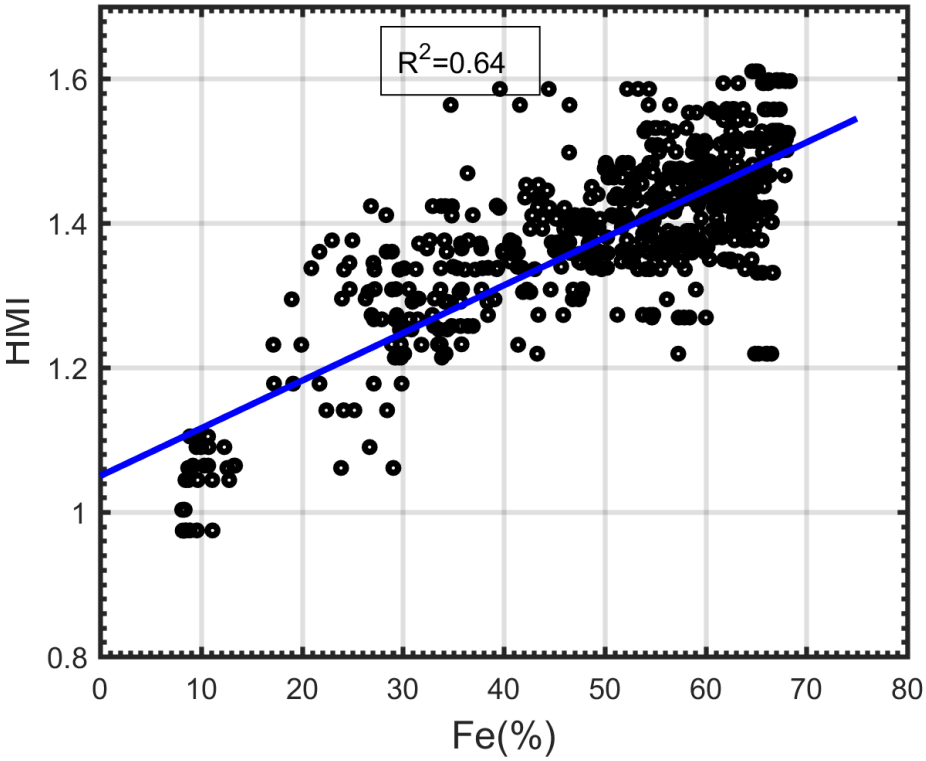

Figure 5-2 HMI vs iron assay for BH01 using channels 50 to 170 for the Compton window. The correlation is quite good with $R^2 = 0.64$.

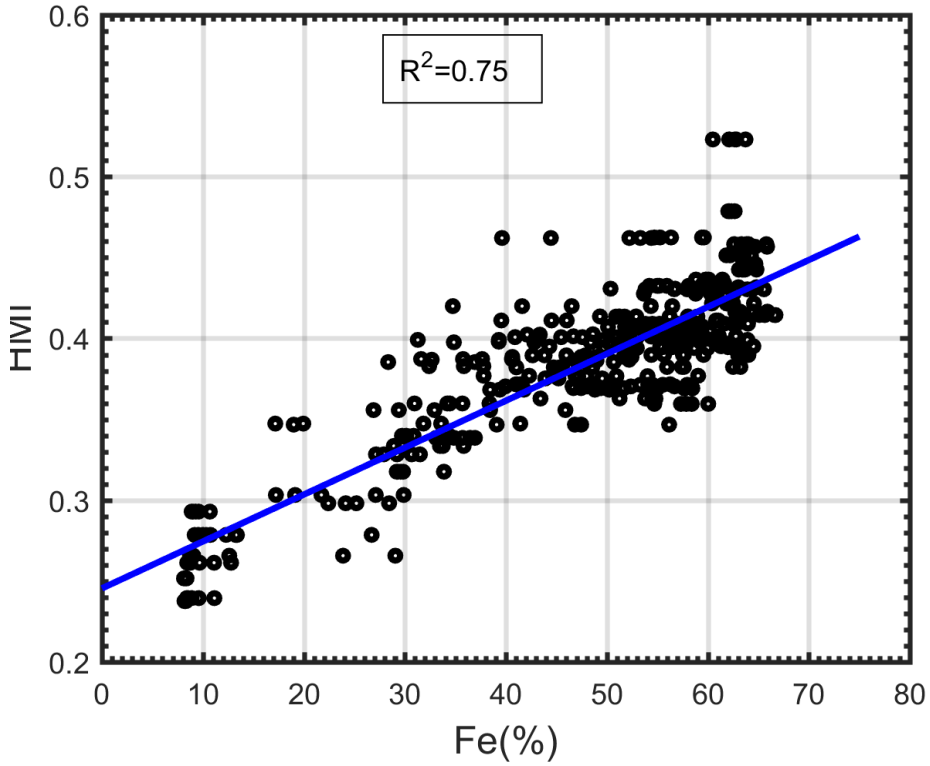

Figure 5-3 HMI vs iron assay for BH01 using channels 100 to 150 for the Compton window. The correlation is improved to $R^2 = 0.75$.

The same approach is applied to the spectra from borehole 02 (BH02) since the spectrum has the same format, as shown in Figure 5-4. Similar to the gamma-ray spectrum of BH01, major features such as the Cs^{137} peak the Compton edge of Co^{60} and backscatter peak of Cs^{137} can be identified in the spectrum. HMI was calculated by applying the wider Compton window, from channel 50 to 170 and was cross plotted with iron assay as depicted in

Figure 5-5. Applying a narrower Compton window, from channel 100 to 150, also improves the HMI and iron assay correlation from $R^2 = 0.74$ to $R^2 = 0.78$ as shown in Figure 5-6.

In Figure 5-7 we plotted a histogram of the iron percentage for BH01 and BH02. Both boreholes reveal high-iron concentrations that show they are located in iron-rich formations. In BH01 the iron concentrations are from 10% to 66% where more samples contains 50% to 66% iron. Iron in BH02 has slightly higher percentages, with a maximum of 68%, and a number of samples with more than 60% iron are three times higher than BH01. Therefore, iron rich intervals in BH02 are more than in BH01, which might be the reason for the better correlation of HMI with iron assays for this dataset.

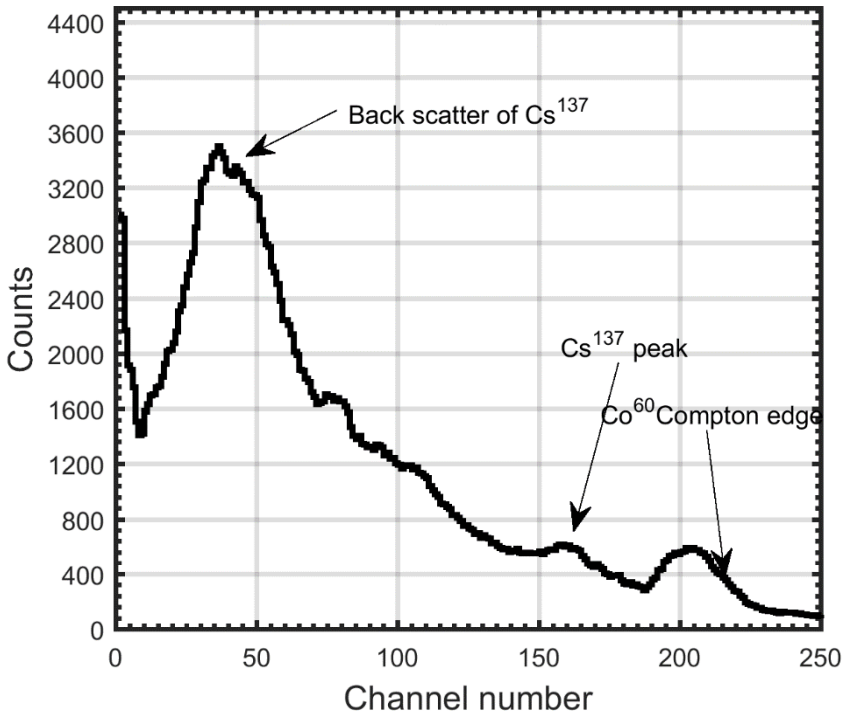

Figure 5-4 Gamma-ray spectrum of BH02 which is recorded with the 7301 litho-density tool. The spectrum is similar to BH01. Important peaks such as Cs^{137}, can be observed here.

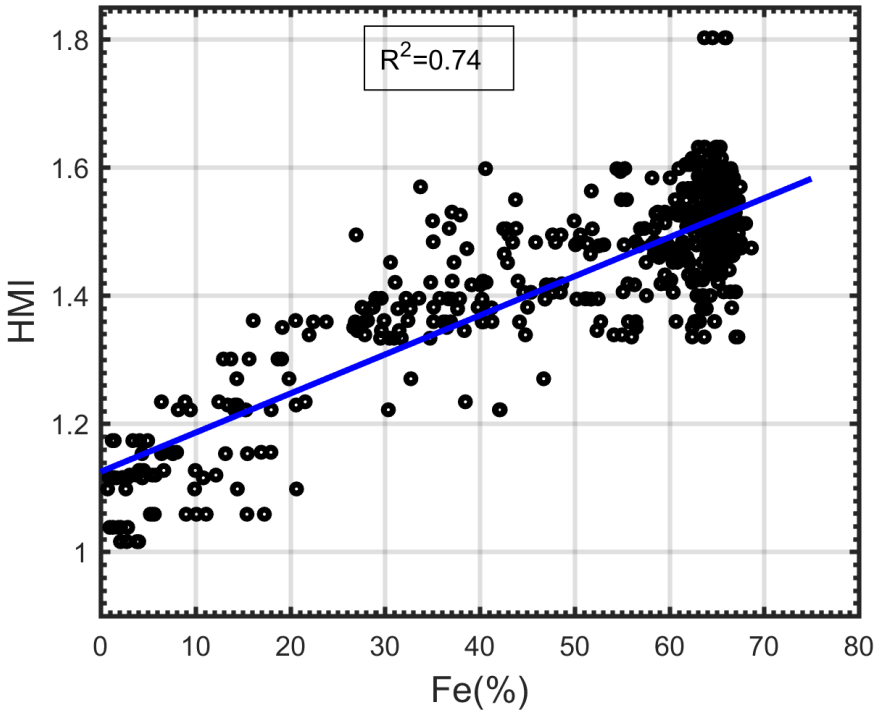

Figure 5-5 HMI vs iron assay for BH02 using the Compton window channels 50 to 170. The R^2 of 0.74 suggests a good correlation between HMI and iron assay.

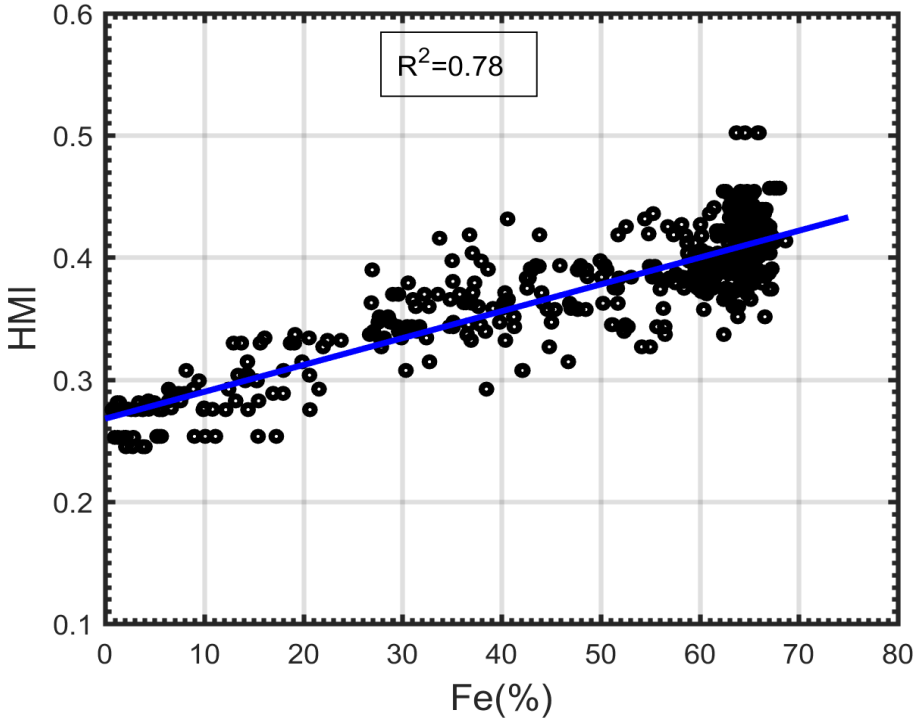

Figure 5-6 HMI Vs iron assay for BH02 with a narrower Compton window, channels 100 to 150. The correlation also improved for this borehole.

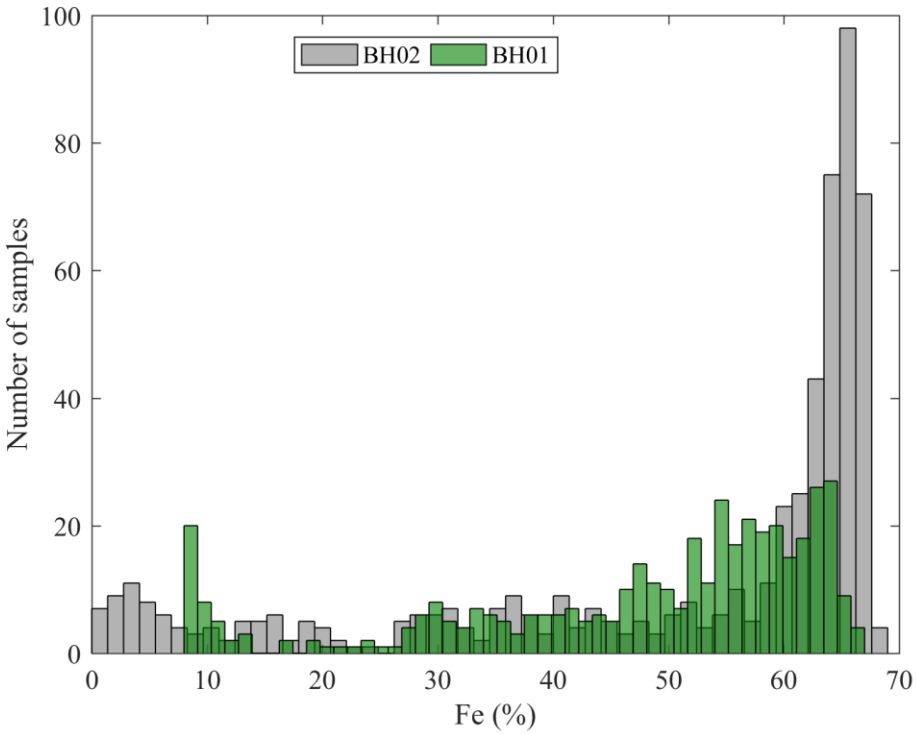

Figure 5-7 Histogram plots of Fe assay in percentages for BH01 and BH02. The iron percentages range is from 10% to 66% for BH01 where at 10% there is a peak. This peak can be a result of a cut-off threshold in which all values less than 10% are considered as 10%. For BH02 there is no cut-off threshold and iron percentage varies from 0 to 68%. We observe that BH02 contains more samples where the iron percentages is greater than 60% in iron-rich formations.

5.2 DATASET FROM SPECTRAL GAMMA-RAY TOOL

The other tool used in the BH01 and BH02 boreholes was a spectral gamma tool, model number 7201, also from Century Wireline Services (Century wireline services 2015). This tool measures the natural gamma radiation of a formation and records in three channels related to the potassium, uranium and thorium content. The tool, similar to the litho-density tool, has a small Cs^{137} source with energy of less than one micro-curie to stabilise the gain of the spectrometer. This small source is located very close to the detector in such a way that any gamma rays emitted from it do not interact with the medium surrounding the borehole. The spectra are recorded for every centimetre, into 256 energy channels with a logging speed of 1.5 m/min. The features presented in Table 5-1 for the litho-density tool, Century 7301c, are similar to the spectral gamma tool with extra features shown in

Table 5-2. The tool used a large CsI crystal with dimensions 3.81 cm in diameter and 30.48 cm in length, located at the bottom of the tool. The tool underwent a primary calibration at a calibration pit with known radioactive concentration before being deployed for field measurements (Century wireline services 2015).

Spectral gamma tool	
1. Potassium (%)	Offset 135.63 cm
2. Uranium (ppm)	Offset 135.63 cm
3.Thorium (ppm)	Offset 135.63 cm
Pressure	232 kg/cm^2
Weight	16.82 kg
Length	167 cm

Table 5-2 Features for spectral gamma-ray toolCentury 7201. Note that "Offset" means the distance from the top of the probe.

The recorded spectrum for BH01 is plotted in

Figure 5-8. There are no gamma-ray counts in the channels greater than 100. This is due to the pre-processing, which extracts the potassium, uranium and thorium counts from the spectrum. The peak observed at energy channel 55 is related to Cs^{137} backscatter. For this analysis, the spectrum was integrated over 1-meter intervals to improve the counting statistics. As discovered in the previous section, the Cs^{137} backscatter region should be avoided when calculating the HMI. Therefore, energy channels 1 to 20 and 22 to 42 were selected for the photoelectric and Compton windows respectively. Computed HMI values are cross plotted with iron assay data for BH01 and BH02 and shown in

Figure 5-9 and Figure 5-10. There is no obvious correlation between HMI and iron assay for BH01. BH02 also shows a very poor correlation, with an R^2 of 0.24.

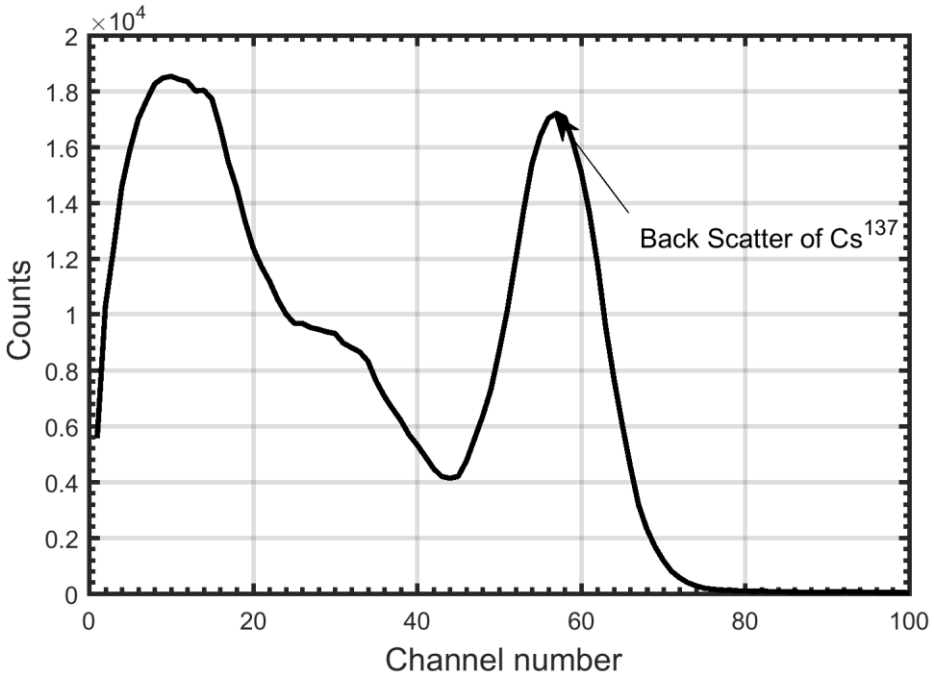

Figure 5-8 Spectrum recorded with the 7201 spectral gamma tool.

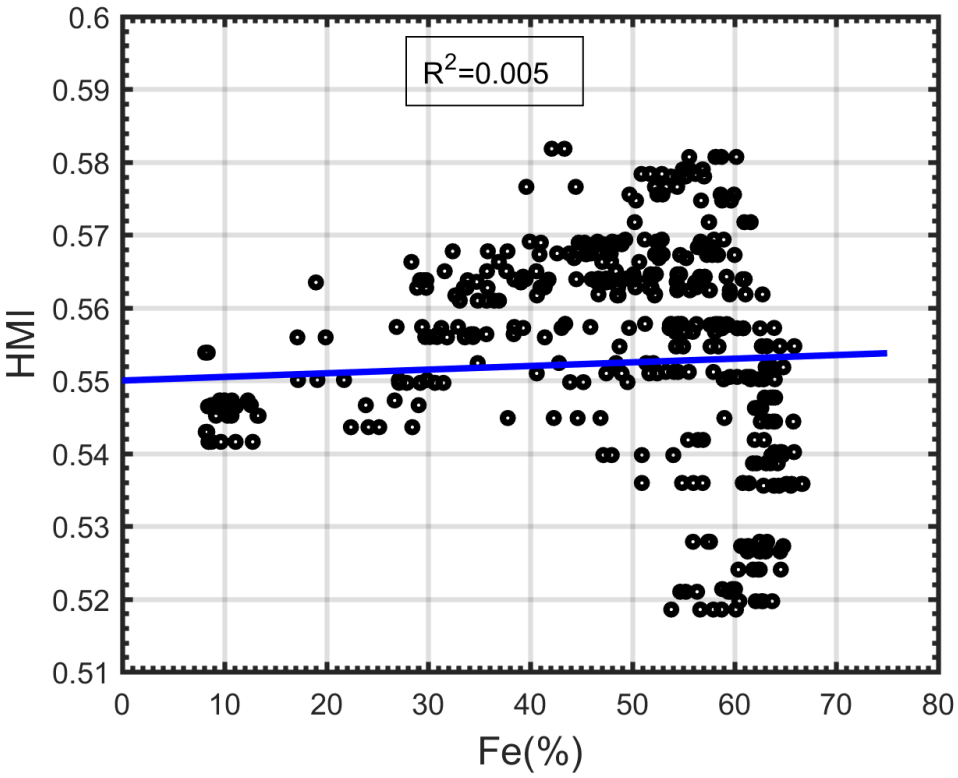

Figure 5-9 HMI vs iron assay calculated from the 7201 spectral gamma tool for BH01.

This lack of correlation is the result of poor counting statistics in the gamma-ray spectra due to the rather fast logging speed of 1.5 m/min. In this formation the number of gamma rays which can be recorded with a spectral gamma tool is less than 200 counts per second (Kepic 2014). Therefore, the speed of 1.5m/min can provide 4000 counts of gamma rays for half-meter intervals. This number is one fifth of the minimum count required for a good quality spectrum, 20000 counts, that was calculated in section 3.2.4. Hence, without a radioactive source, the quality of the spectrum decreases. Moreover, the spectra are cut off below channel 100, which leaves a very narrow energy region for the photoelectric window. Similar to the results from the litho-density tool BH02 shows a slightly better HMI/iron assay correlation compared to BH01. As already discussed this might be due to the higher percentage of iron rich formations in BH02. The final section of this chapter describes how HMI values may be related to overall lithology. Since lithology information is provided only for borehole BH02, we only present the results for this borehole in the following section.

5.3 HMI CORRELATION WITH LITHOLOGY FOR THE BOREHOLE

Previous chapters have shown how HMI is related to the chemical composition (Z_{eff}) of a medium in that it measures variations in Z_{eff}. In principle therefore, HMI can also be used to map lithological changes. To study this link, HMI logs from both the litho-density and the spectral gamma tools are plotted along with the total gamma-ray counts and iron assay from BH02 as depicted in Figure 5-11. In order to ensure that both tools are presenting data from the same depth the gamma-ray total counts logs measured in each tool were applied as a reference log to match the depth for both tools. However, for the sake of simplicity we only present one of the total count logs in Figure 5-11. The first log from the left is the gamma-ray total count (TC), measured with the litho-density tool. Both HMIs are plotted together to visualise which one corresponds better to the lithology. The TC log shows a number of peaks at different depths. These sections correspond to low HMI and high TC values and indicate shale-rich lithology that has a higher gamma signature due to their higher potassium content. The low-iron content of shales results in a lower average atomic number and consequently a lower HMI. High-grade iron ore and low grade ore intervals correspond to high and medium-high HMI values, respectively. TC gamma log has lower values for both high and low iron

grades. The BIF (banded iron formation, waste rock) lithology units are characterised by low HMI and low TC gamma values.

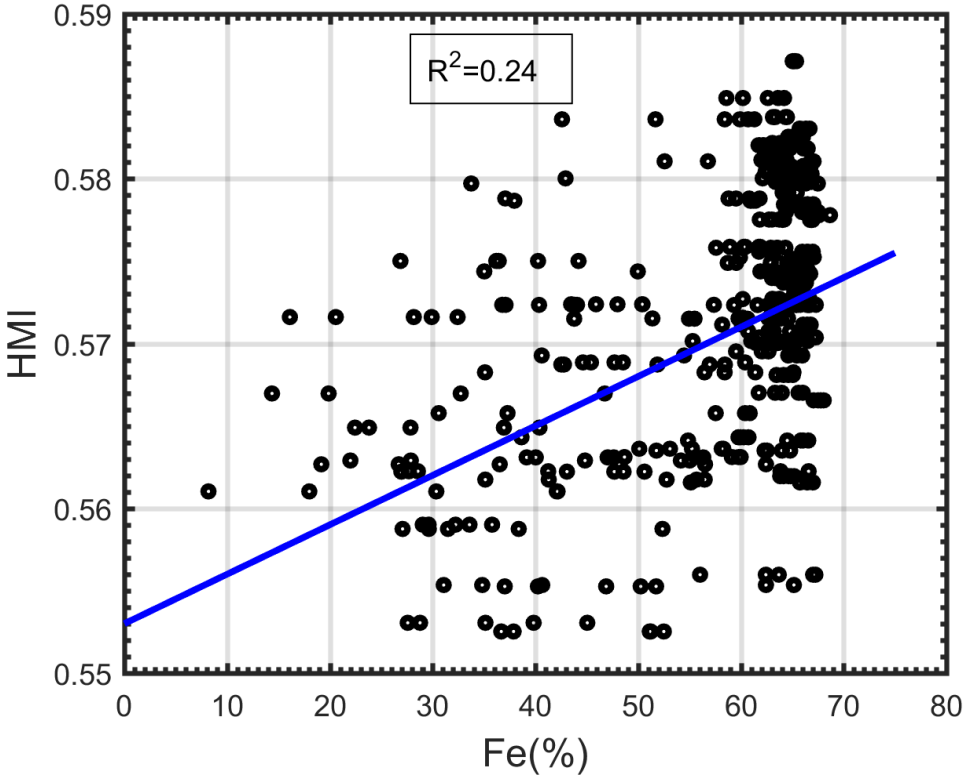

Figure 5-10 HMI vs iron assay calculated from the 7201 spectral gamma tool for BH02.

To summarise, ore lithology corresponds to high HMI and low TC; BIF corresponds to low HMI and low TC; and, shales are characterised by low HMI and high TC. A combined analysis of the HMI (from the litho-density tool) and TC logs is therefore sufficient to separate the lithology. Unfortunately, the HMI calculated from the spectral gamma log cannot separate iron ore and BIF in all instances (values are in the same range for both lithology), but can distinguish the shale units from the other lithology.

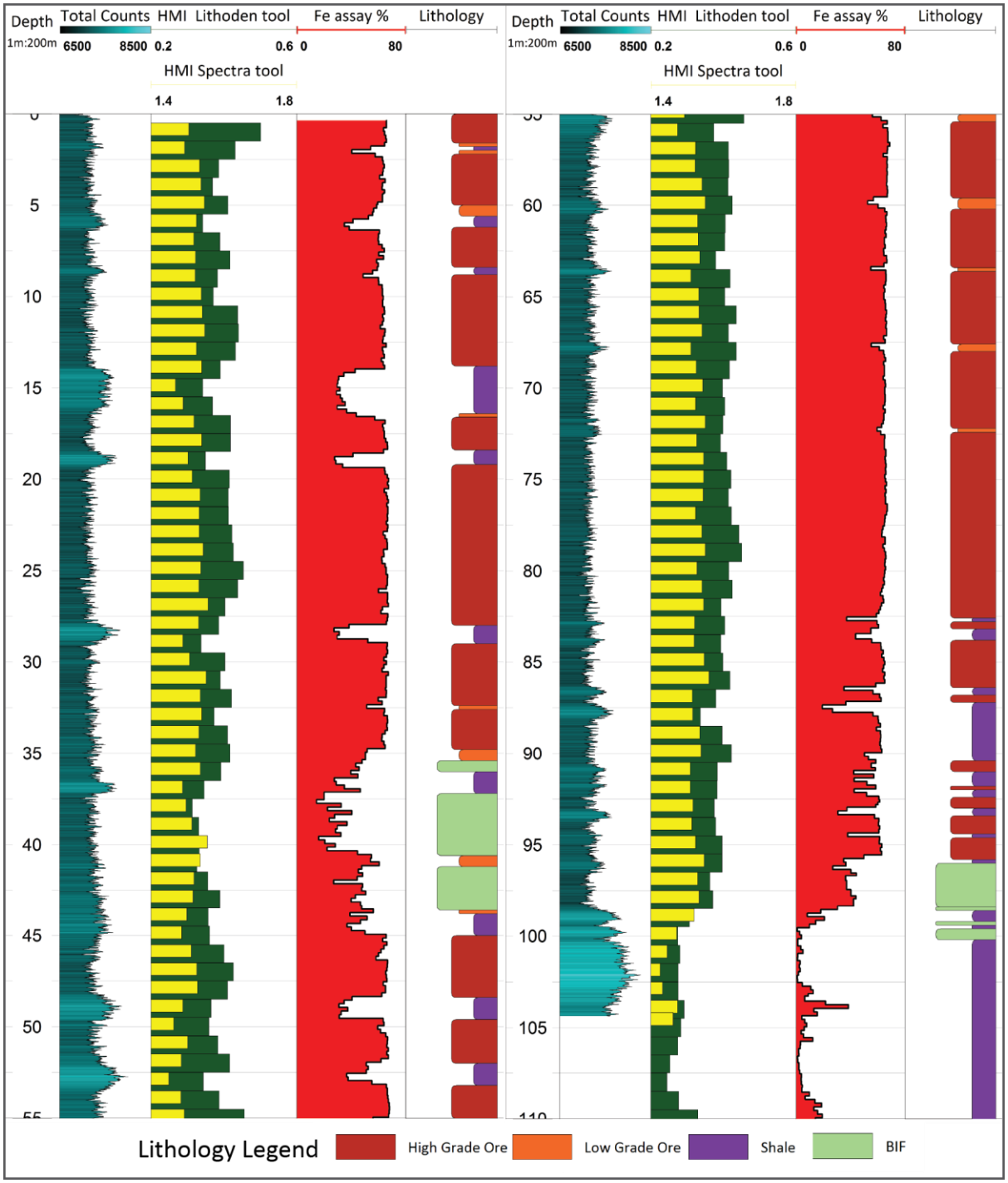

Figure 5-11 Log plots for borehole BH02; left part is from 0-55 m, right part from 55-110 m depth. The respective logs from left to right are: total count gamma (TC), HMI from litho-density log (green) and HMI from spectral gamma log (yellow), Fe% from assay and the lithology log on the right. High TC and low-medium HMI values correspond to shale units; high HMI and low TC correlate to iron ore lithology and high Fe%; low HMI and low TC indicate BIF (banded iron formation, waste rock).

CHAPTER 6. FROM DOWNHOLE TO THE AIR: AIRBORNE RADIOMETRICS

The promising results in applying the HMI technique to target lithology variations and mineralised zones (iron concentrations' regions) in the borehole environment encouraged trialling a similar analysis of the gamma-ray spectra from airborne surveys. Over the last forty years, Geoscience Australia and the State Geological Surveys plus the Northern Territory Geological Surveys have conducted low-level, airborne gamma-ray spectrometry covering more than 80 per cent of the Australian continent (Wilford 2009). Therefore, any improvement in analysing the gamma-ray spectrum can be performed on these existing high-quality datasets to gain new insights into geological/soil processes.

Another reason to look at the scattered radiation in airborne datasets is that data quality has improved greatly over the last two decades. This is due to better quality scintillators and electronic signal processing to produce full spectrum output rather than just Total Counts and K, U, Th estimates. Typical geophysical airborne detectors consist of a package of four 10.2 cm × 10.2 cm × 40.6 cm sodium iodide crystals with a total volume of 32 litres (Grasty 1995). Spectra are recorded in at least 256 energy channels, ranging from 0 to 3 MeV, which spans the full spectrum of gamma rays from natural radioisotopes. With flying heights between 80 m to 100 m, and now often at 25 m, the attenuation from air can be largely ignored, which will result in a high quality spectrum even in the low energy channels critical for the HMI technique (Minty, McFadden, and Kennett 1998).

All of these improvements in airborne radiometrics have been used to provide better (lower noise, higher spatial resolution) maps of natural radioisotope activity. Hence, radiometrics tend to be viewed as a geochemical mapping tool. With the full spectrum data it is now possible to analyse gamma rays that scatter within a thin top layer of the earth rather than just the "primary" gamma rays that come to the detector unhindered. Normally, the gamma rays that scatter within the earth are "background" or noise and are removed. However, these gamma rays have interacted with the earth and soil, and characterise the relative strengths of photoelectric (PE), and Compton interactions. Thus, the HMI would provide a new independent measurement of the near surface earth properties. In the following section, HMI is calculated on an airborne dataset from the Elashgin area in Western

Australia, and compared with the geology of the area and other radiometric measures. The question is, does it provide extra information and something novel in this example?

6.1 SOME BASICS ABOUT AIRBORNE RADIOMETRICS

Airborne radiometrics measures the natural gamma rays emitted from the earth's surface by using gamma-ray detectors in an aircraft and flying low over the land. For a typical survey, using a 32-litre sodium iodide crystal detector the survey is carried out within 100 m of the surface, where most gamma rays captured in the detector originate from tens of cm under the surface of the ground (Grasty 1979). Thus, as an airborne geophysical method radiometrics is not a particularly penetrative measurement. Various studies show that nearly all of the detected gamma rays originate from within 30 cm to 40 cm of the surface, see Appendix 1. Despite the limited depth of penetration radiometric surveys have many applications when used as a geochemical mapping tool, such as gold and uranium exploration, basic regolith/ outcrop geological mapping, alteration mapping and soil-type mapping (Herrmann 2010; Jones et al. 2010).

In a conventional spectrum processing method for airborne radiometrics the count rates in three principal windows of energy channels centred around 1.46 MeV (K), 1.76 MeV (U) and 2.62 MeV (Th) are used to obtain equivalent estimates of elemental abundances of these radioisotopes (Minty, McFadden, and Kennett 1998). The calculations are a little more complicated as the presence of higher energy primary gamma rays and daughter products requires "stripping out" of the interference of the other elements and their daughter products. After the basic corrections for energy calibration, altitude variations and stripping, the estimates of concentrations of the main radionuclides – K, U, Th - are produced (with the assumption these concentrations are uniform in the top soil layers and in "secular equilibrium", which given the complexities of soil profiles is not an entirely safe assumption). HMI analysis, based on the ratio of count rates on a low energy part of the spectrum (50 keV to 300 keV) divided by the counts in the Compton region (a range between 350 keV to1000 keV), has never been performed in radiometric spectroscopy. A possible reason for the lack of such analysis is that the low energy region is not traditionally collected, or used in later processing. In any case, adding HMI analysis should provide Fe plus the usual K, U, Th concentrations (assuming that Fe is the dominant high-Z element), and as Fe

is a major constituent of many minerals/rocks it should be at least as useful as any of the traditional radionuclides.

Radiometric signals change with variations in the mineralogical components of the parent materials, with felsic rocks typically having higher radiometric signals due an abundance of K-feldspars and mafic rocks having lower radioactivity (Rawlins, Lark, and Webster 2007). In many cases, weathering and alteration patterns are well mapped by radiometrics by the actions of leaching and concentration in other geological media. For example K is higher in many altered rocks (Dickson 1997), while weathering may result in a loss of K in all rocks as the minerals containing K tend to be easier to erode (an example end product is high silica sands). Also, many porphyry intrusive have zones of K-rich rocks that can be used to identify possible porphyry-related Cu deposits (Telford et al, 1990). On the other hand U and Th contents can be enhanced compared to K as weathering advances, or changes as the ph values of groundwater rise-and-fall as the regolith formation (Wilford and Minty 2006). Therefore, radiometric surveys when combined with regional lithology and geochemistry information can provide a better understanding of a survey area.

In environmental and agricultural applications understanding the land's properties such as soil texture, depth and water holding capability is very difficult spatially (Pracilio 2007); however, ground surveys and soil mapping may be combined with airborne gamma-ray spectrometry data to create high resolution soil maps from both inputs. Gamma-ray spectrometry (radiometrics) can be applied for soil sensing since the K, U and Th elemental distributions often correspond to soil textures and properties (Cook et al. 1996). Gamma-ray radiometric measurements that have been available for the last few decades are capable of improving the speed and efficiency of soil mapping. HMI analysis can add another dimension to the existing use of radiometrics, by tracing lithological units with elemental iron variations (or other heavier elements such as copper, zinc, lead etc). Soil mapping is where HMI is likely to be of greatest importance as soils are environments for plant and animal life and iron is an important element in living organisms.

6.2 STUDY AREA

6.2.1 Location and survey parameters

The Elashgin is an area located 206 km northeast of Perth and 10 km southeast of the town of Wyalkatchem and in the northern wheat-belt region of Western Australia, (Figure 6-1). The survey data is in the AMG84 coordinate system (a Universal Transverse Mercator projection) is derived from the Australian Geodetic Datum and is contained within zone 50 with a central meridian of 117 degrees. Coordinates of the northwest airborne survey corner are 538614 mE and 6541420 mN. High resolution and low-level airborne magnetics-radiometrics were collected over a 77 km^2 survey area. The radiometrics survey was conducted by UTS Geophysics on behalf of Agriculture WA in 2001, where measurements were made at 20 m intervals, with flight height 20 m above ground and flight lines spaced 25 m apart. This survey provided an early example of such low-level high-quality airborne data, and is a well-studied data-set in Australia. Overall, 3442 line kilometres were flown on this survey with the main survey area located in the valley area. Hence most gamma rays were collected from an ellipsoid about 40 m in width and 80 m in length on the ground (Taylor et al. 2002). Data were collected during the mid-summer, dry season; therefore, it is believed to have minimal gamma-ray attenuation from vegetation and soil moisture (Verboom and Pate 2003).

To measure the gamma rays a 32 L thallium-doped sodium iodide crystal was used as a detector, which allowed for a signal to be collected despite the flying speed. Gamma rays were binned into 256 energy channels spanning 0 to 3 MeV with a sampling period (a spectrum) of half a second (Verboom and Pate 2003). More information related to the survey parameters area can be found in the logistics report by UTS (UTS Geophysics 2001).

Figure 6-1 Location of the Elashgin area on Google Earth is shown with a red square and it is enlarged in the top-right map.

6.2.2 Overview of the geology of the Elashgin area

The soils in the area are composed of clays and sandy loams with varying amounts of ironstone gravels, often masked from field observations by thin cover. The flat valley in the centre of the study area is an ancient drainage system (paleochannel) now filled with alluvial and fluvial sediments (Beckett 2007). In the valley floor quartz-feldspar porphyry occur along these palaechannels. The valley then drains into a nearby salt lake. The bed-rock is mostly comprised of seriate adamellite and prophyritic granites with numerous dolerite dyke intrusions (Chin 1986); the trend of the dykes are mainly east to west. In the north-west of the valley the soil is dominated by a reworked sandplain, with white and yellow sand, which contains locally derived limonite pebbles with lateritic gravel outcrops (Chin 1986). On the

slope of the outcrops, in the south-east of the valley, sands and gravels are derived from the weathering of the underlying bedrock. Topographic highs are associated with granite outcrops, which are relatively high in potassium bearing minerals.

6.3 DATA ANALYSIS

The Elashgin dataset was downloaded through an open source document available by DMP Geoview (2016). The dataset is provided in two forms; a raw dataset that is in a text file format and a processed dataset in a gridded format and this survey is one of the very few that has such data in the public domain. In the next sections only the raw dataset that contained the coordinates and the 256 channel spectrum for each measurements are used. UTS undertook the basic calibration, levelling and stripping, which is briefly explained as follows (UTS Geophysics 2001):

- Reflown lines are eliminated from the data.
- The maximum noise fraction method is performed to reduce statistical noise from the 256 channel dataset (Dickson 1999).
- Noise (background) is removed from channels 30 to 250, which contained the interesting part of the spectrum, and afterwards the spectrum between the potassium and thorium peak was recalibrated (energy calibration).
- Other corrections such as cosmic, radon, height and aircraft background corrections were applied (Minty 1992) in flight.
- The 256 channels data is sorted into 5 main windows. These windows are as follows: total counts window, Potassium window, Uranium window, Thorium window and a window for low energy uranium.

This conventionally processed data will be used for comparative purposes to the HMI map and to assist in interpreting the various landforms. Raw spectral data was used to calculate HMI values. Therefore, the raw spectrum is the input to the HMI calculation. The corrected raw spectrum was also used to calculate the relative intensities of K, U, Th, which was done for consistency in order to relate to the HMI calculations (rather than using the already gridded and translated maps from the survey company). After calculating the HMI values a map was generated (with OASIS software) from these values alongside the existing K, U and Th maps. All of the maps are used to make a basic lithological interpretation of the survey area. This interpretation is then used to cross-check whether the HMI product detects the geological features expected: ironstone gravels and iron-rich lateritic products.

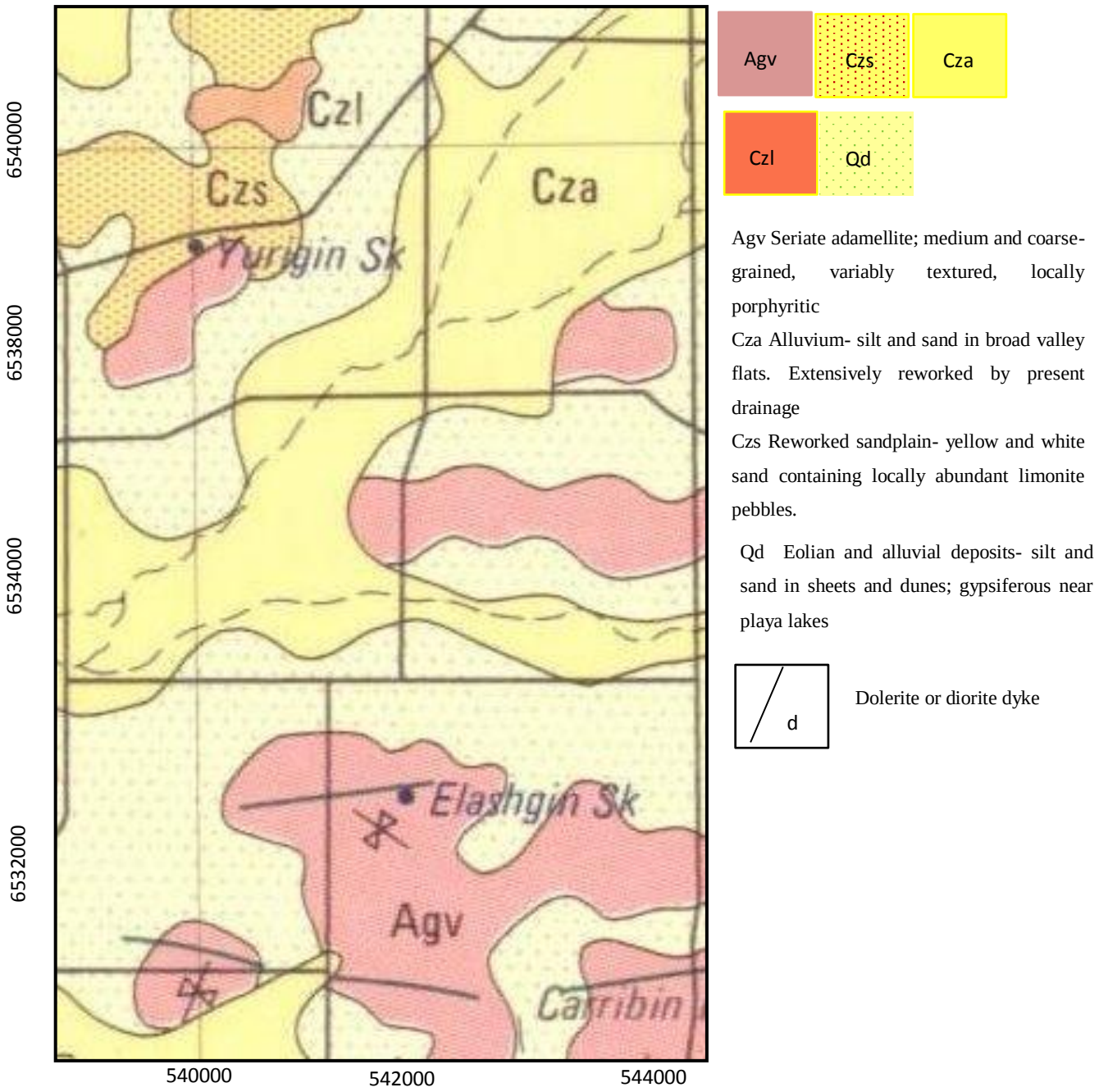

Figure 6-2 Schematic geology map of Elashgin area(Chin 1986).

Additionally, a digital elevation model (Portal 2017) for the survey area is used with other maps to aid the interpretation.

6.3.1 Radio-elemental maps of K, U and Th

The regular procedure for analyzing airborne radiometric starts with the potassium (K) map which is extracted from the potassium window by using a stripping technique to remove

effects from other radiosiotopes. The stripping, as discussed in more details in section 2.1.5, is based on choosing three windows to estimate K, U and Th peaks.

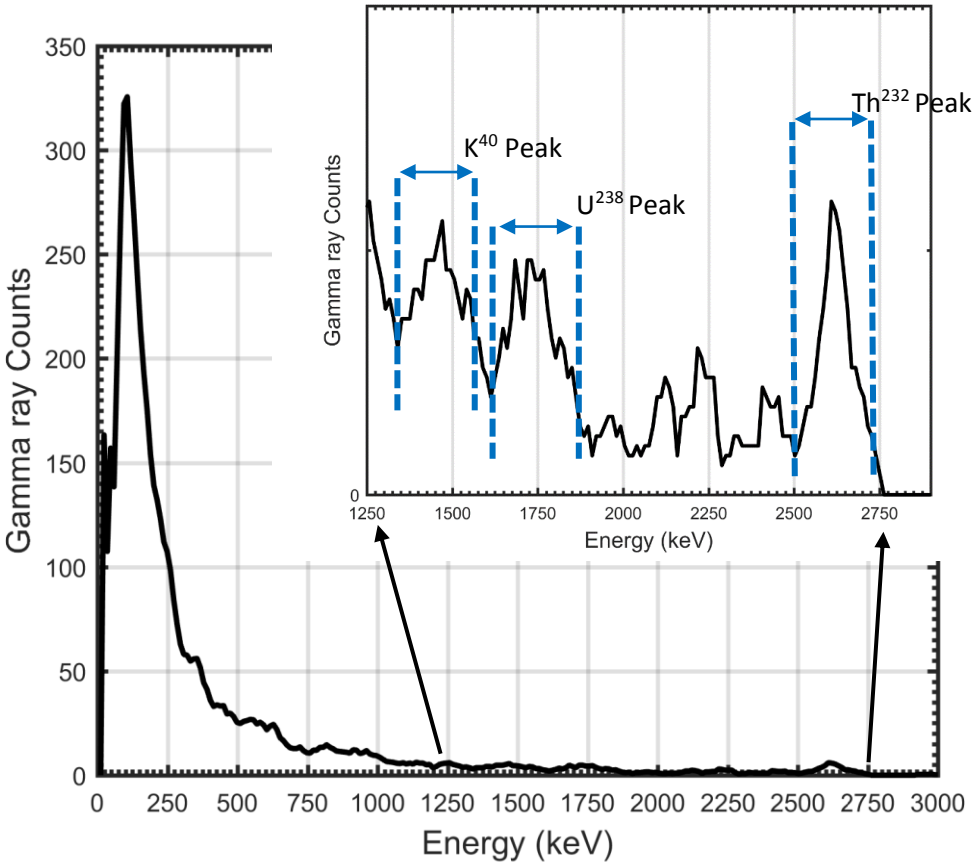

Figure 6-3 A spectrum from Elashgin survey. The energy range from 1250 keV to 2750 keV of the spectrum is enlarged to better illustrate energy windows chosen for each of K^{40}, U^{238} and Th^{232} elements.

Figure 6-3 shows a spectrum from Elashgin and windows that we defined to extract peaks of interest. Note that the spectrum was recorded in 256 channels, which means gamma rays energy from 0 to 3 MeV are binned into 256 channels. After binning (and correcting) the gamma rays in the windows for each peak K, U and Th maps are generated and gridded with a minium curvature method: Figure 6-4, Figure 6-6 and Figure 6-8.

The K map is also draped over the Digital Elevation Model (DEM) for better visualization of geological features associated with topography to assist the interpretation (Figure 6-5). Important features are categorized into various geological morphologies and all separated with black lines. These categories are labelled A, B, C, D and E on the maps as the following:

- Region A is assigned to valley floors, which contains various clays, loams and sands. All three elements, K, U and Th are relatively high in intensity with little variation throughout the whole valley. High potassium values are a result of clays and effect of waters on potassic-feldspar (Verboom and Pate 2003). In the clays K has a lower intensity across the valley (Taylor et al. 2002).
- Location marked with B, B1-B5, does not have a consistent radioactivity pattern and we observe variability throughout the study area. This area is dominated by seriate adamellite and porphyrictic granite. Areas with high amounts of K feldspar are reflected with high intensity in the K window, B2 to B4. There are two regions in this area with low K while U and Th intensity is still high: namely B1 and B5; these are interpreted as exposed ferricretes created by groundwater movements (regolith process) (Commander et al. 2001). This behavior is expected as iron-rich surface minerals are often Th and U enhanced while K is depleted (Dickson 1997).
- Region C: Residual quartz and sand plains are low in radioactivity, which is well reflected with very low intensity in all K, U and Th maps
- Region D: According to (Commander et al. 2001), the iron-rich lateritic horizons can usually be identified by higher thorium and uranium with lower potassium (as K is more mobile and U and Th tend to be chemically bound to the lateritic products and less mobile) and these horizons are typically located on the flanks of topographic highs. Thus, we would expect to find rings and/or spirals shapes on the slopes identified with DEM maps.
- Region E: It has the highest amount of potassium and relatively high Th and U. At the early stage of weathering of granite, removal of weathered minerals leads to an increase in K content (Dickson 1997). It is interpreted as partially-eroded granitic rock where K-feldspars are spreading into channels.

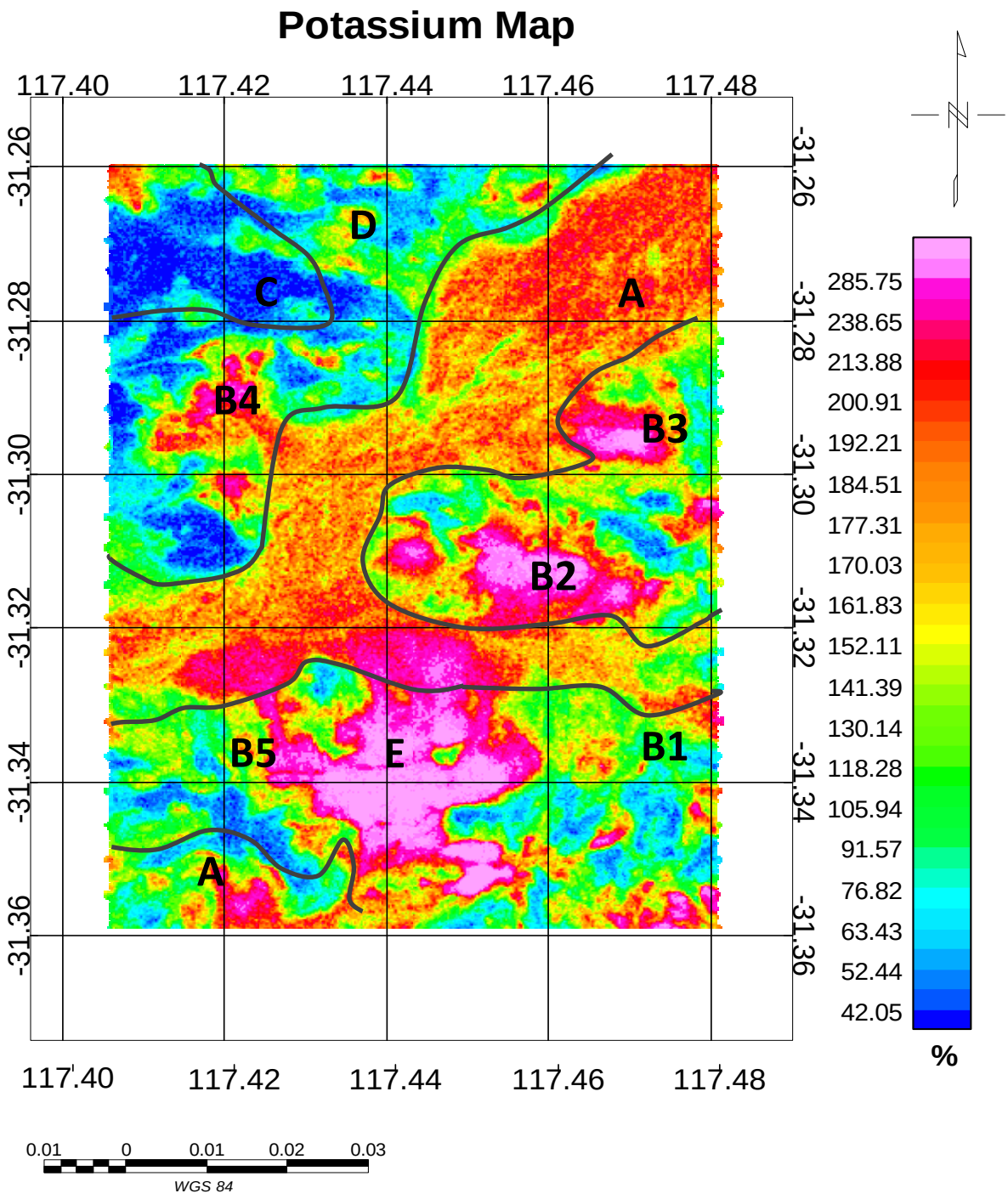

Figure 6-4 Potassium Map from airborne measurements of Elashgin area. Important features are labeled with letters A to E.

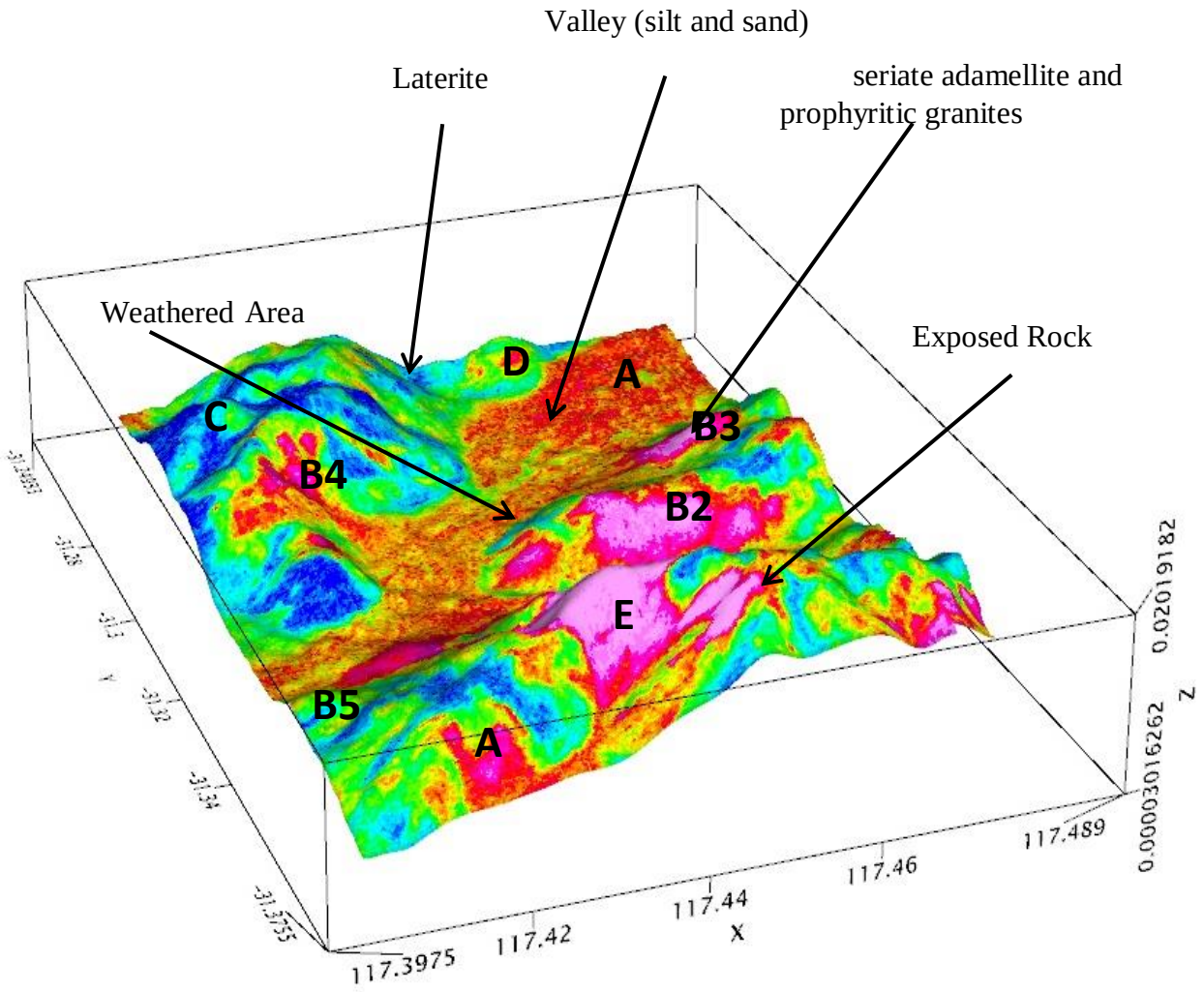

Figure 6-5 Potassium map draped over DEM of survey area with important features marked with A, B and C letters

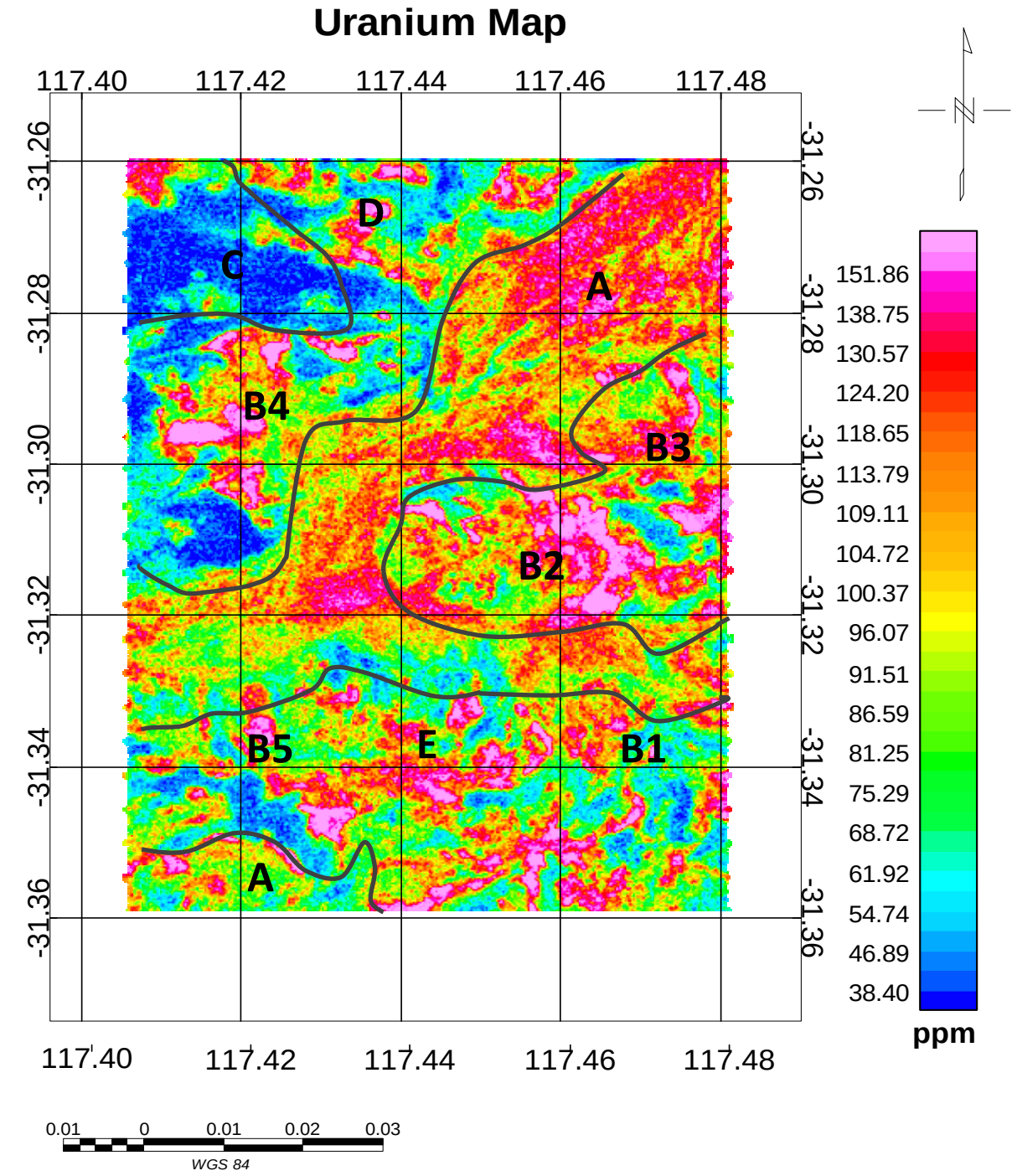

Figure 6-6 Uranium map. Significent features are identified similar to the potassium plot.

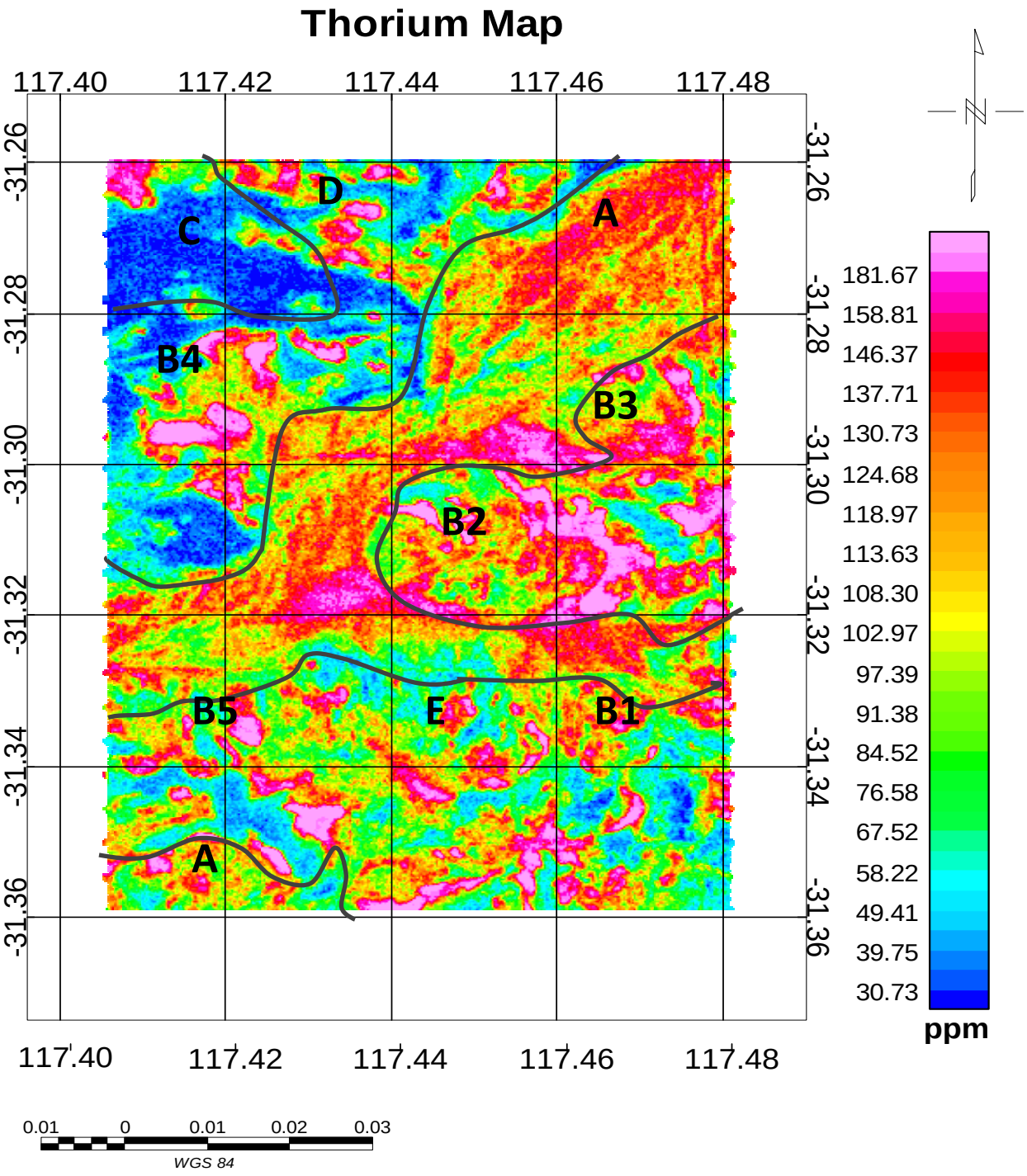

Figure 6-7 Thorium map, significent geological features can be seen as in the potassium plot.

6.3.2 Applying HMI to target high iron concentration

The two windows selected for calculating the HMI is as follow: the low energy window was chosen to be 50-300 keV, almost equivalent to the channels 5 to 27 and the high energy window, ranged from 350-1000 keV, corresponding to channels 32 to 90 on the 256 channel data. The HMI value was calculated applying the ratio of the high to low windows for each measured point and this was then gridded with minimum curvature in OASIS montaj software (Figure 6-). The grid size is 10 m, which is the half distance between measuring points along the lines. The same labels are shown the HMI map with the same alphabetical labels. Note the HMI map in Figure 6-9 has a noisy look as compared to the previous maps. This is due to the calculation of HMI where the ratio of two windows is used. Thus, it increases the sensitivity to statistical fluctuations in the gamma-ray counts, especially in the low energy region.

An analysis of the HMI and comparison with the K, U, Th maps and their corresponding analyses reveals that:

a) In region A there is a clear link between ironstone gravel patterns in the paleo-channel and the dendritic patterns in the HMI in this region. Generally, the flat valley, labelled as A in Figure 6-, has a low HMI intensity due to iron leached sands while the drainage channels inside the valley show higher HMI values. The higher values in the drainage area are expected because ironstone gravels from upper slopes are transported with water and deposited in these channels (Beckett 2007).

b) The link between high HMI and the high Th and U low K lateritic horizons on the slopes of the topographic highs is strong. These are interpreted to be the ferricretes and yellow sands mentioned in the U and Th interpretation by Commander et al (2001). In the B category, B1 to B5, the exposed regolith geology is a mosaic of exposed ferricretes that forms wave-like shapes moving up, down and across the slope. The B5 region is a rocky outcrop, which stands out with the highest HMI values and is also interpreted to be ferricrete produced from weathering.

c) The sandy areas in the valley A and the leached silica sands in area C, the reworked sandplain- with yellow and white sand containing locally abundant limonite pebbles, are low in Fe/HMI as expected of these materials

d) The topographic highs and corresponding high K values are granitic outcrops, and these should, and are, relatively low in HMI/Fe. This is true in areas E and areas just

south of B2 and B3. Region E, which has registered with the highest amount of potassium, displays low HMI. This region is eroding granite; hence, lower HMI is anticipated and seen in the HMI map.

e) Region D has a high HMI signature. This region is laterite (iron-rich materials) that also corresponds with high Th and U but lesser K.

There appears to be no corroborating soil data despite nearly 100 samples taken by UWA researchers (Pracilio 2007). Soil measurements taken from the DMP database of the area DMP Geoview (2016) are of uncertain quality and origin and did not correlate well with the HMI maps, or any of the radioelement maps. The results of analysis by Pracilio (2007) did not achieve a good correlation with the soil sampling either, Th, and U analysis (best with Th with a correlation of about 0.7). Taylor et al. (2002) also had difficulty relating soil samples to airborne data, but had better correlations of soil geochemistry with ground-based radiometric measurements. As soil sampling is very prone to spatial aliasing and effects of soil horizon layering, and may not be representative of the 40 m x 80 m footprint from airborne measurements any attempt in using ground truth for the Elashgin study has not been pursued further.

The independence and usefulness of HMI is confirmed by the non-resemblance to K, U, Th maps. The utility is shown by relating the various geomorphologies that are known and expected to be iron-rich by using the known relationships of K, U, Th and topography and broad soil typing based upon visual landform mapping to confirm high/low HMI areas are iron-rich or iron poor.

6.3.3 HMI and magnetic airborne

Magnetic were collected simultaneous with the radiometric data. Corrections and processing included diurnal correction, removal of residual parallax errors and micro-levelling techniques are applied (UTS Geophysics 2001). The regional magnetic gradient (International Geomagnetic Reference Field (IGRF)) was subtracted from the dataset and a magnetic map was generated in a grid format (Figure 6-10).

The airborne magnetic data in Elashgin provides an opportunity to compare the HMI map, with a magnetic map. Both can detect iron-rich formations if the iron is magnetic and

near the surface. Examining the magnetic map in Figure 6-10 indicates there is no significant magnetic mineralisation in this area, apart from dolerite dykes with east-west orientations intruding the basement rock. There is no correlation between the HMI and magnetic maps (Figure 6- and Figure 6-10 compared). The aeromagnetic map responds to magnetic materials, mostly magnetite bearing minerals, from surface to an about 200 metres or more. Whereas, the HMI technique only detects the surface material with high average Z content, which is likely to be the element of iron, but not deeply as the depth of radiometric investigation is limited to tens of centimetres. One method only detects magnetic iron minerals, and the other largely detects iron-dominated atomic number independent of the ferrous or ferric state of the iron. Thus, sometimes the maps will match, and often they will not. In Elashgin they don't match.

6.4 CONCLUDING REMARKS

A radiometric dataset from Elashgin area is used to evaluate the potential of HMI. If HMI from natural gamma rays measured in boreholes can target variations in lithology then so should airborne radiometric data be as amenable.

The normal practice in analysing radiometric data is to derive K, U and Th maps and use these maps for interpretation based on the measured or predicted radiometric signature of rocks (Dickson 1997). In recent years, there are some developments in spectrum analysis, but these are still focused on estimating radio-nuclide concentrations. For example, joint soil sampling and ground radioactive survey activities on a small scale over a region are used to build a relationship between ground studies and radiometrics. Then this relationship is applied to regional radiometric data for quick soil-typing interpretation on a larger scale, (Marchuk and Ostendorf 2009) ; (Taylor et al. 2002). Multispectral processing is another example of new radiometric analysis. In this technique gamma ray peaks are emphasized by removing noise with sophisticated estimators and incorporating all of the low amplitude peaks U and Th from isotopes and daughter products to generate better K, U and Th maps (Beckett 2007). Whilst these methods improve conventional radiometric analysis, they are largely based on removing "background noise" and increasing quality of the K, U and Th maps and not revolutionary in obtaining new information.

This thesis puts the focus on the generally neglected aspects of the radiometric spectrum, which is the scattered gamma ray radiation that has interacted with the other elements of the soils and rocks. The Elashgin case history demonstrates that low-level and high resolution full spectrum radiometrics provides good data for the HMI technique. As the HMI values are dominated by Fe concentration then it becomes a proxy for iron content. Thus as a new interpretation approach HMI can extract significant additional information from the radiometric spectrum. Areas composed of higher atomic numbers, mostly due to the iron content, such as ferricretes and laterite show up clearly in the Elashgin data without the need to be "interpreted" with respect to geological context. With the high resolution of modern radiometrics this technique works well for remote sensing; since very small features such as drainage channels are well reflected in the maps. Perhaps the most exciting aspect of HMI analysis for airborne radiometrics is not just the future, but the past: many high quality full spectrum data sets already exist and may be easily reprocessed to reveal new geological insights.

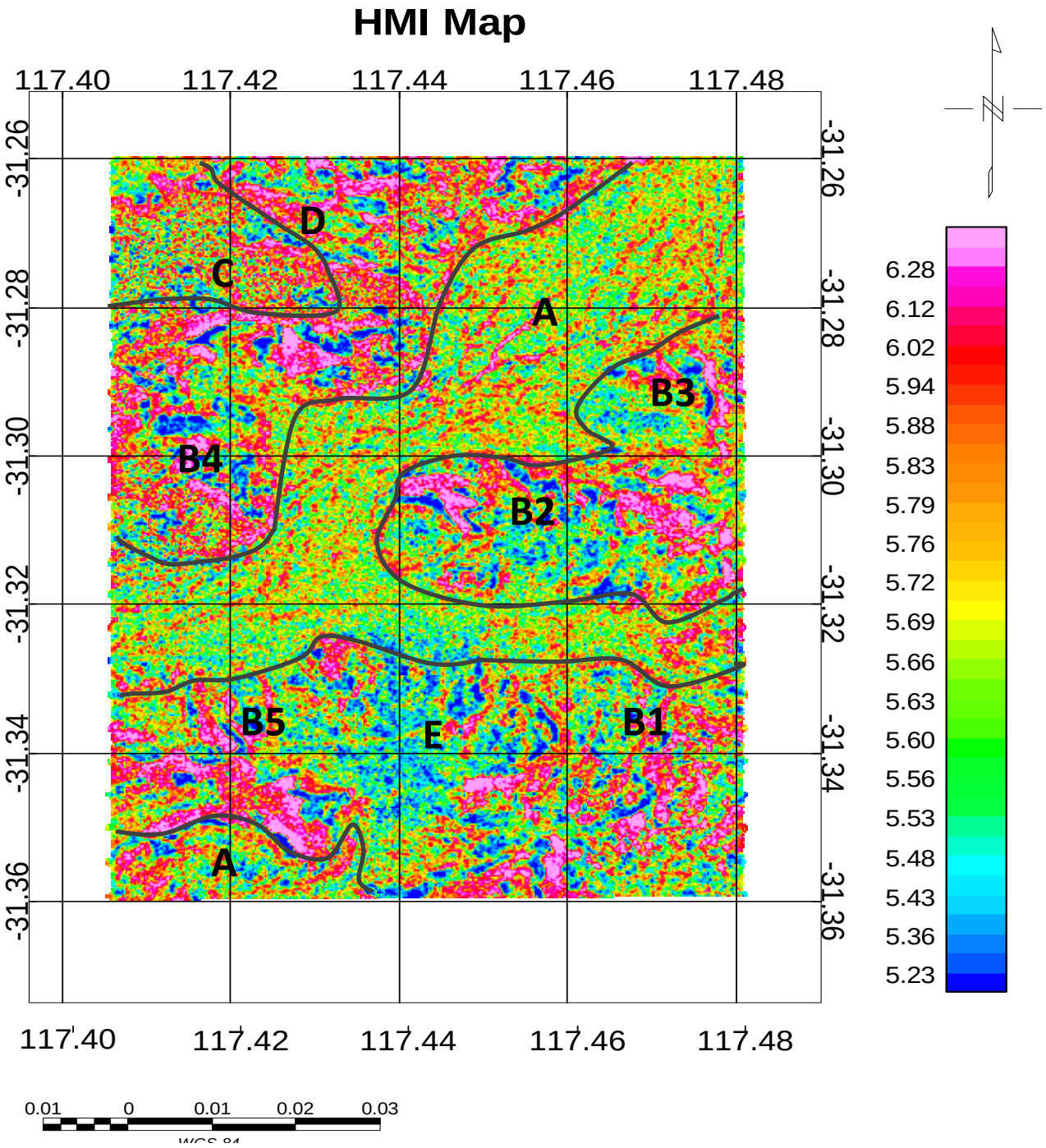

Figure 6-8 HMI values which were calculated from airborne radiometric of Elashgin survey, as it is explained in a text the variations in values follows iron concentrations in survey area

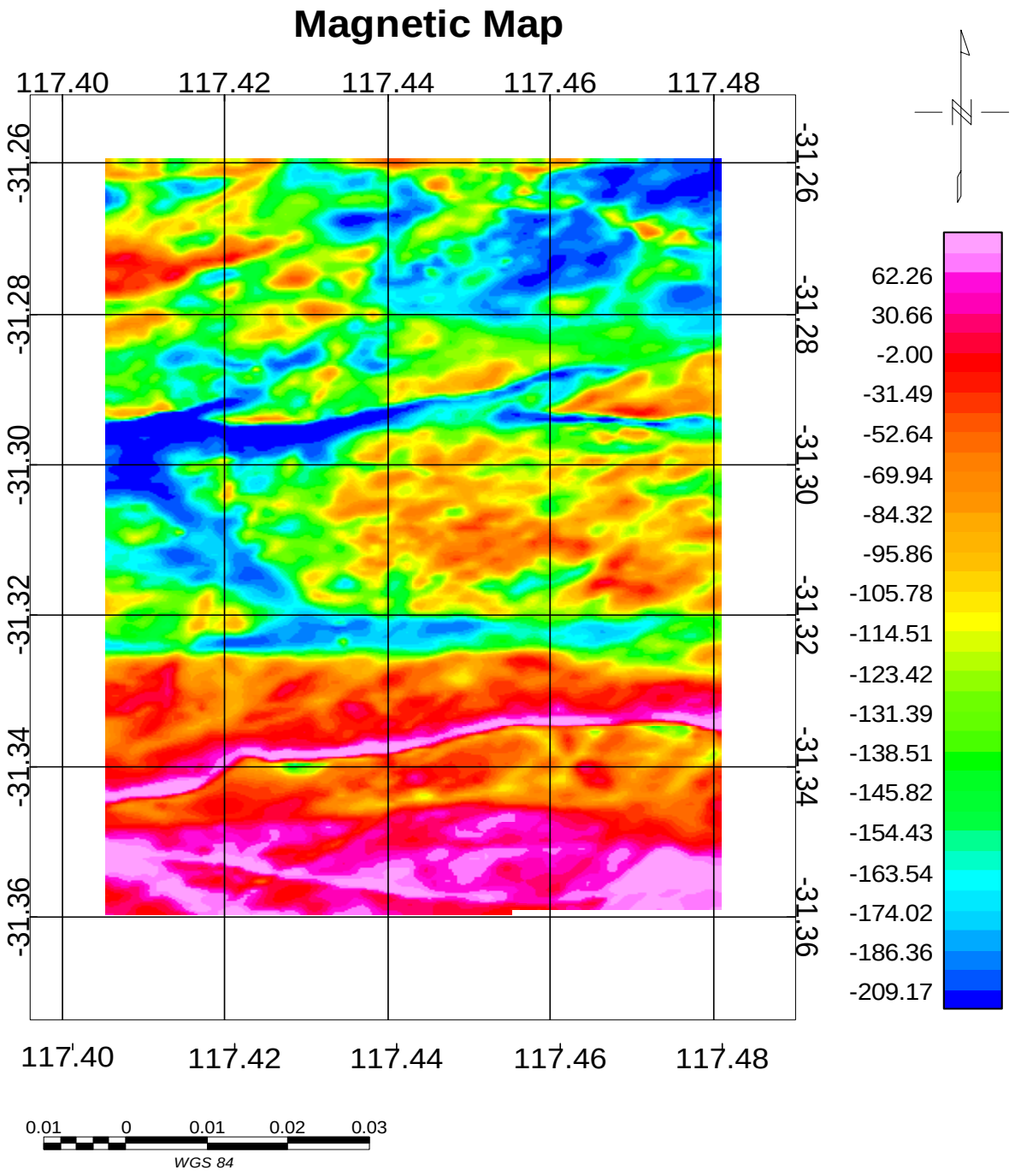

Figure 6-9 Aeromagnetic map of Elashgin area, basic corrections such as reduction to the magnetic pole and light filtering have been applied

CHAPTER 7. CONCLUSIONS

7.1 MAIN OUTCOMES AND CONCLUSIONS

A principal objective of this thesis is to determine whether the natural gamma-ray spectrum can be used as a means of detecting variations in effective atomic numbers (Z_{eff}); thereby, enabling the identification of mineralised zones without the need to use radioisotopes to illuminate the rock formations. From a fundamental physics point of view the ratio of high energy (Compton scattering dominant) to low energy (Photoelectric scattering dominant) parts of the gamma spectrum should be a reliable indicator for variation in Z_{eff} regardless of whether the source is natural or not. Such a measurement, labelled the Heavy Mineral Indicator (HMI), is independent of the density of the material as both the Photoelectric and Compton scattering mechanisms are similarly dependent upon density. Simulations with GEANT4 and laboratory measurements of samples have confirmed that this HMI ratio corresponds well with changes in Z_{eff} with a natural radioactive source (potassium) distributed evenly through the medium. Previous work in measuring effective Z in borehole logging has only looked at spectral-gamma-gamma logging with a radioisotope or nuclear generator within the tool to irradiate the rock formation. No other studies have postulated or tested the use of natural radioactivity as the means to measure Z_{eff}.

A serious practical limitation of implementing HMI is the number of errors due to variations in spectral counting statistics. This is the main challenge of using the natural gamma-ray spectrum. Some simple modelling shows that a spectrum must be comprised of at least 20,000 gamma-ray total counts per spectrum to provide enough counting statistics to be acceptable for the HMI measure to usefully separate the natural variations in Z_{eff}. Unfortunately, experiments at the Brukunga test site and the analysis of field data from a spectral gamma tool used in the Geoscience Australia drilling initiative demonstrate that typical wireline logging speeds have poor counting statistics for natural gamma-ray spectra analysis. Either the spatial resolution suffers as many tens of metres of data must be averaged, or the variations due to statistical fluctuations swamp the changes in Z_{eff} . This thesis concludes that the practical application of HMI is best realised in a logging-while-drilling application using a platform such as Auto-Shuttle (developed for diamond drilling by the Deep Exploration Technology Commonwealth Research Centre). Typical diamond

drilling speeds are sufficiently slow, at 0.2-0.5m/min, so that a high quality spectrum with acceptable counting errors is produced.

With the aid of computer simulations and lab/field data it was found that the optimal choice for energy windows in the HMI method is between 50 and 500 keV. The low energy region is generally best in the range of 50 keV to 200 keV. Regions lower than 50 keV are mostly noise contaminated and overly prone to attenuation from drilling case/muds/rods. The high-energy windows are best sampled from 250 keV to 500 keV, where peaks from isotopes/daughter products of U and Th decay are not present. Another practical consideration in the context of logging-while-drilling for the HMI measurement is the "steel effect", where the nearby presence of the drill-string rods biases estimates of Z_{eff} to higher than actual levels resulting in less sensitivity. Performing the measurements inside the drill rods does attenuate the lower energy gamma rays (below 50 keV in particular) and interferes with the measurement of the surrounding rock formations. However, drill rod steel with 5 mm or less thickness does not influence the measurements in the 80-500 keV energy range sufficiently that it cannot be corrected. As most common diamond drill rods are less than 5 mm thick the idea of measuring HMI through the drill rods is still feasible.

At the Brukunga test site experiments were performed with wireline tools simulating a LWD tool, and a prototype spectral gamma LWD tool in two holes. These tests demonstrate that pyrite-rich zones can be delineated from the host rocks by analysing the HMI derived from the natural gamma-ray spectrum. Additionally, in both holes the match between Fe assay data and HMI logs demonstrates clearly the link between the HMI measurement and Fe content. Calculations of Z_{eff} from the assay data also confirm that in many cases HMI is highly correlated with iron content. Such success was not achieved on the normally logged (via wireline) spectral gamma data in the Geoscience Australia logging program (in Victoria, Australia). Confirming that typical wireline logging speeds cannot provide sufficient counting statistics for quantitative analysis of the natural gamma-ray spectrum. Demonstrating the use of the natural gamma spectrum as a direct indicator of non-radioactive elemental abundance of iron is novel, and is a first for mineral exploration.

Although the main focus of this research is the use of the natural gamma-ray spectrum, it is still worthwhile looking at the wider application of the HMI method on spectra measured with an isotopic radioactive source. A possible key application is relating HMI to iron contents, thus an iron ore environment was used to test such ideas. Tests of the HMI method

on four wireline logs, from two boreholes, in iron ore deposits in the Pilbara demonstrated a means to measure iron content much quicker than a lab assay. The gamma-ray spectra were collected with a prototype litho-density tool deployed via wireline. The analysis of the litho-density tool data showed that HMI correlates well with-iron rich zones and confirmed that HMI may be used as a grade control tool. Again the poor results of HMI measures on the spectra recorded with a wireline tool without an isotopic source in the same borehole provided another example of the necessity for long residence times for HMI measurements with natural radioactivity.

The application of the HMI technique was trialled on a low-level airborne radiometric spectrum from the Elashgin area in Western Australia. This data set tested the ability to identify areas with a higher atomic number due to iron minerals, such as ferricretes and iron-rich laterite materials. The good correlation with other interpretations (based upon conventional K, U, Th and ground surveys) of this well studied data set demonstrates the utility of applying the HMI method for remote sensing; since narrow features such as drainage channels are clearly identified and well resolved. This appears to be the first use of natural gamma rays scattered within the earth as a means of identifying changes in Z_{eff}, and HMI as a proxy for near-surface changes in elemental iron concentrations. This thesis demonstrates the first use of natural radiometrics to infer Fe along with traditional K, U, Th distributions from airborne radiometrics; perhaps heralding a new era in radiometrics analysis, and the reprocessing of legacy data for new insights.

This thesis is largely dedicated to enhancing the application of natural gamma-ray spectroscopy. LWD can save a substantial amount of time and expense compared to normal core logging. The results from the research can be utilised to increase efficiency in spectral analysis and provide a scope for more frequent application in the mineral industry. In the next decade, we might finally see the universal recognition of LWD measurements by the mining industry just as it has been recognised for years in the oil industry. The developments from this research will open new areas in exploration regarding the estimation of rock properties in real-time and the improvements of geological knowledge from downhole to the surface.

1.1 RECOMMENDATIONS FOR FURTHER STUDIES

This study demonstrates the benefits of using different parts of the natural gamma-ray spectrum to collect more information about rock formations. We also conducted some brief research of using the ratio of Compton region of the spectrum normalised by the potassium peak to indicate density variations using natural radioactivity. This work is presented in Appendix A. Unfortunately this initial work was inconclusive. The major drawback of this method is the sensitivity to geometry or in-homogeneity of radioisotopes in the medium. In the borehole environment, the radiation leaving a volume equilibrates with the radiation coming in to the borehole. This is a downside in logging applications, as the spectrum is largely the same shape regardless of density. However, the lack of radioactive material in air and the distinct density difference at the boundary between air and the earth's surface means that this method might be viable in ground or airborne measurements. Airborne radiometric measurement appears to be a good application for this type of Compton to peak normalisation analysis, since the gamma rays detected are within 30 cm of the earth's surface. Another restriction is less sensitivity for this technique when it is applied to dense materials, such as a density greater than 4 g/cm^3. However, soils rarely have a density greater than 2.5g/cc. Thus, there is an opportunity to map soil density variations quantitatively by applying this new approach to analysing the natural gamma-ray spectrum. We strongly recommend that this method be investigated further.

REFERENCES

Agostinelli, S., et al., 2003, "GEANT4—a simulation toolkit.". Nuclear Instruments and Methods in Physics Research Section A: Accelerators, Spectrometers, Detectors and Associated Equipment, **506**(3), 250-303.

Ahrens, T. J., 1995, Global Earth Physics: A Handbook of Physical Constants. American Geophysical Union.

Airo, M. L., 2015, Geophysical signatures of mineral deposit types in Finland. Geological Survey of Finland, **58**, 22.

AMPTEK, MCA-8000D Digital Multichannel Analyzer, 2017, http://amptek.com/products/mca-8000d-digital-multichannel-analyzer/, accessed 26 January 2017.

Apostolakis, J., S. Giani, L. Urban, M. Maire, A. V. Bagulya, and V. M. Grichine, 2000, An implementation of ionisation energy loss in very thin absorbers for the GEANT4 simulation package. Nuclear Instruments and Methods in Physics Research Section A: Accelerators, Spectrometers, Detectors and Associated Equipment, **453**(3), 597-605. doi: http://dx.doi.org/10.1016/S0168-9002(00)00457-5.

Beattie, N., 2009, Monitoring-While Drilling for open-pit mining in hard rock environment: An Investigation of Pattern Recognition Techniques Applied to Rock Identification. Thesis of Queen's University, Kingston, Canada.

Beckett, K. A., 2007, Multispectral Analysis of High Spatial Resolution 256-channel Radiometrics for Soil and Regolith Mapping. Thesis of Curtin University of Technology, Perth, Australia.

Bertozzi, W., D. V. Ellis, and J. S. Wahl, 1981, The physical foundation of formation lithology logging with gamma rays. GEOPHYSICS, **46**(10), 1439-1455.

Bevington, P. R., and D. K. Robinson., 2003, Data reduction and error analysis for the physical sciences. Third Edition. McGraw-Hill. 338 p.

Birks, J. B., 1964, The Theory and Practice of Scintillation Counting. International Series of Monographs in Electronics and Instrumentation, **27**, Pergamon Press. 684 p.

Blum, P., A. Rabaute, P. Gaudon, and J. Allan, 1997, Analysis of natural gamma-ray spectra obtained from sediment cores with the shipboard scintillation detector of the Ocean Drilling Program: Example from Leg 156. Proceedings of the Ocean Drilling Program, **156**, 183-195.

Borsaru, M., R. J. Holmes, and P. J. Mathew, 1983, Bulk analysis using nuclear techniques. The International Journal of Applied Radiation and Isotopes, **34**(1), 397-405.

Century wireline services, 2015, Spectral Gamma Logging Tool, http://www.century-geo.com/7201.html, accessed 24 March 2017.

Century wireline services, 2009, 7201 Users Guide, http://www.centurywirelineservices.com/ug7201.html, accessed 19 April 2017.

Chin, R. J., 1986, 1:250:000 geological series-explanatory notes, Kellerberrin, Western Australia. Geological Survey of Western Australia.

Commander, P., N. Schoknecht, B. Verboom, and P. Caccetta, 2001, The Geology, Physiography and Soils of the Wheatbelt Valleys. Proceedings of the Wheatbelt Valleys Conference, Perth, Australia.

Collett, T. S., M. W. Lee, M. V. Zyrianova, S. A. Mrozewski, G. Guerin, A. E. Cook, and D. S. Goldberg, 2012, Gulf of Mexico Gas Hydrate Joint Industry Project Leg II logging-while-drilling data acquisition and analysis. Marine and Petroleum Geology, **34**(1), 41-61.

Cook, S., R. Corner, P. Groves, and G. Grealish, 1996, Use of airborne gamma radiometric data for soil mapping. Soil Research, **34**(1), 183-194.

Copco, A., 2015, Professional Diamond Driller's Handbook, Practical Guide. Atlas Copco Secoroc AB. 52 p.

Crain, 2014, CRAIN'S PETROPHYSICAL HANDBOOK, http://www.spec2000.net/08-lwd.htm, accessed 15 December 2016.

Crawford, A. J., R. R. Keays, 1978, Cambrian greenstone belts in Victoria: Marginal sea-crust slices in the Lachlan Fold Belt of southeastern Australia. Earth and Planetary Science Letters, **41**(2), 197-208.

Crouthamel, C. E., F. Adams, and R. Dams, 1970a, Applied Gamma-Ray Spectrometry. International Series of Monographs on Analtical Chemistry, Pergamon Press, 772 p.

Crouthamel, C. E., F. Adams, and R. Dams. 1970b, Chapter 2: Scintilation Detectors. In: Applied Gamma-Ray Spectrometry. International Series of Monographs on Analtical Chemistry, Pergamon Press, 31-68.

Czubek, J. A., 1979, Modern trends in mining geophysics and nuclear borehole logging methods for mineral exploration. In: Geophysics and Geochemistry in the Search for Metallic Ores: Proceedings of Exploration 77 an International Symposium Held in Ottawa, Canada in October, 1977. Geological Survey of Canada.

Czubek, J. A., 1966, Physical possibilities of gamma-gamma logging. In: Radioisotope Instruments in Industry and Geophysics. IAEA, Vienna, **2**, 249-275.

Dickson, B. L., and M. K. Scott, 1997, Interpretation of aerial gamma-ray surveys - adding the geochemical factors. AGSO journal of Australian geology & geophysics, **17**, 187-199.

Dickson, B., and G. Taylor, 1999, Maximum noise fraction method reveals detail in aerial gamma-ray surveys. Exploration and Mining Research News, **11**, 8-10.

DMP Geoview, 2016, Government of Western Australia, Department of Mines and Petroleum, https://geoview.dmp.wa.gov.au/GeoViews/?Viewer=GeoVIEW, Data set accessed 15 December 2016.

Dodd P. H., and D. H. Eschliman, 1972, Borehole logging techniques for uranium exploration and evaluation. Uranium Prospecting Handbook, Bowie, S.H.U., Davis, M., and Ostle, D., eds., Inst. Min. Metall., London, 244-276.

Duval, J. S., B. Cook., and A. J. S. Adams, 1971, Circle of investigation of an airborne gamma-ray spectrometer. Journal of Geophysical Research, **76**, 8466–8470.

Ellis, D., C. Flaum, E. Marienbach, C. Roulet, and B. Seeman, 1985, Litho-Density Tool Calibration. Society of Petroleum Engineers Journal, **25**(4), 515-520.

Ellis, D. V., 1987, Nuclear Logging Techniques. In: Petroleum Engineering Handbook, Howard B. Bradley, Chap. 50, Richardson, Texas, Society of Petroleum Engineers. 38 p.

Ellis, D. V., 1988, Gamma ray scattering measurements for density and lithology determination. IEEE Transactions on Nuclear Science, **35**(5).

Ellis, D. V., and J. M. Singer, 2007, Well Logging for Earth Scientists. Springer Netherlands, doi: 10.1007/978-1-4020-4602-5.

Evans, R. D., 1955, The Atomic Nucleus. Tata McGraw Hill Publishing Company Limited. 1002 p.

Gardner, J. S., and J. L. Dumanoir, 1980, Litho-Density Log Interpretation. In: SPWLA 21st Annual Logging Symposium. Lafayette, Louisiana. Society of Petrophysicists and Well-Log Analysts, doi: SPWLA-1980-N.

Garrels, R. M., and F. T. Mackenzie, 1972, Evolution of sedimentary rocks. WW Norton & Co; 1st edition.

Gearhart, D. A., and G. L. Mathis, 1986, Development Of A Spectral Litho-Density Logging Tool By Use Of Empirical Methods. Society of Petrophysicists and Well-Log Analysts. 18 p.

George, R. J., 1969, Sulphide-silicate reactions during metamorphism of the Nairne pyrite deposit. Proc. Australasian Inst. Mining Me, **230**, 1-7.

Glenn, W.E., and G. W. Hohmann, 1981, Well logging and borehole geophysics in minearal exploration. In: Skinner, B. J., Seventy-Fifth Anniversary Volume, Society of Economic Geologists.

Glenn, W.E., and P.H. Nelson, 1979, Borehole logging techniques applied to base metal ore deposits. In: Hood, P. J., Geophysics and Geochemistry in the Search for Metallic Ores, Geological Survey of Canada, Economic Geology Report 31, 273-294.

Goldberg, D., A. Meltser., and ODP Leg 191 Scientific party, 2001, High Vertical Resolution Spectral Gamma Ray Logging: A New Tool Development And Field Test Results. Society of Petrophysics and Well Log Analysts 42nd Annual Logging Symposium, Houston, USA.

GOWell Petroleum Equipment , 2016, Litho Density Logging Tool (LDLT), http://www.gowellpetro.com/product/litho-density-logging-tool-ldlt.html. Accessed 10 Febarary 2017

Grabmaier, B. C., 1984, Crystal Scintillators. IEEE Transactions on Nuclear Science, **31**(1), 372-376.

Grasty, R. L., 1979, Gamma ray spectrometric methods in uranium exploration - theory and operational procedures; In: Geophysics and Geochemistry Economic Geology in the Search for Metallic Ores, Geological Survey of Canada, Economic Geology Report 31, 147-161.

Grasty, R. L., and B.R.S. Minty, 1995, A guide to the technical specifications for airborne gamma-ray surveys. Department of Primary Industries and Energy, Australian Geological Survey Organisation.

Greenwood, A., A. Kepic, A. Podolska, C. Dupuis, S. Gordon, 2015, Logging during diamond drilling?: Autonomous logging integrated into the Bottom Hole Assembly. ASEG Extended Abstracts, 2015(1), 1-4.

Hamamatsu Photonics, 2007, Photomultiplier Tubes: Basics and Applications. 3rd Edition.

Hart, P. J., 1969, The Earth's Crust and Upper Mantle: Structure, Dynamic Processes, and Their Relation to Deep-seated Geological Phenomena. In: Hart, J., American Geophysical Union, Washington D.C., 736 p.

Hassan, M. H., A. Combaz, 1976, Fundamentals Of The Differential Gamma Ray Log - Interpretation Technique. Society of Petrophysicists and Well-Log Analysts 17th Annual Symposium. Paper H, 1-18.

Herrmann, L., U. Shuler, W. Rangubpit, P. Erbe, A. Surinkum, M. Zarei, K. Stahr, and R. Gilkes, 2010, The potential of gamma-ray spectrometry for soil mapping. Proceedings of the 19th World Congress of Soil Science, Soil solutions for a changing world. 1-6 August 2010, Brisbane, Australia.

Hillis, R. R., D. Giles, S. E. van der Wielen, A. Baensch, J. C. Cleverly, A. Fabris, S. W. Halley, B. D. Harris, S. M. Hill, P. A. Kanck, A. Kepic, S. P. Soe, G. Stewart, and Y. Uvarova, 2014, Coiled tube drilling and real-time sensing-enabling prospecting drilling in the 21st Century Society of Economic Geologists, Special Publication **18**, 243–259.

Holmes, K., T. Griffin, and N. Odgers, 2014, Soil and Landscape Grid Digital Soil Property Maps for Western Australia (3" resolution). Commonwealth Scientific and Industrial Research Organisation (CSIRO). doi: https://doi.org/10.4225/08/5aaf364c54ccf.

Hooshyari, I., A. Kepic, M, Carson, 2016, Gamma-ray spectra analysis for Lithology investigation. Near Surface Geoscience 2016 - First Conference on Geophysics for Mineral Exploration and Mining, 4-8 September 2016. Barcelona, Spain: EAGE.

Hooshyari, I., A. Kepic, A. Greenwood, A. Podolska, 2015, A New Logging While Drilling Approach for Natural Gamma Spectroscopy with Diamond Drilling. Joint assembly, AGU-GAC-MAC-CGU, 3-7May 2015, Montreal, Canada

Hooshyari-Far, I., A. Kepic, and A. Podolska. 2015. A new approach provides opportunities for spectral gamma analysis in boreholes for mineral exploration. ASEG Extended Abstracts 2015: 24th International Geophysical Conference and Exhibition. 1-4 February 2015, Perth, Australia

Hoyer, W., and G. Lock, 1971, Natural Gamma-ray Spectral Logging. Society of Petrophysicists and Well-Log Analysts, **12**(5), 7 p.

Hurtado, S., M. García-León, and R. García-Tenorio, 2004, GEANT4 code for simulation of a germanium gamma-ray detector and its application to efficiency calibration. Nuclear Instruments and Methods in Physics Research Section A: Accelerators, Spectrometers, Detectors and Associated Equipment, **518**(3), 764-774.

Jasinski, S. M., 2011, Mineral resource of the month: potash. Earth, **56**(10), 25-25.

Jones, M., T. Cudahy, M. Thomas, and R. Hewson, 2010, Airborne and ground-based spectral surveys map surface minerals and chemistries near Duchess, Queensland. Proceedings of the 19th World Congress of Soil Science, Soil Solutions for a Changing World, 1-6 August 2010, Brisbane, Australia.

Kepic, A., A. Podolska, I. Hooshari-Far, and A. Greenwood, 2015, New scintillators and method for spectral gamma logging in slim boreholes. Near-Surface Asia Pacific Conference, Waikoloa, Hawaii, 7-10 July 2015. 220-223.

Kepic, A., A. Podolska, and A. Greenwood, 2014, Technical Report, Project 2-2: Sensors for rapid down-hole rock characterisation, Sonde testing with RC Drill Rig, March 2014: Deep Exploration Technology CRC.

Killeen, P. G., 1997, Borehole geophysics: Exploration the third dimension: Gubins, A. G., Proceedings of Exploration 97: Fourth Decennial International Conference on Mineral Exploration, 31-42.

Killeen, P. G., 1997, Nuclear techniques for ore grade estimation. In: Gubins, A. G., Proceedings of Exploration 97: Fourth Decennial International Conference on Mineral Exploration, 677–684.

Killeen, P. G., and B. E. Elliott, 1997, Surveying The Path Of Boreholes: A Review Of Orientation Methods And Experience. In: Gubins, A. G., Proceedings of Exploration 97: Fourth Decennial International Conference on Mineral Exploration, 709–712.

Killeen, P. G., C. J. Mwenifumbo, B. E. Elliott, K. A. Pflug, L. D.Schock, and G. R. Bernius, 1996, Borehole Geophysics in mineral exploration. Geological Survey of Canada

Killeen, P. G., L. D. Schock, and B. E. Elliott, 1989, A slim hole assaying technique for base metals and heavy elements based on spectral gamma-gamma logging. In: Proceedings of the 3rd Int'l. Symposium on Borehole Geophysics for Minerals and Geotechnical Logging, 2-5 Oct., 1989, Las Vegas, Nevada, 435-454.

Kitzig, M. C., A. Kepic, and D. T. Kieu, 2016, Testing cluster analysis on combined petrophysical and geochemical data for rock mass classification. Exploration Geophysics, **48**(3), 344-352.

Knoll, G. F., 2010, Radiation Detection and Measurement. John Wiley & Sons. 816 p.

LaGanza, R. F., 1959, Pyrite investigations at Nairne, South Australia. Economic Geology, **54**(5), 895-902.

Li, Y., and D. W. Oldenburg, 1998, 3-D inversion of gravity data. GEOPHYSICS, **63**(1), 109-119.

Boart Longyear, 2009, Global product catalogue - Coring rods and casing.

Loy, J., 2007, Code of Practice: Security of Radioactive Sources. Radiation Protection Series Publication No. **11**. Australian Radiation Protection and Nuclear Safety Agency.

Marchuk, S., and B. Ostendorf., 2009, Relationship between soil properties and airborne gamma-radiometric data. Proceedings of the Surveying & Spatial Sciences Institute Biennial International Conference (SSC2009).

Marett, G. C., P. Souhaite, J. Suau, 1976, Shaly sand evaluation using gamma ray spectrometry, applied to the North Sea Jurassic. Proceedings of the 17th Annual Logging Symposium, Society of Petrophysicists and Well-Log Analysts.

Materials World magazine, 2009, Logging While Drilling in Mining, http://www.iom3.org/materials-world-magazine/news/2009/feb/01/logging-while-drilling-mining. Accessed 15 December 2017.

Mathis, G. L., C. W. Tittle, D. R. Rutledge, R. Mayer, and W. E. Ferguson, 1984, A Spectral Gamma Ray (SGR) Tool. In: SPWLA 25th Annual Logging Symposium, 10-13 June, New Orleans, Louisiana. Society of Petrophysicists and Well-Log Analysts. 21 p.

Maučec, M., P. H. G. M. Hendriks, J. Limburg, and R. J. de Meijer, 2009, Determination of correction factors for borehole natural gamma-ray measurements by Monte Carlo simulations. Nuclear Instruments and Methods in Physics Research Section A: Accelerators, Spectrometers, Detectors and Associated Equipment, **609**(2–3), 194-204.

McMonnies, B., and V. Gerrie, 2007, Ground Geophysics and Borehole Logging – A Decade of Improvements, Improvements. Proceedings of Exploration 07: Fifth Decennial International Conference on Mineral Exploration, 39-49.

Mount Sopris Instruments, 2017, QL40-SGR Spectral Gamma - Geophysical Well Logging Equipment, http://mountsopris.com/items/ql40-sgr-spectral-gamma/. Accessed 22 March 2017.

McNally, G. H., 2002, Soil and Rock Construction Materials. Taylor & Francis e-Library, 2003.

Minty, B. R. S., 1992, Airborne gamma-ray spectrometric background estimation using full spectrum analysis. GEOPHYSICS, **57**(2), 279-287.

Minty, B. R. S., P. McFadden, and B. L. N. Kennett, 1998, Multichannel processing for airborne gamma-ray spectrometry. GEOPHYSICS, **63**(6), 1971-1985.

Mutton, A. J., 1994, Application of Downhole Geophysical Logging to Lithological Correlation and Resource Assessment in Base Metal Deposits. Symposium on the Application of Borehole Logging to Mineral Exploration and Mining, Perth 1994. Australian Mineral Industries Research Association.

Muty, R. C., 1965, Effective Atomic Numbers of Heterogeneous Materials. Nature, **207**, 398-399.

Odgers, N. P., A. B. McBratney, and B. Minasny, 2015, Digital soil property mapping and uncertainty estimation using soil class probability rasters. Geoderma, **237–238**, 190-198.

Odgers, N. P., W. Sun, A. B. McBratney, B. Minasny, and D. Clifford, 2014, Disaggregating and harmonising soil map units through resampled classification trees. Geoderma, **214–215**, 91-100.

Portal Geosience, 2016, Geophysical Archive Data Delivery System, http://www.geoscience.gov.au/cgibin/mapserv?map=/nas/web/ops/prod/apps/mapserver/gadds/wms_map/gadds.map&mode=browse. Dataset accessed on 20 December 2016.

Pracilio, G., 2007, The utilisation of gamma ray spectrometry, a soil mapping technology, to improve dryland crop production. Thesis of the University of Western Australia.

Rapach, T. A., and M. A. Pelcher, 2008, Gamma ray spectroscopy. Department of Physics and Astronomy, University of Rochester, Rochester, NY, 14627.

Rawlins, B. G., R. M. Lark, and R. Webster, 2007, Understanding airborne radiometric survey signals across part of eastern England. Earth Surface Processes and Landforms, **32**(10), 1503-1515.

Reilly, D., N. Ensslin, H. Smith, and S. Kreiner, 1991, Passive Nondestructive Assay of Nuclear Materials. United States Nuclear Regulatory Comission.

Richgro Garden Products, 2013, Safety data sheet, product name: Sulfate of Potash.

Rider, M. H., and M. Kennedy, 2004, The Geological Interpretation of Well Logs. Rider-French Consulting Ltd. 432 p.

Segrè, E., 1977, Nuclei and particles: an introduction to nuclear and subnuclear physics. W. A. Benjamin. 966 p.

Serra, O., 1984, Fundamentals of Well-log Interpretation: 1. The acquisition of logging data. Elsevier Science Publishing.

Serra, O., J. Baldwin, and J. Quirein, 1980, Theory, Interpretation, And Practical Applicatons Of Natural Gamma Ray Spectroscopy. Society of Petrophysicists and Well-Log Analysts. 30 p.

Skinner, B. J., 1958, The geology and metamorphism of the Nairne pyritic formation, a sedimentary sulfide deposit in South Australia. Economic Geology, **53**(5), 546-562.

Skladzien, P. B., T. Barton, A. Schofield, and M. A. McLean, 2016, Regional geology and mineral systems of the Stavely region, western Victoria: Data release 4 – drill core rock property measurements. Record 2016/14. Geoscience Australia, Canberra.

Smith, H. D. Jr, A. Robins, D. M. Arnold, L. L. Gadeken, and J. G. Deaton, 1983, A Multi-Function Compensated Spectral Natural Gamma Ray Logging System. Proceedings of the 58th Annual Technical Conference and Exhibitio, San Francisco, USA. Society of Petroleum Engineers of AIME.

Stoller, C., H. L. Darling, T. DasGupta, B. M. Jorion, R. A. Perchonok, O. G. Philip, and N. I. Wijeyesekera, 1997, Density Logging in Slim Holes With a Novel Array Density Tool. Society of Petroleum Engineers. 10 p.

Taylor, M. J., K. Smettem, G. Pracilio, and W. Verboom, 2002, Relationships between soil properties and high-resolution radiometrics, central eastern Wheatbelt, Western Australia. Exploration Geophysics, **33**(2), 95-102.

Telford, W. M., L. P. Geldart, and R. E. Sheriff, 1990, Applied Geophysics. Cambridge University Press. 770 p.

Theys, P. P., 1999, Log Data Acquisition and Quality Control. Editions Technip. 453 p.

UTS Geophysics, 2001, Logistics Report: Detailed Airborne Magnetic, Radiometric and Digital Elevation Survey for the Elashgin Catchment. Universal Tracking Systems Geophysical Surveys, Job #A418.

Uvarova, Y., J. Cleverley, A. Baensch, D. Lawie, M. Carey, F. Best, and F. Blaine, 2013, Lab-at-Rig® for Mineral Exploration. http://detcrc.com.au/programs/program-3/project-3-2/. Accessed on 10 December 2016.

Verboom, W. H., and J. S. Pate, 2003, Relationships between cluster root-bearing taxa and laterite across landscapes in southwest Western Australia: an approach using airborne radiometric and digital elevation models. Plant and Soil, **248**(1), 321-333.

Watson, C. C., 1983, Numerical Simulation Of The Litho-Density Tool Lithology Response. Society of Petroleum Engineers. 12 p.

Wilford, J., and B. Minty, 2006, The Use of Airborne Gamma-ray Imagery for Mapping Soils and Understanding Landscape Processes. In: A. B. McBratney, P. Lagacherie, and M. Voltz, Developments in Soil Science. Elsevier, 207-610.

Wilford, J., L. Worrall, and B. Minty, 2009, Radiometric Map of Australia provides new insights into uranium prospectivity. AUSGEO News **95**. Geoscience Australia.

Witherly, K., 2012, The evolution of minerals exploration over 60 years and the imperative to explore undercover. The Leading Edge, **31**, 292–295.

Wong, M., Y. Oliver, and M. Robertson, 2009, Gamma-radiometric assessment of soil depth across a landscape not measurable using electromagnetic surveys. Soil Science Society of America Journal, **73**(4), 1261-1267.

APPENDIX A: COMPTON TO PEAK RATIO - CPR

The common practise for estimating the density is applying a Gamma-Gamma density tool where a radioactive source is used to measure gamma rays. This method is not very favourable as the loss of radioactive source in a borehole imposes a heavy toll as regulations require that the radioactive source should be retrieved immediately and if the source is irretrievably lost, no further drilling is allowed in the vicinity of the source (Loy 2007). Therefore, developing a new means of determining a rock density using a natural gamma-ray spectrum is in high demand.

The method we investigated in this research is by using the different parts of a natural gamma-ray spectrum to estimate the rock density. The hypothesis is that the ratio of number of gamma rays, which are scattered by the Compton effect (energy ranging from 200 keV to 1000 keV), to those that directly deposit in a detector and form the primary peak in a spectrum, can be used as a measure to estimate density. The idea of applying the ratio of these parts of a spectrum (refer to Figure 1) as a measure of density originates from the following discussion:

From equation 1, we define intensity of non-scattered gamma rays approximately as:

$$I_p = I_0 e^{-\rho x}, \qquad (1)$$

where I_p is intensity of gamma rays that deposit directly into a detector, ρ is the density of a formation where gamma rays interact, x is an average length that gamma rays travel before reaching a detector and I_0 is the initial intensity. Since ^{40}K is a dominant natural radioactive source, we only considered the gamma rays peak at 1.46 MeV (the energy of the gamma ray associated with the decay of ^{40}K). The number of gamma rays that are scattered in the formation before registering in the detector is assumed to be proportional to the intensity of all the gamma rays except those near (or at) the peak regions.

$$I_c = \beta I_0 (1 - e^{-\rho x}), \qquad (2)$$

where β is a factor to scale the intensity to Compton scattered gamma rays that are registered into the detector. From the equation I_c is shown to be depended on a density as well. The ratio of I_c to I_p is thus given by:

$$\frac{I_c}{I_p} = \frac{\beta(1 - e^{-\rho x})}{e^{-\rho x}}. \quad (3)$$

We call this ratio the CPR (Compton scattered to peak ratio). As equation (3) shows, CPR depends on the density and is independent of the initial gamma ray intensity (I_0). Note that we did not take detector effects into account. From all gamma rays that are captured into a detector, only a fraction of them registered with their correct energy (the same energy that they entered into the detector crystal). Therefore the CPR can be modified as follows:

$$\frac{I_c}{I_p} = \frac{\beta(1 - e^{-\rho x}) + (1 - \mu)e^{-\rho x}}{\mu e^{-\rho x}}, \quad (4)$$

where μ is a factor to quantify the proportion of gamma rays that registered with their energy before any scattering in the crystal.

Equations 3 and 4 shows CPR increases with density. Parameters β and μ can be set empirically through laboratory calibrations. It is important to note that for the sake of mathematical simplicity we only consider equation (4) in one dimension. Moreover, other peaks such as uranium and thorium are not taken into account as K^{40} is the most abundant natural radioactive source. I plot CPR values for different density from 1.5 to 6 g/cc, assuming specific values for constant parameters in equation 4. CPR values changes exponentially with density variations when passing through a fixed distance in a medium (x= constant). Therefore, the hypothesis of using CPR for estimating density in a formation could be appropriate. In the following sections, we evaluate this theory with computer simulation along with laboratory measurements.

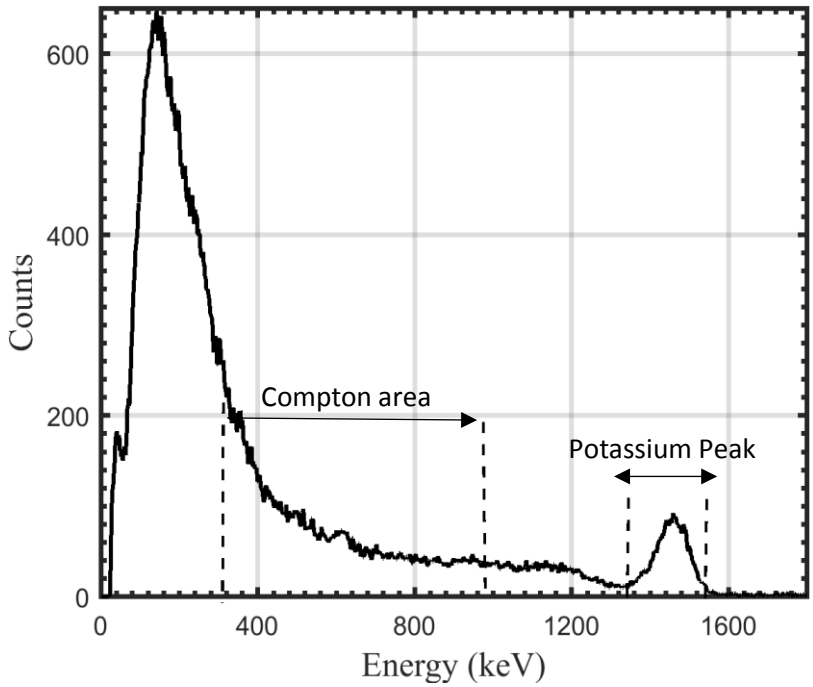

Figure 9: Laboratory spectrum showing how the Compton and peak energy windows are defined. K^{40} is typically the most abundent naturally occurring radioactive isotope and it is gamma rays from K^{40} decay which primarily scatter into the Compton region.

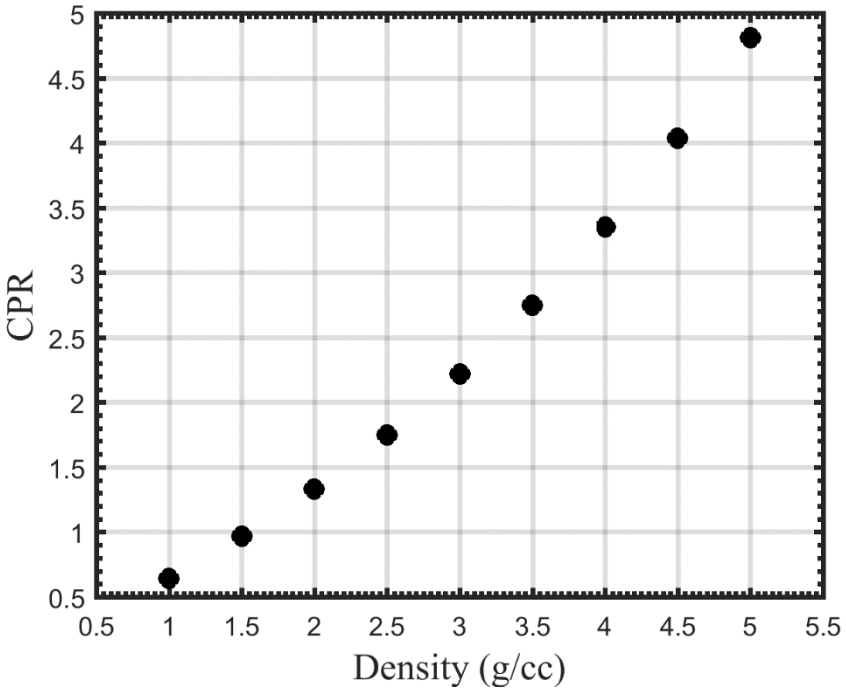

Figure 10: CPR for discrete density values using equation (4). The distance that gamma rays travel through the medium is considered constant, leaving density as the only variable. Increasing density leads to an increase in CPR.

COMPUTER SIMULATION OF CPR

In this section, we evaluate the CPR technique with Monte Carlo calculations using GEANT4 computer simulations (refer to chapter 3). We designed different models (scenarios) to simulate measurements under various borehole conditions. Each model consisted of a rock, a borehole, a detector and a source. The geometry of the models are the same as previously discussed (in section 3.1). In the following sections we present the CPR results from analyzing simulated spectra. The spectra are generated by using various scenarios such as changing rock density or borehole sizes.

Models with different density

The purpose of these series of simulations is to investigate whether CPR values can vary with rock density. Ten different models were simulated keeping the parameters (for instance borehole geometry, rock geometry, source and rock materials) are kept the same except for the rock density. The density ranges from 1.5 to 6 g/cm^3 with 0.5 g/cm^3 increment to cover a broad range of rock density range in the earth's crust (Telford et al. 1990). The sources of the gamma rays were ^{40}K that were uniformly distributed in the rock. To have a high-quality spectrum, each simulation modelled the interaction of 5x10^7 gamma rays in the rock. The rock materials were selected by the eight most abundant elements in the earth's crust which are as following, Oxygen 47.1%, Si 27.6%, Al 8.6%, Fe 5.6%, Ca 3.6%, Na2.8%, K 2.6% and Mg 2.1% (Garrel 1972). As a final step, we calculated CPR values for each spectrum resulting from the simulation. For this purpose, two energy windows were selected from the spectrum; the first one is from 250 to 500 keV (Compton window) and the second one is the peak window which in this case is centred around 1.46 MeV. CPR values and statistical errors are calculated and against the model density in Figure 11. We observe that increasing density follows by increase in CPR values as anticipated from equation 4 and results presented in figure 2. However, CPR plot from simulations has a logarithmic growth while CPR from the theory presented above shows an exponential growth. This show that an overly simple approach was adopted when deriving equation (4).

For density ranging from 1.5 to 4 g/cm^3, CPR values vary approximately linearly with the density. In this range, CPR values can detect 0.5 g/cm^3 density variations with 95 % confidence (2 sigmas). For density variantions greater than 4.5 g/cm^3, the resolution decreases to 66% (1 sigma). The decrease in resolution can be explained as gamma rays

scatter more in denser media. Hence, more gamma rays are registered in photoelectric region of the spectrum while the number of gamma rays in Compton and Peak regions do not change significantly. Since the majority of the rocks have density between 1.5 to 4.5 g/cm^3, it is possible to trace density variations using CPR technique.

In the next step, we simulated models that can be constructed under laboratory conditions. Therefore, these simulations can be readily reproduced in the laboratory and their results can be compared with our numerical simulations. For this series of modelling, we designed three models with the same geometry for the borehole, rock and detector as the previous section. However, the rock composition and density were different. The choice of rock materials were important since the same geometry parameters should provide us a good density contrast. We applied pumice which is a very light and porous volcanic rock to construct a model with a low density. Iron, which has high density and is easily obtainable, was chosen to increase the density in the model. We used concrete in all models to hold materials in place. Potash was also an ingredient in all model constructions to increase natural gamma-ray radioactivity. Potash in this case is di-potassium sulfate (96%) and potassium chloride (4%) which is normally available as a fertilizer, where the potassium is water soluble (Jasinski 2011; RICHGRO 2013).

The first model was composed of pumice 3.76%, concrete 54.39% and potash 41.84% which provided a density of 1.7 g/cm^3. For the second model we only used concrete 67.22% and potash 32.78% that yielded in density of 2.2 g/cm3 and the heaviest model comprised of iron 38.66%, concrete 35.56% and potash 25.78% with a density of 2.8 g/cm^3. The detector we used was a BGO crystal which is very dense making it a good choice for detecting more gamma rays.

We calculated CPR values for all three models and plotted them in Figure 12. Similar to the previous models, we can distinguish different densities based on CPR values. In these simulations, the density variations can be separated with higher confidence (more than 3 sigmas). Therefore, materials with less density can be detected with higher resolution. Note that CPR calculated from these simulations resulted in different values compare to the previous models, with the same density. For instance, CPR values for these models are from 2.2 to 2.9 while in the preceding section CPR values change within the range of 1.2 to 1.7. Differences in CPR error bounds are related to the statistical counts of gamma rays in the simulations. In the previous section, we used 5x10^7 gamma rays as sources while for the later simulation 10^6. Hence, counting statistics in the spectra change accordingly. We should

emphasise that CPR is only a ratio and is not a measure of any parameter such as a density. It is meaningful only in comparison with other CPR values measured in the same environment. In other words we cannot determine an absolute value for CPR and link it to density.

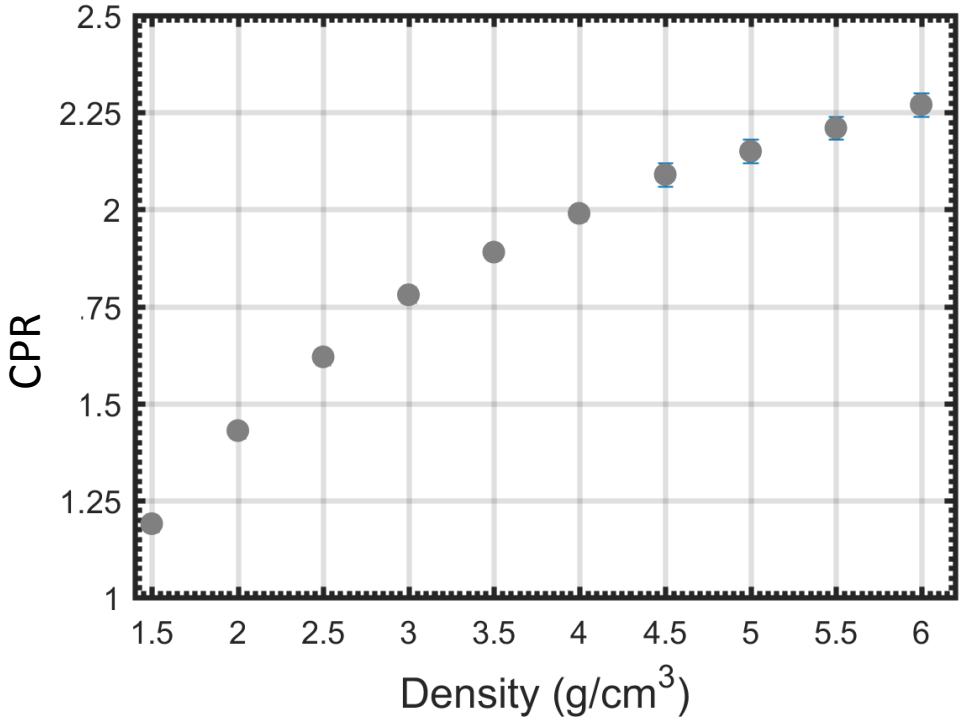

Figure 11: CPR values computed from models with different density. For each CPR value, the relative error is calculated and plotted but is only greater than the symbol size in the case of the larger densities. For density from 1.5 to 4.5 g/cm^3, CPRS values change significantly, but for densities more than 4.5 g/cm^3, CPR values do not vary significantly with density.

Simulated models with different density and geometry

In the previous section, simulated models were designed with the same geometry; the rock was a cylinder with radius of 15 cm and 21 cm height. In this section, we wanted to investigate the role of the geometry of media on the CPR technique and whether it imposes any significant limitation. For this purpose, all geometry parameters are the same as the previous models except for the radius of the "rock". We simulated five models with different rock radius that varies from 15 cm to 75 cm with 15 cm intervals. Figure 5 shows a schematic figure of these simulated models with different geometries. For each radius, for instance a rock with 15 cm in radius, we simulated models with density from 1.5 to 6 g/cm^3. All other model parameters such as the detector and the gamma ray sources remained the same and

similar to what is described in previous sections. Ultimately, 50 models with different density and different geometries were simulated. From each resulting spectrum, we calculated CPR value applying 250-500 keV energy range for the Compton window and used the standard window for the potassium peak. The results are plotted in figure 6.

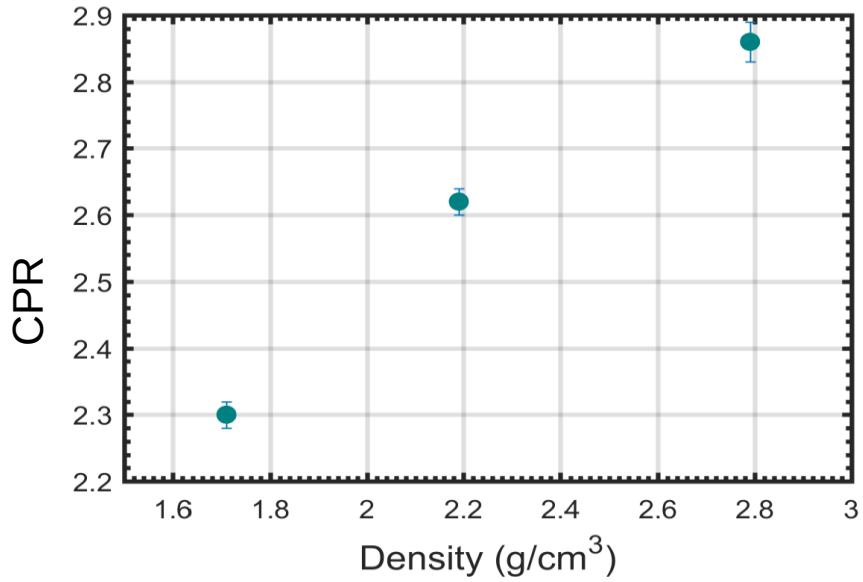

Figure 12: CPR values for models with 3 different density.

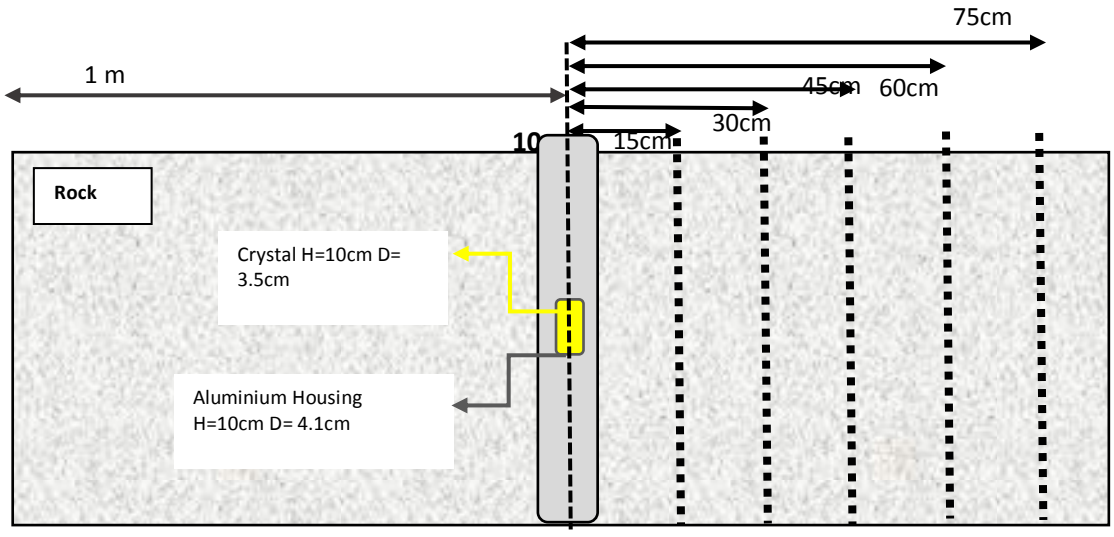

Figure 13: Schematic figure of models with different geometry.

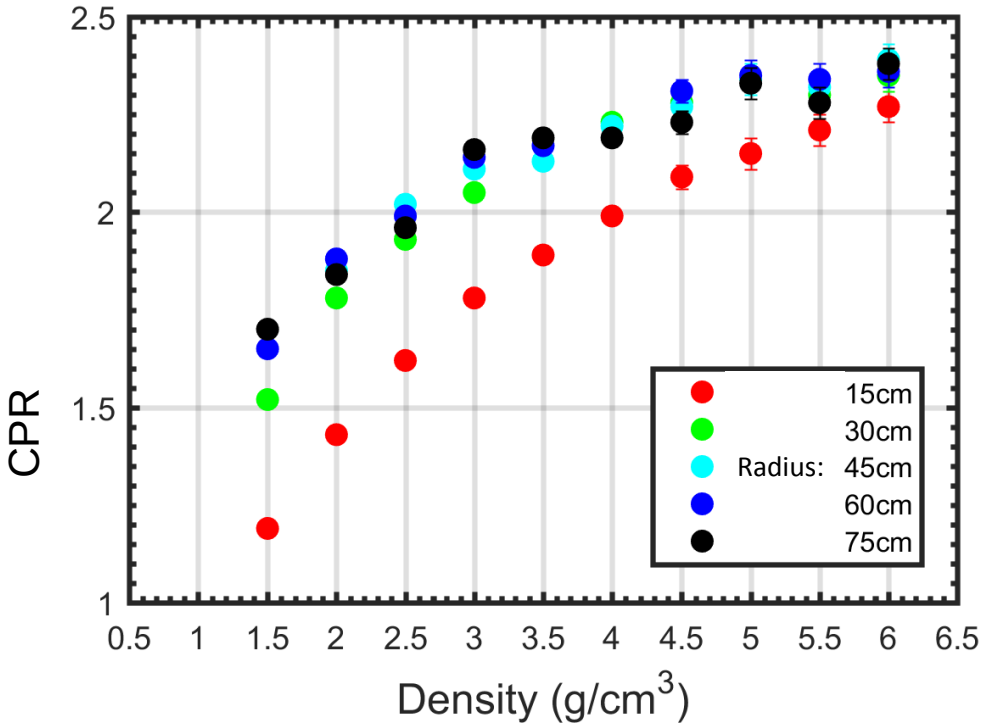

Figure 14: CPR values for different density calculated form models with different geometry.

The same logarithmically increasing trend of CPR with density can be followed for different geometries. For small density, less than 3 g/cm^3, it is still possible to detect density variations with CPR for all the radii. However, for density 3 g/cm^3 and greater CPR values do not change significantly with density. This result implies that CPR values are sensitive to radius of the rock when the radius is less than 30 cm. This can be explained with gamma ray attenuation which depends on distance that a gamma ray goes through as well as the medium density (equation 2-4). When gamma rays travel more than 40 cm in the media with different density, they lose their intensity in the same amount. In another word, after 40 cm the ratio of gamma ray intensity over its initial intensity, I/ I_0, is the same regardless of the medium density. Therefore, this technique is not applicable in gamma ray logging since gamma rays which deposited in the detector travel from infinite radius. In the next section, we conducted laboratory measurements for the models with small geometries, 15 cm in radius, to cross check the simulation results for the CPR technique.

LABORATORY EXPERIMENTS FOR CPR

Model constructor parameters

In this section, we carried out experimental measurements, on laboratory scale boreholes (LSB) equivalent to the simulated models. Gamma-ray spectra are measured and used in the CPR technique. Three LSB are constructed with concrete mixtures of iron and pumice to provide significant density variations. To provide homogeneous zones we mixed materials in separate containers and transferred them cautiously to our LBS. A plastic pipe was placed in the centre position of the LBS and detector used as in the experiments described in Chapter 3. Although we tried to create laboratory models to be very similar to the specifications of the simulated ones, the concrete elemental composition applied in experiments is not exactly the same as used in GEANT4 simulations. This is a result of imprecise information relating to industrial concrete as used in the laboratory. Since we assume density is the strongest factor in the CPR, slight difference in elemental composition should not have an impact on experimental results. The other experimental parameters are kept the same as determined in our simulations. We followed the same procedures explained for gamma-ray measurements in previous tests, refer to chapter 3.

Experimental results

As with the simulation models we chose an energy range from 250 keV to 500 keV for the Compton window and 1360 keV to 1560 keV for the peak window. After spectrum calibration, the numbers of gamma-ray counts under each window are integrated to compute the CPR ratio. We presented CPR from experimental data with their equal models in figure 7. The expected increment trend of CPR with density is detected. We also observe a satisfying linear correlation between CPR ratios and density of the LSBs (R^2= 0.94). For 30% increase in density, CPR values are separable with 2 sigma accuracy. This significant accuracy makes this technique a very useful tool to track density variation in formations.

CPR values from simulated data vs density are also plotted in figure 7 to have a better comparison with laboratory results. Laboratory results from CPR calculations follow the same trend as simulated results which is a confirmation to the computer simulations. Trend lines are 4 % differentiated with an offset similar to HMI experiments that we believe is due to the same reasons, detector affect. However, as we discussed in the previous section the

CPR technique suffers from some limitations, it is limited to the geometry of the medium, which makes it inapplicable under borehole conditions.

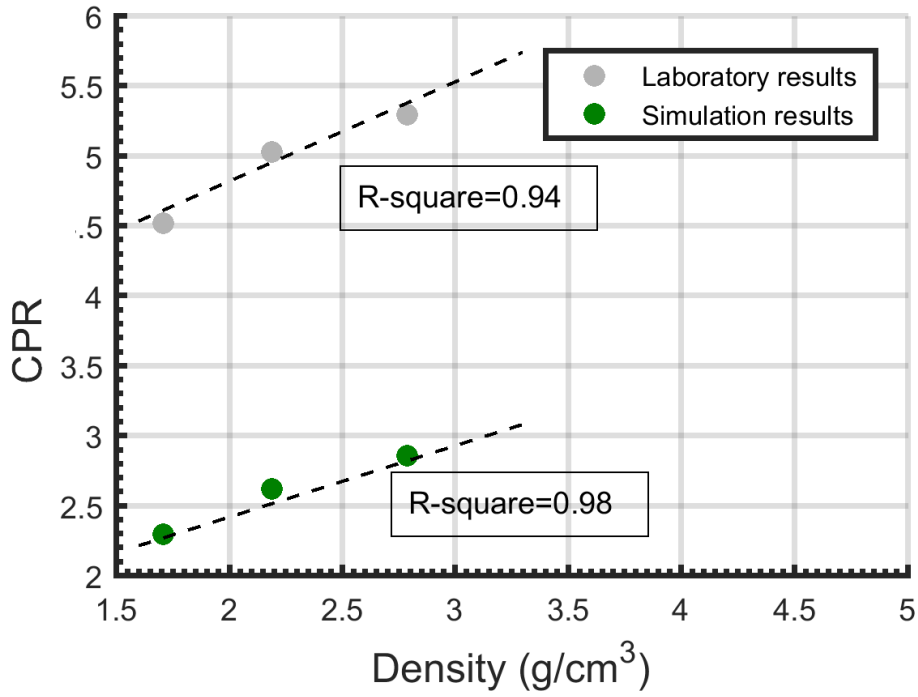

Figure 15 Results from CPR ratio values obtained from laboratory (grey symbols) and simulated (green symbols) data vs density of the medium. Trend lines are 4 % differentiated with an offset similar to HMI experiment which we believe is due to the same reasons (Hooshyari, Kepic, Greenwood, and Podolska 2015).

SIMULATIONS OF CPR FROM AIRBORNE DATA

The major drawback of CPR method is being sensitive to geometry of the medium. In another words if the formation, which gamma rays interact with, is more than 30 cm, CPR are no longer able to detect gamma ray variations. Although this is a downside in logging applications, the CPR technique can be applied in the other environments. Airborne radiometric measurements could be a good example for its application, since the gamma rays, which are being measured, come from the top 30 cm of the earth surface. The other restriction is the poor resolution of this technique when used for densities more than 4 g/cm^3. This should not be an issue again with airborne radiometric data, as soil density are less than 4 g/cm^3.

In this section, we present the result from simple simulation models of the airborne radiometric geometry to examine the potential of the CPR method to track density variations in this environment. The first model consists of a big sphere with a diameter of 2 m, considered as the earth. Gamma rays are uniformly distributed as a mono-energy source of ^{40}K, with a photopeak energy of 1.46 MeV (Fig. 8). For the sake of simplicity, we assumed that gamma rays leaving the surface of the sphere do not scatter back to the surface. The energy of gamma rays are recorded immediately after escaping from the surface. The density of the sphere has been changed from 1 to 4 g/cm^3. We designed the code to terminate when $7x10^4$ gamma rays have been registered in the detector. Thus all density spectra have the same counting statistics.

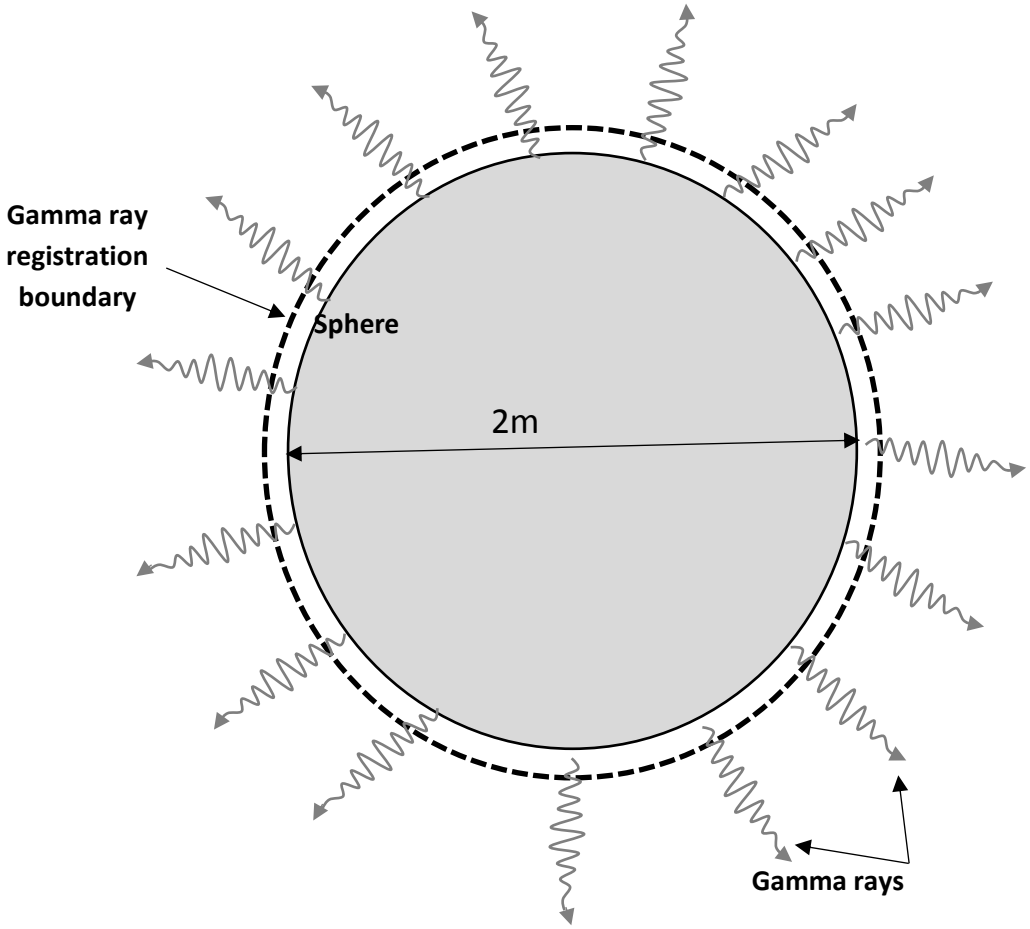

Figure 16: Schematic figure of the simulation sphere model; the dash line is the registering line.

CPR has been calculated using the Compton window from 300 to 1000 keV. The number of gamma rays in the normal K window is determined. We plotted CPR for different density values in figure 9. For density from 1 to 3 g/cm^3, the CPR is increasing with density

values in which it can separate density variations of 0.5 g/cm^3 with 1 sigma accuracy. However for density more than 3.5 g/cm^3 the CPR is not valid anymore, since gamma rays scattered more and contribute more to photoelectric region. Therefore, the numbers of gamma rays in the peak and Compton area decrease with the same ratio. It is important to note that soil density are in the range of 1.5 to maximum 3.5 g/cm^3. Hence, CPR values can be a good indicator of variations in soil density. The model that we simulated and studied was very simple with many assumptions such as ignoring the air effect and curvature effects.

As one further step, we modelled a condition which was slightly closer to the reality. The aim of this model was simulating a scenario where generated gamma rays can be easily detected by a crystal. It was a small and simplified scale of the airborne radiometric measurements. For this purpose, the model construction consisted of two paralleled discs which were separated by 50 cm.

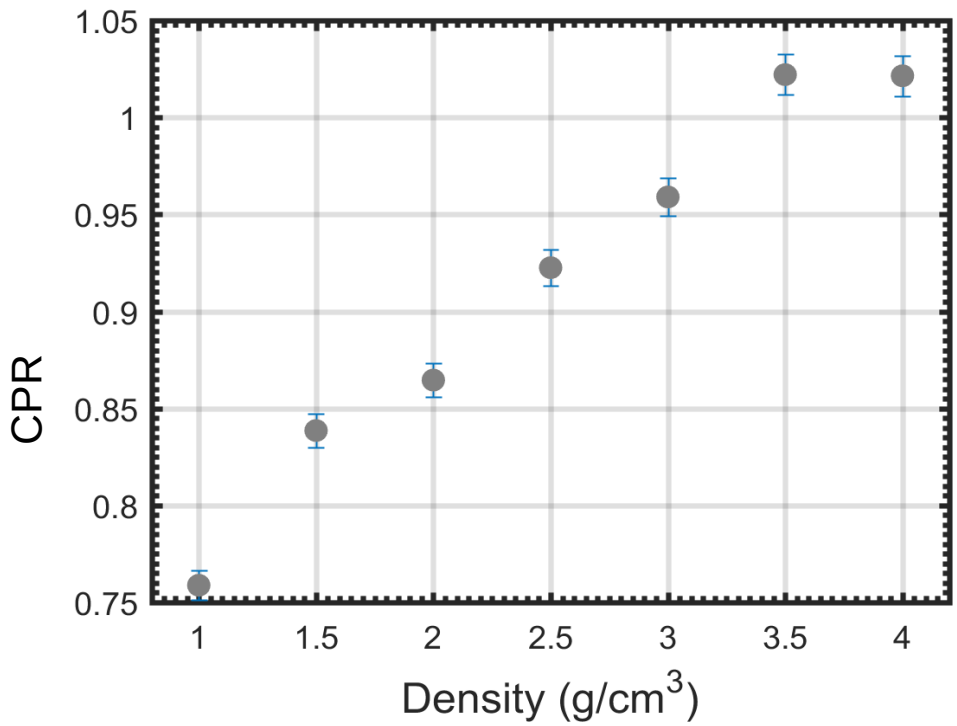

Figure 17: CPR calculated for sphere model. Density varies from 1 to 4 g/cm^3 where for density more than 3.5 g/cm^3 the CPR values do not change with the density.

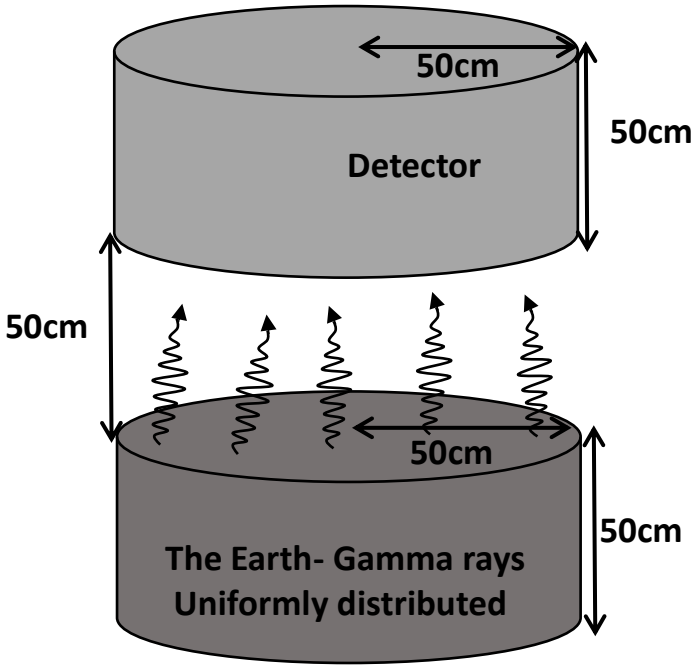

Figure 77: Schematic figure of airborne radiometric, the detector and the source have the same geometry.

The top disc simulates a detector which is defined as a NaCl crystal with dimensions of 50 cm in radius and 50 cm in height, refer to Figure 10. The lower disc simulates the "rock" within which gamma rays with energy of 1.46 MeV (isotropic mono-energy of K^{40}) were uniformly distributed. We defined the rock with nine elements in the earth's crust as, Si 78.66 %, O 2.34 %, Al 5.69 %, Fe 27.78 %, Ca 2.53 %, Na 0.64 %, K 4.83 %, Cl 0.25 % and S 2.28 %. Rock dimensions were the same as the detector. The code was set to terminate the simulation when $5x10^5$ gamma rays were registered in the detector. We kept all the parameters in the models constant and left the rock density the only variable. We ran simulations for density of 1.5, 2, 2.5, 3, 3.5, 4, 4.5 and 5 g/cm^3. The CPR is plotted versus density in Figure 11. As we expected, CPR logarithmically changes with density, which is similar to the "sphere model" only for density greater than 4 g/cm^3 we are not able to distinguish the density variations inferred from CPR values.

Simulation results encouraged us to apply this technique on real datasets. In the following section airborne radiometric from the Elashgin area has been used to assess the ability of CPR to detect density variations.

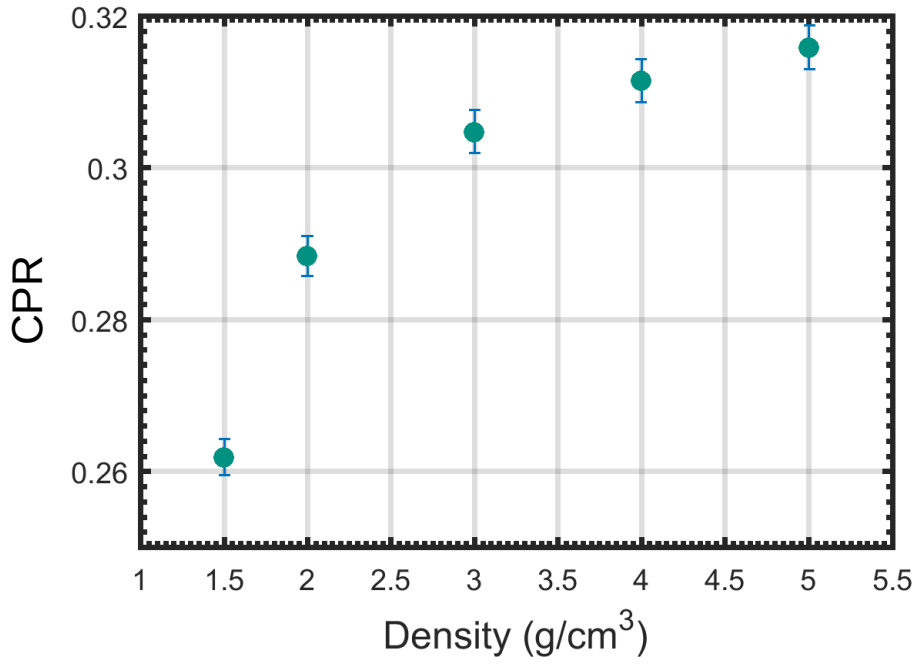

Figure 11: Density variations with CPR values for airborne simulations.

GAMMA RAY SPECTROSCOPY FOR SOIL MAPPING

Understanding land properties such as soil texture, depth and water holding is very difficult spatially (Pracilio 2007). Gamma ray spectrometry can be applied for soil sensing since the response can correspond to soil textures and properties (Cook et al. 1996). Gamma ray radiometric measurements have been available for the last few decades and it is capable of improving speed and efficiency of soil exploration. In radiometric surveys, concentrations of radioactive elements (K, U and Th) are estimated and linked to soil conditions. The K content of the topsoil can be used to map soil variations, indicative of the weathering which can lead to reduction in K content. On the other hand U and Th contents can enhance compared to K as weathering advances (Wilford and Minty 2006). Moreover radiometric signals can also change by variation in mineralogical components of the parent materials (Rawlins, Lark and Webster 2007). Therefore radiometric soil survey should be combined with regional lithology and geochemistry information to allow a better analysis of a survey area.

Applying calculated radioactive concentrations in combination with spatial soil analysis and geochemistry is a common practise for soil and regolith mapping. In the last decade,

other methods are developed to estimate soil depth in addition to the soil properties. For instance gamma rays attenuation by soil layers is used to estimate soil density over the cement rocks or gravel layers (Wong, Oliver and Robertson 2009). The absorption of gamma rays depends on the electron density of the matter that they pass. Above the earth surface the gamma-ray attenuation coefficient only depends on the bulk density since oxygen and nitrogen are dominant elements in the air and most rock types, therefore by Duval (1971).

$$Y(t) = (1 - e^{-0.046 * p_e t}) * 100, \quad (6)$$

where $Y(t)$ is the percent of gamma ray attenuated after passing t cm distance in a formation, p_e is the bulk density of the formation in g/cm^3. In figure 12, gamma-ray attenuation using equation (6) is plotted for density from 1 to 4 g/cm^3 and depth from surface to 30 cm. It shows that for a density of 1.5 g/cm^3, 50% of the gamma rays emit from the top 10 cm of the surface and 90% from the top 30 cm. Moreover soil moisture can attenuate gamma rays with the rate of 1% for a 1% increase in water content (Cook et al. 1996). Hence, gamma rays measured in a radiometric survey can only provide information related to less than 40 cm of the earth soil.

For generating soil maps, a new spatial modelling and digitized soil mapping techniques has been used. It is based on 2 algorithms called Disaggregation and Harmonisation of Soil Map Units Through Resampled Classification Trees (DSMART; Odgers et al., 2014) and Digital Soil Property Mapping Using Soil Class Probability Raster (PROPR; Odgers, McBratney and Minasny, 2015). The DSMART algorithm was used to disaggregate soil classes. In this technique, random virtual sampling within each map unit was used to predict distribution of soil classes based on their link to environmental covariate layers. To have a better estimation of soil class spatial distributions, the algorithm was run 100 times and the results were averaged. The second step is soil property prediction by applying the PROPR algorithm. In this stage, the soil probability maps produced from DSMART algorithm and reference soil property were used to estimate soil properties. For each physiographic zone across WA, a separate estimation was made and it was based on available profile data and surveyor experience.

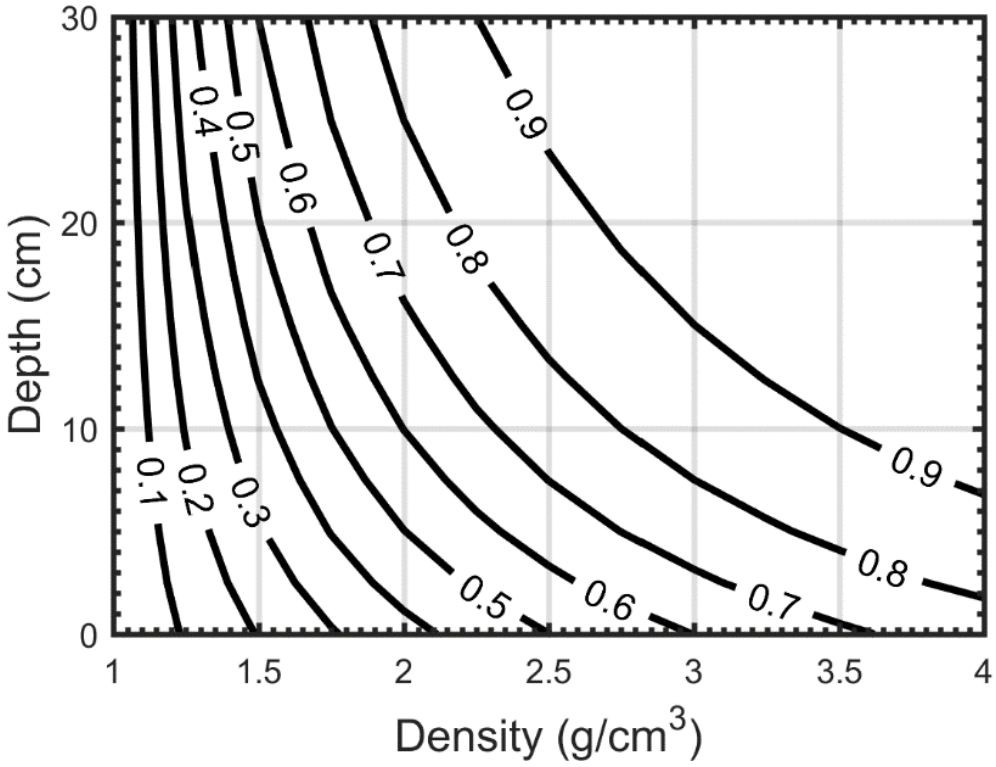

Figure 19: Gamma-ray attenuations from surface to 30 cm of the earth for different densities. Increasing the density and depth of the medium leads to more attenuation.

The bulk density – whole earth product (BDw) was calculated for the soil as a whole (fine and coarse texture fractions), and values were reported in units of g/cm^3. Each soil attribute product was a collection of 6 depth slices. Each depth raster had an upper and lower uncertainty limit associated with it. The depths provided are 0-5 cm, 5-15 cm, 15-30 cm, 30-60 cm, 60-100 cm and 100-200 cm, consistent with the specifications of the global soil map (Holmes, 2014). Our depths of investigations are from surface to 60 cm.

As we explained in the previous section, the CPR technique is limited to the radius of the investigation and is not practical in the borehole conditions. On the other hand, radiometric gamma rays cannot suffer from the limitations as gamma rays are emitting from the top 40 cm of the surface and are less likely to return to the surface. Thus, we are expecting to have conditions similar to one dimension attenuation (refer to equation 4).

In this section, soil density maps of the Elashgin area that were calculated for different depths are presented. These maps are part of soil properties products which are provided by the Department of Agriculture and Food of Western Australia, CSIRO and the University of

Sydney (Holmes, 2014). Soil density maps in this section were obtained using DSMART and PROPR (Odgers, McBratney and Minasny, 2015).

Soil density maps are provided in different depth slices 0-5 cm, 5-15 cm, 15-30 cm, 30-60 cm, 60-100 cm and 100-200 cm (Holmes, 2014). We only considered depths from surface to 60 cm, since our depth of investigation using radiometric gamma ray are only valid up to this depth.

Applying the CPR technique to estimate density

We applied CPR method on the radiometric dataset of the Elashgin area. The Elashgin location and data properties were presented and explained in chapter 6. Thus, in this section we only summarised the result of the CPR method (using the ratio of Compton window and Peak window, derived from the gamma spectrum). The Compton window spanned 350 to 1000 keV where the main isotopes of Th and U have been removed. For thorium, three main isotopes that we considered avoiding in our calculations were Pb^{212} with the energy of 239 keV, Ti^{208} with the energy of 583 keV and Ac^{228} with the energy of 911 keV. With regards to uranium, only two isotopes of Bi^{214} with the energies of 352 and 609 keV were strong enough to be removed from the spectrum. After removal of these isotopes, we integrated the gamma ray counts in the Compton window.

The peak window was actually consisted of all three K^{40}, U^{238} and Th^{232} peaks; since all of them can be equivalently strong (see for example figure 6-3). The peak energy windows were as the following: potassium from 1.34 to 1.58 MeV, uranium 1.62 to 1.86 MeV and thorium from 2.5 to 2.74 MeV. The gamma ray counts in the energy windows were summed. The CPR value was calculated applying the ratio of the Compton to peak windows for each measured point and then gridded with minimum curvature in OASIS montaj software (Fig. 6). The grid size is 10 m, which is the half distance between measurement points along the profile .

Comparing CPR maps with the density map and the geological description

The CPR map is interpreted with respect to the geological information of the survey area. Hence, the important geological features were alphabetically labelled on the CPR map.

We also applied the same labelling pattern on the density maps to have a better comparison between CPR and the density (Figs. 3-6).

f) In region A, The sandy valley is expected to have relatively low density, which is well reflected with low values in the density maps. The CPR map also shows this region with low values. The ironstone gravel patterns in the paleo-channels inside the valley cannot be detected in both the density and CPR maps. That is believed to be due to the low amount of ironstone gravels in these channels, hence they cannot significantly increase the density.

g) In the B category, B1 to B5, the exposed regolith geology is a mosaic of exposed ferricretes that forms wave-like shapes moving up, down and across the slope. The B5 region is a rocky outcrop, which stands out with the highest CPR values and is also interpreted to be ferricrete product from weathering. Hence, we can trace the ferricretes as they are registered with high values in the CPR and this is confirmed on the density maps.

h) The sandy area C is the reworked sand plain with yellow and white sand containing locally abundant limonite pebbles and this region is high in CPR and density. This area is expected to show lower values compare to B regions (ferricretres) but does not follow my expectation.

i) The topographic highs are granitic outcrops, and these should be very low in CPR and density. This is true in the CPR map; however the density map does not follow my expectation and shows very high values. Region E, which is registered with the lowest amount of CPR, also curiously displays high density. This region is dominated by weathered granite; hence, lower CPR is anticipated and seen in the CPR map.

j) Region D has a high CPR signature as expected. This region is laterite (iron-rich materials) that also corresponds with high Th and U but lesser K.

The CPR technique is not well studied in this thesis due to the short research timeframe. Further study on this topic is highly advised as preliminary results from the study of data from the Elashgin area suggest the potential of the CPR technique in remote sensing and soil mapping.

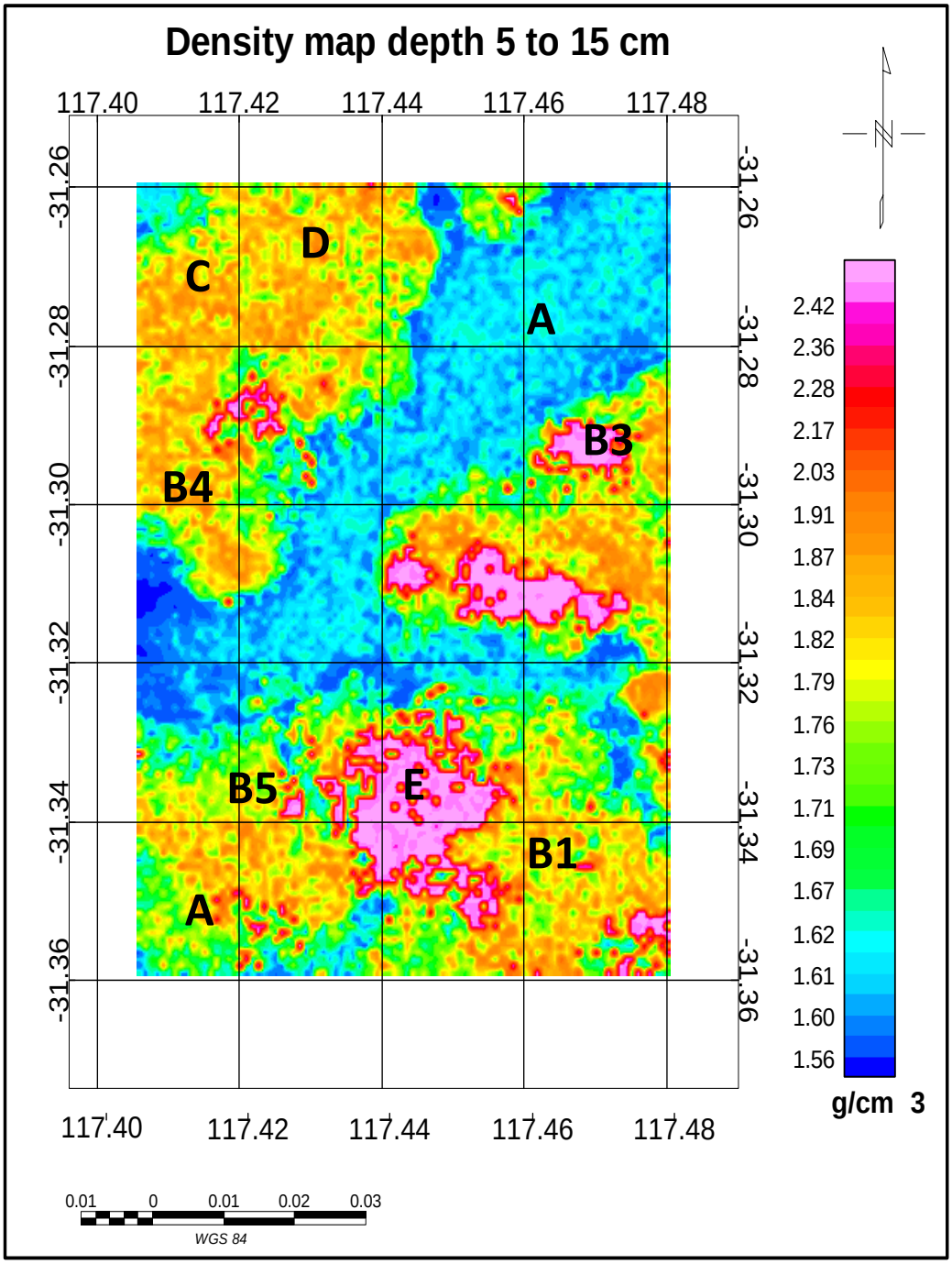

Figure 13: Density map from 0 to 15 cm depth derived from soil density measurements in the Elashgin survey area. Important features are labelled for discussion.

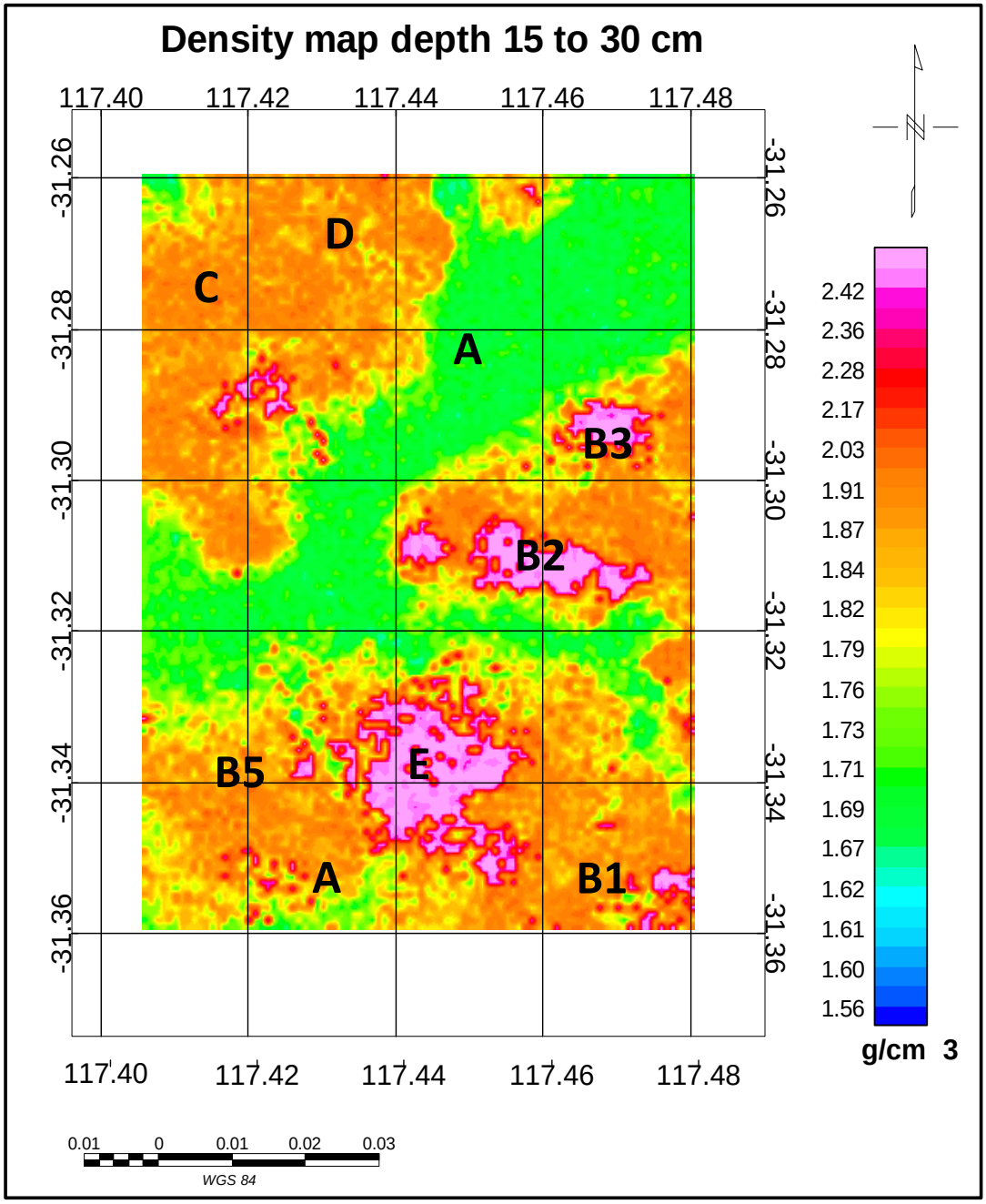

Figure 21: Density map from 15 to 30 cm depth derived from soil density measurements in the Elashgin survey. Important features are labelled for discussion.

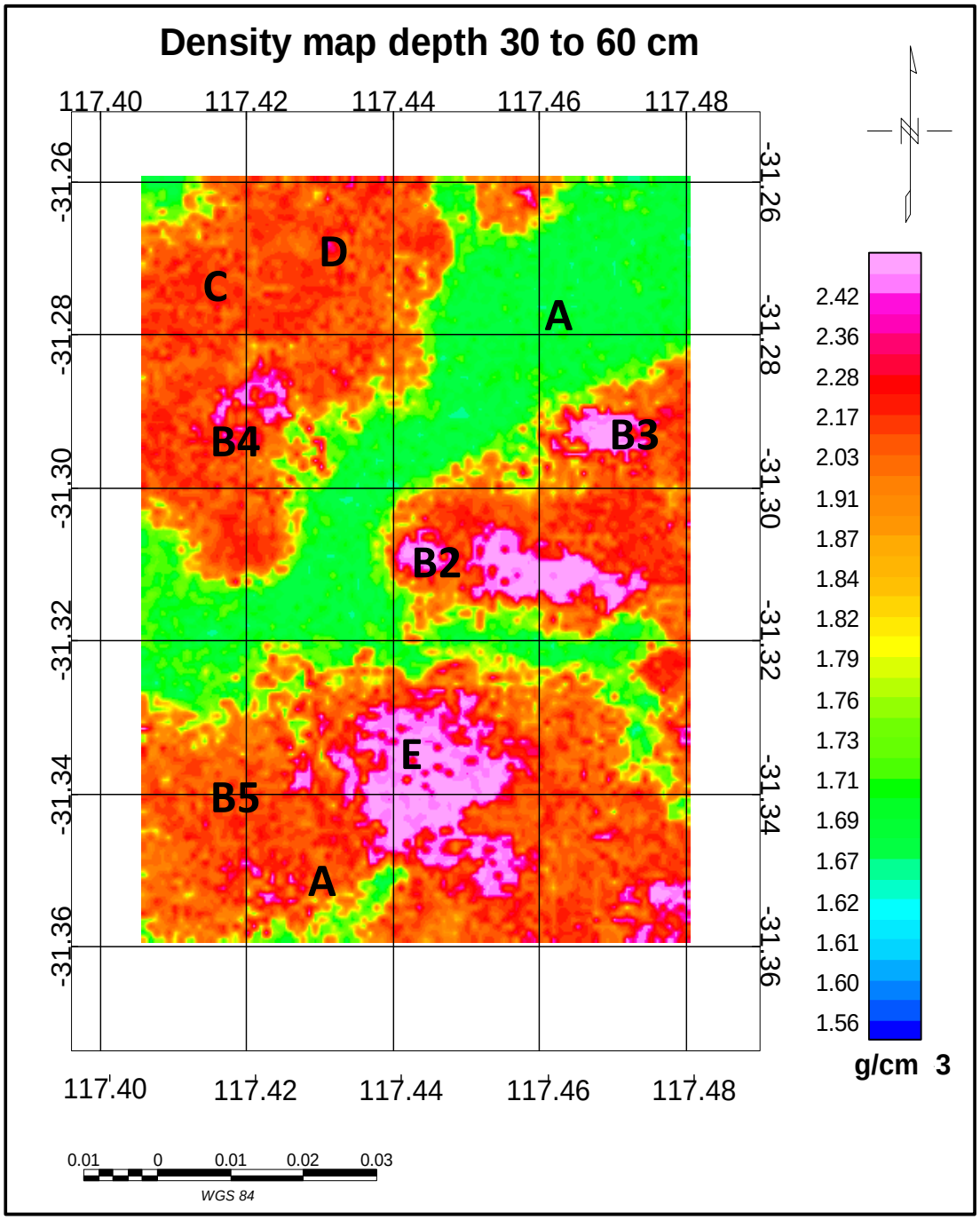

Figure 15: Density map from 30 to 60 cm depth derived from soil density measurements in the Elashgin survey. Important features are labelled for discussion.

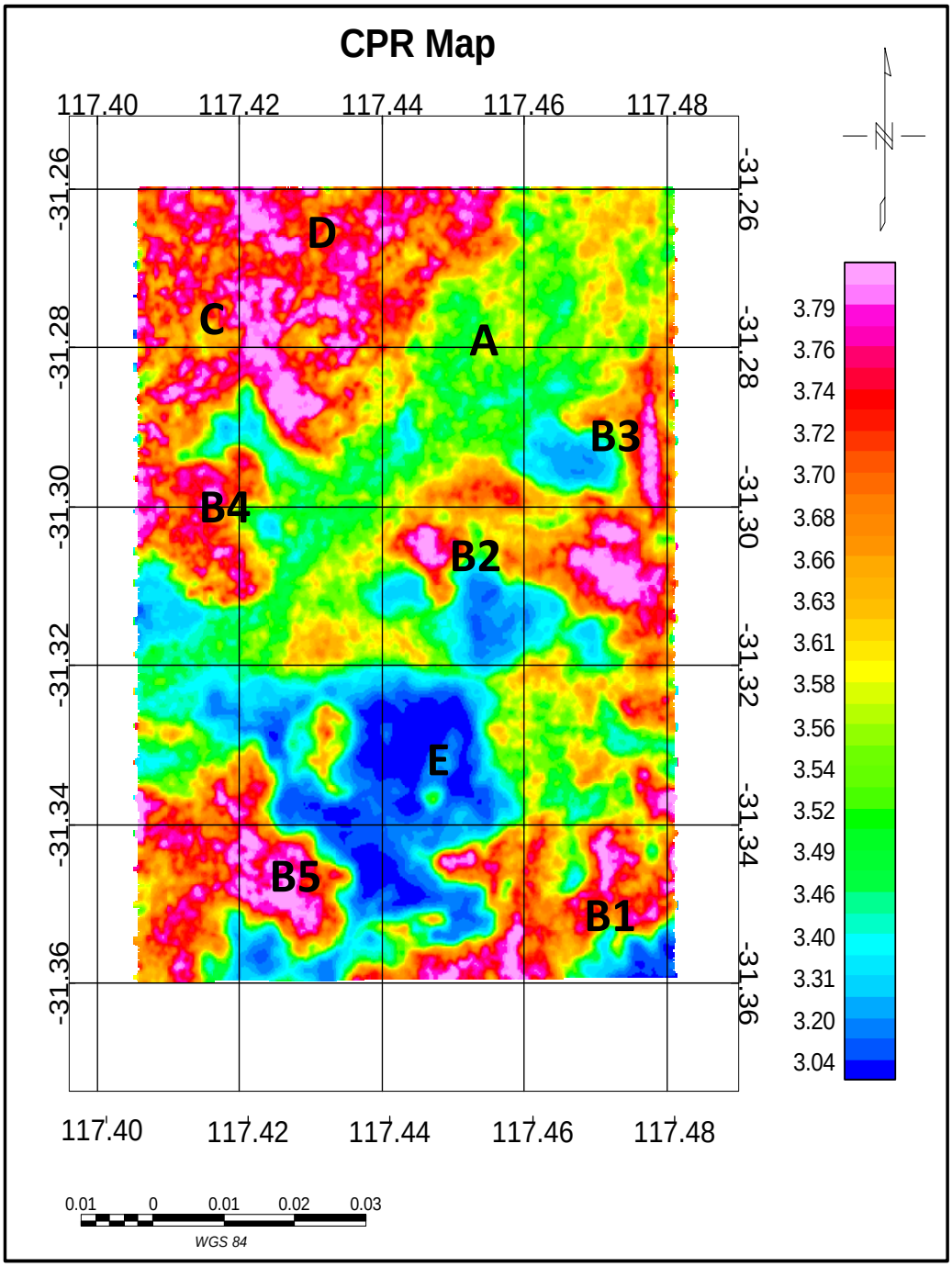

Figure 16: CPR map generated from airborne radiometric data collected during the Elashgin survey.